A Study of Seebeck and Nernst effects in (Ga,Mn)As/normal semiconductor junctions

Dissertation

zur Erlangung des
naturwissenschaftlichen Doktorgrades
der Julius-Maximilians-Universität Würzburg

vorgelegt von
Tsvetelina Naydenova
aus Sofia \ Bulgarien

Würzburg 2014

Eingereicht am: 18.03.2014

bei der Fakultät für Physik und Astronomie

Gutachter der Dissertation:

1. Gutachter: PD. Dr. Charles Gould

2. Gutachter: Prof. Dr. Jens Pflaum

3. Gutachter:

Prüfer im Promotionskolloquium:

1. Prüfer: PD. Dr. Charles Gould

2. Prüfer: Prof. Dr. Jens Pflaum

3. Prüfer: Prof. Dr. Björn Trauzettel

Tag des Promotionskolloquiums: 08.08.2014

Doktorurkunde ausgehändigt am: 22.08.2014

Parts of this thesis have been published elsewhere:

- Ts. Naydenova, P. Dürrenfeld, K. Tavakoli, N. Pégard, L. Ebel, K. Pappert, K. Brunner, C. Gould, and L. W. Molenkamp, Diffusion Thermopower of (Ga,Mn)As/GaAs Tunnel Junctions, Phys. Rev. Lett. 107, 197201 (2011)

Articles from a master thesis published during the Ph.D.:

- Ts. Naydenova, P. Atanasov, M. Koleva, N. Nedialkov, J. Perriere, D. Defourneau, H. Fukuoka, M. Obara, Ch. Baumgart, Sh. Zhou, H. Schmidt, Influence of vanadium concentration on the microstructure and magnetic properties of V-doped ZnO thin films, Thin Solid Films 518, 19, pp. 5505-5508, (2010).

Contents

Zusammenfassung **1**

Summary **4**

1 Introduction **9**

2 Physics Background **13**

2.1 (Ga,Mn)As - Anisotropies and Density of States 13
2.2 AMR, TAMR and Planar Hall effect in (Ga,Mn)As based structures 18
2.2.1 AMR and PHE 18
2.2.2 TAMR and its applications 21
2.2.3 Fingerprint method 23
2.3 Thermoelectric and thermomagnetic effects and the relations between them 25
2.4 Magnetic materials and thermal effects, spin and heat coupling - spin caloritronics 30

3 Diffusion Thermopower of (Ga,Mn)As/GaAs Tunnel Junction **33**

3.1 Thermopower in (Ga,Mn)As - short overview 33
3.2 Diffusion thermoelectricity and phonon drag 36
3.3 Heating current method 37
3.4 Weak Localization 38
3.5 Design and Sample Fabrication 39
3.6 Electrical Characterization of the (Ga,Mn)As / GaAs Tunnel Device 40
3.7 WL Measurements of the electron temperature 43
3.8 Thermopower and Seebeck coefficient 45
3.9 TAMT 47
3.10 Anisotropies of TAMT 51
3.11 Cartoon Model of TAMT 58

4 Anomalous Nernst Effect of (Ga,Mn)As/GaAs Tunnel Junction **63**

4.1 Planar and Anomalous Nernst Effect in (Ga,Mn)As - State of Art 63
4.2 Nernst Geometry and Device Fabrication 68
4.3 Weak Localization Measurements and Temperature Calibration 69

4.4 Detection of the anomalous Nernst Effect of a (Ga,Mn)As/GaAs tunnel junction. 74
4.5 ANE magnetic field sweeps and Nernst Fingerprints 84

5 Conclusion and Outlook **93**

A Appendix **95**

Bibliography **104**

Zusammenfassung

Die Entdeckung des Riesenmagnetowiderstands (GMR)-Effekts im Jahr 1988 von Albert Fert [Baib 88] und Peter Grünberg [Bina 89] führte zu einer raschen Entwicklung auf dem Gebiet der Spintronik und damit zu Fortschritten in der Informations-Technologie. Der darauf aufbauende Bereich der halbleiterbasierten Spintronik bietet darüber hinaus Möglichkeiten Speicherung und Datenverarbeitung in einem einzigen monolithischen Bauteil zu kombinieren. Eine direkte Folge davon ist eine reduzierte Wärmeableitung. Die Beobachtung des Spin-Seebeck-Effekts von Uchida [Uchi 08] im Jahr 2008 brachte ein erhöhtes Interesse hervor und führte zur Forschung im Bereich der Spin-Caloritronics. Während in der Spintronik die Kopplung von Ladungs-und Spintransport untersucht wird, liegt der Fokus der Spin-Caloritronics auf der Wechselwirkungen zwischen Wärme-und Spinströmen. Im Unterschied zur Spintronik mit ihrer Vielzahl von Anwendungen wurde ein reines Spin-Caloritronics Bauteil noch nicht realiziert. Doch viele der neuen Phänomene in der Spin-Caloritronics können in den meisten Spintronik-Bauteilen auftreten. Darüber hinaus könnten thermoelektrische Effekte einen wesentlichen Einfluss auf den Betrieb der Spintronik-Bauteile haben. Dieser Punkt wird von besonderem Interesse für diese Arbeit sein. Tieferes Verständnis der Prinzipien der Kopplung zwischen Wärme- und Spinströmen kann einen alternativen Weg aufzeigen um die Wärmeableitung zu kontrollieren und verspricht neue Funktionalitäten.

Diese Dissertation zielt darauf ab die Kenntnisse über die Thermoelektrik in Materialien mit starker Spin-Bahn-Wechselwirkung zu erweitern, in diesem Fall der prototypische ferromagnetische Halbleiter (Ga,Mn)As. Die Untersuchungen konzentrieren sich auf die thermoelektrischen und -magnetischen Effekte an der Grenzfläche zwischen einem normalen Metall und dem ferromagnetischen (Ga,Mn)As. In solchen Systemen führen die unterschiedlichen Grenzflächen zu einem minimalen Beitrag des Phonon-Drags zu den thermischen Effekten. Dies legt nahe, dass nur Bandbeiträge (ein Diffusionstransport-Regime) auf diese Effekte gemessen werden.

Kapitel 2 beginnt mit einer Einführung über die Eigenschaften der untersuchten Materialsysteme, Grundlagen der Thermoelektrik und Spin-Caloritronics. Die charakteristischen Anisotropien der Zustandsdichte (DOS) von (Ga,Mn)As und die dadurch entstehenden magnetischen Eigenschaften werden beschrieben. Die DOS und die magnetische Anisotropie haben einen Einfluss auf die Transporteigenschaften des Materials und führen zu Effekten wie dem anisotropen Tunnelmagnetowiderstand (TAMR)

[Goul 04]. Einige dieser Effekte werden im Weiteren als eine Referenz für die Ergebnisse der thermoelektrischen und magnetischen Messungen verwendet. Die Anisotropie-Fingerprintabduck-Technik [Papp 07a] wird ebenfalls beschrieben. Die Methode bietet die Möglichkeit, die Material-Anisotropien in verschiedenen Geometrien einfach zu untersuchen.

Kapitel 3 schließt sich mit der experimentellen Beobachtung der Diffusions - Thermospannung an einer (Ga,Mn)As / Si-dotierten GaAs-Tunnelübergang an. Eine Bauteilgeometrie zur Messung der Diffusions-Thermospannung wird vorgeschlagen. Sie besteht aus einem Si-dotierten GaAs-Heiz-Kanal mit einem GaAs/(Ga,Mn)As-Kontakt in der Mitte des Kanals. Ein einzelner Ti/Au-Kontakt wird an der Oberseite des Übergangs aufgebracht. Die Charakterisierung der Probe erfolgt bei 4.2 K. Ein Wechselstrom mit niedriger Frequenz wird durch den Kanal gesendet und erhöht dadurch dessen Temperatur, während der (Ga,Mn)As-Kontakt bei konstanter Temperatur im Helium-Bad bleibt. Aufgrund der Temperaturdifferenz zwischen dem Heizungskanal und dem (Ga,Mn)As-Kontakt entsteht eine thermische (Seebeck-)Spannung, die wir als anisotrope Tunnelmagnetothermospannung bezeichnen (TAMT), ähnlich dem TAMR. TAMT wird mittels Lock-In-Technik bei der doppelten Frequenz des Heizstroms detektiert. Die Seebeck-Spannung wächst dabei linear mit der Temperaturdifferenz an, was auf das Vorliegen eines reinen Diffusionstransport-Regimes hinweist. Ein Beitrag des Gitters (Phonon-Drag) zur Thermospannung, der in der Regel stark nichtlinear von der Temperatur abhängt, wird nicht beobachtet. Der Wert des Seebeck-Koeffizienten des Übergangs bei 4.2 K wird auf 0.5 μV/K abgeschätzt. Das ist ein um drei Größenordnungen kleinerer Betrag als zuvor von [Pu 06] berichtet. Anschließend wird die thermische Spannung unter Einfluss eines äußeren Magnetfelds untersucht. Es zeigt sich, dass die Thermospannung eine Anisotropie mit der Magnetisierungsrichtung aufweist. Diese Anisotropie wird mit den bekannten Eigenschaften des (Ga,Mn)As-Kontakts erläutert. Ferner werden Schaltvorgänge in der Thermospannung detektiert, wenn das Magnetfeld von negativen zu positiven Werten geändert wird. Die Schaltvorgänge erinnern an die Signale eines Spin-Ventils. Dieses Verhalten ist vergleichbar mit den Ergebnissen aus früheren Experimenten an Spininjektion mithilfe eines (Ga,Mn)As-Kontakts in nicht-lokaler Messgeometrie. Dies betont die Bedeutung der thermoelektrischen Effekte und deren mögliche Auswirkungen auf die Spininjektions-Messungen. Ein Polardiagramm der gesammelten Schaltfelder für verschiedene Magnetisierungswinkel zeigt eine zweiachsige Anisotropie und ähnelt früheren TAMR-Messungen an (Ga,Mn)As-Tunnelbarrieren. Ein einfaches Modell wird zur Beschreibung und Abschätzung der erwarteten Thermospannung am untersuchten Übergang eingeführt. Eine gute Übereinstimmung des Modells mit den experimentellen Ergebnissen ist evident.

Der Nernst-Effekt an einem (Ga,Mn)As/GaAs-Kontakt wird im vierten Kapitel untersucht. Hierfür wird eine Modifizierung der Proben-Geometrie vorgenommen. Anstelle des einzelnen Kontakts oberhalb der Übergangsregion werden vier kleine Kontakte hergestellt. Die Temperaturdifferenz wird wiederum mittels Heizkanal gewährleistet. Das Magnetfeld

ist parallel zur Probenoberfläche orientiert. Zwischen sich gegenüberliegenden Kontakten wird eine Spannungsdifferenz bei 2f detektiert. Es stellt sich heraus, dass eine Kosinus-Funktion, mit dem Winkel zwischen der Magnetisierung und der [100]-Kristallrichtung der (Ga,Mn)As Schicht als Parameter, das gemessene Signal gut beschreibt. Dieses wird auf den anormalen Nernst-Effekt (ANE) des ferromagnetischen Kontakts zurückgeführt. Die Symmetrie des ANE unterscheidet sich von der des Seebeck- Effekts des Übergangs. Im Temperaturintervall, in dem die Thermo-Spannung untersucht wurde, zeigt auch der ANE-Koeffizient lineares Verhalten mit der Temperaturdifferenz (ΔT). Für größere ΔT jedoch zeigt sich eine nichtlineare Abhängigkeit. Der ermittelte ANE Koeffizient ist um mehrere Größenordnungen kleiner als jeder andere veröffentlichte Wert. Sowohl die Temperaturabhänigkeit als auch die Größe des ANE bedürfen weiterer Untersuchungen. Wird das Feld von positiven zu negativen Werten gefahren, zeigen sich Schaltvorgänge im Nernst Signal. Diese Schaltvorgänge stehen im Zusammenhang mit den Schaltfeldern des ferromagnetischen (Ga,Mn)As. Normalerweise existieren bei TAMR oder AMR Messungen zwei Zustände, einer mit geringem und einer mit hohem Widerstand. Das gemessene Nernst Signal dagegen zeigt drei Zustände - hohe, mittlere und geringe Thermomagnetischespannung. Dieses Verhalten ist nicht nur von der Magnetisierung, sondern auch von der Charakteristik der Nernst-Geometrie beeinflusst.

Kapitel 5 fasst die wichtigsten Erkenntnisse dieser Arbeit zusammen und gibt einen Ausblick auf zukünftige Arbeiten und Experimente.

Summary

The discovery of the Giant Magneto Resistance (GMR) effect in 1988 by Albert Fert [Baib 88] and Peter Grünberg [Bina 89] led to a rapid development of the field of spintronics and progress in the information technology. Semiconductor based spintronics, which appeared later, offered a possibility to combine storage and processing in a single monolithic device. A direct result is reduced heat dissipation. The observation of the spin Seebeck effect by Ushida [Uchi 08] in 2008 launched an increased interest and encouraged research in the field of spin caloritronics. Spintronics is about the coupling of charge and spin transport. Spin caloritronics studies the interaction between heat and spin currents. In contrast to spintronics and its variety of applications, a particular spin-caloritronic device has not yet been demonstrated. However, many of the novel phenomena in spin caloritronics can be detected in most spintronic devices. Moreover, thermoelectric effects might have a significant influence on spintronic device operation. This will be of particular interest for this work. Additional knowledge on the principle of coupling between heat and spin currents uncovers an alternative way to control heat dissipation and promises new device functionalities.

This thesis aims to further extend the knowledge on thermoelectrics in materials with strong spin-orbit coupling, in this case the prototypical ferromagnetic semiconductor (Ga,Mn)As. The study is focused on the thermoelectric / thermomagnetic effects at the interface between a normal metal and the ferromagnetic (Ga,Mn)As. In such systems, the different interfaces provide a condition for minimal phonon drag contribution to the thermal effects. This suggests that only band contributions (a diffusion transport regime) to these effects will be measured.

Chapter 2 begins with an introduction on the properties of the studied material system, and basics on thermoelectrics and spin caloritronics. The characteristic anisotropies of the (Ga,Mn)As density of states (DOS) and the corresponding magnetic properties are described. The DOS and magnetic anisotropies have an impact on the transport properties of the material and that results in effects like tunneling anisotropic magnetoresistance (TAMR) [Goul 04]. Some of these effects will be used later as a reference to the results from thermoelectric / thermomagnetic measurements. The Fingerprint technique [Papp 07a] is also described. The method gives an opportunity to easily study the anisotropies of materials in different device geometries.

Chapter 3 continues with the experimental observation of the diffusion thermopower

of (Ga,Mn)As / Si-doped GaAs tunnel junction. A device geometry for measuring the diffusion thermopower is proposed. It consists of a Si - doped GaAs heating channel with a Low Temperature (LT) GaAs / (Ga,Mn)As contact (junction) in the middle of the channel. A single Ti / Au contact is fabricated on the top of the junction. For transport characterization, the device is immersed in liquid He. A heating current technique is used to create a temperature difference by local heating of the electron system on the Si:GaAs side. An AC current at low frequency is sent through the channel and it heats the electron population in it, while the junction remains at liquid He temperature (experimentally confirmed). A temperature difference arises between the heating channel and the (Ga,Mn)As contact. As a result, a thermal (Seebeck) voltage develops across the junction, which we call tunnelling anisotropic magneto thermopower (TAMT), similar to TAMR. TAMT is detected by means of a standard lock-in technique at double the heating current frequency (at $2f$). The Seebeck voltage is found to be linear with the temperature difference. That dependence suggests a diffusion transport regime. Lattice (phonon drag) contribution to the thermovoltage, which is usually highly nonlinear with temperature, is not observed. The value of the Seebeck coefficient of the junction at 4.2 K is estimated to be 0.5 μV/K. It is about three orders of magnitude smaller than the previously reported one [Pu 06]. Subsequently, the thermal voltage is studied in external magnetic fields. It is found that the thermopower is anisotropic with the magnetization direction. The anisotropy is explained with the anisotropies of the (Ga,Mn)As contact. Further, switching events are detected in the thermopower when the magnetic field is swept from negative to positive fields. The switchings remind of a spin valve signal and is similar to the results from previous experiments on spin injection using a (Ga,Mn)As contacts in a non-local detection scheme. That shows the importance of the thermoelectric effects and their possible contribution to the spin injection measurements. A polar plot of the collected switching fields for different magnetization angles reveals a biaxial anisotropy and resembles earlier TAMR measurements of (Ga,Mn)As tunnel junction. A simple cartoon model is introduced to describe and estimate the expected thermopower of the studied junction. The model yields a Fermi level inside of the (Ga,Mn)As valence band. Moreover, the model is found to be in good agreement with the experimental results.

The Nernst effect of a (Ga,Mn)As / GaAs tunnel junction is studied in Chapter 4. A modified device geometry is introduced for this purpose. Instead of a single contact on the top of the square junction, four small contacts are fabricated to detect the Nernst signal. A temperature difference is maintained by means of a heating current technique described in Chapter 3. A magnetic field is applied parallel to the device plane. A voltage drop across two opposite contacts is detected at $2f$. It appears that a simple cosine function with a parameter the angle between the magnetization and the [100] crystal direction in the (Ga,Mn)As layer manages to describe this signal which is attributed to the anomalous Nernst effect (ANE) of the ferromagnetic contact. Its symmetry is different than the Seebeck effect of the junction. For the temperature range of the thermopower measurements the ANE coefficient has a linear dependence on the temperature difference

(ΔT). For higher ΔT, a nonlinear dependence is observed for the coefficient. The ANE coefficient is found to be several orders of magnitude smaller than any Nernst coefficient in the literature. Both the temperature difference and the size of the ANE coefficient require further studies and analysis. Switching events are present in the measured Nernst signal when the magnetic field is swept from positive to negative values. These switchings are related to the switching fields in the ferromagnetic (Ga,Mn)As. Usually, there are two states which are present in TAMR or AMR measurements - low and high resistance. Instead of that, the Nernst signal appears to have three states - high, middle and low thermomagnetic voltage. That behaviour is governed not only by the magnetization, but also by the characteristic of the Nernst geometry.

Chapter 5 summarizes the main observations of this thesis and contains ideas for future work and experiments.

Chapter 1

Introduction

Some of the major issues of today's society are energy consumption, dissipation, and waste. A significant part of the energy is used by the information technology infrastructure. That covers a wide range of consumers from nanoscale transistors ($\sim 10^{-8}$ W) to massive data centers ($\sim 10^{9}$ W). A limiting factor for the consumers performance is heat dissipation. As an example, it has an impact on the individual microprocessor frequency. This frequency or the corresponding clock rate determines how fast one CPU chip can operate without errors and within the normal temperature parameters. Each time a transistor in the chip changes its state, an electrical current flows through it and heat is dissipated. The faster a chip goes, the more heat is dissipated. The energy required for cooling is usually a significant part of the input energy. It can be above 50 % for big data centers [Pop 10]. A source of significant heat dissipation in a CPU chip are the interconnects. They carry the information between semiconductor - based data processing units and the ferromagnetic - based memory elements. Semiconductor spintronics offer the opportunity for reducing the heat dissipation by combining memory, information transport and logic operation into the same material system. That gives an alternative device scheme, where interconnecting wires are not needed.

Recently, the coupling of heat and the spin of electron became of a certain interest and a topic of the new field of spin caloritronics [Baue 10, Baue 12]. This field is believed to result in a new generation of devices, which are able to reuse the heat waste. A model of such device - an insulator-based transistor - is proposed by Tserkovnyak [Tser 13].

In addition, the heat can influence the device operation. As an example, the measurements from a spin - injection device in a non-local geometry are discussed. A schematic diagram of the experiment is shown in Fig. 1.1b. A current flows between contacts "1" and "2". A spin accumulation is detected between contacts "4" and "5", which are at a distance from the current path. Since no current flows between the detection contacts, all spurious magnetoresistive effects are expected to be eliminated. The spin accumulation voltage depends only on the relative orientation of the injecting / detecting contacts. It is similar to a magnetoresistance resistance of a spin valve. In a typical spin valve, the resistance for a parallel magnetization configuration of the magnetic layers is smaller than an

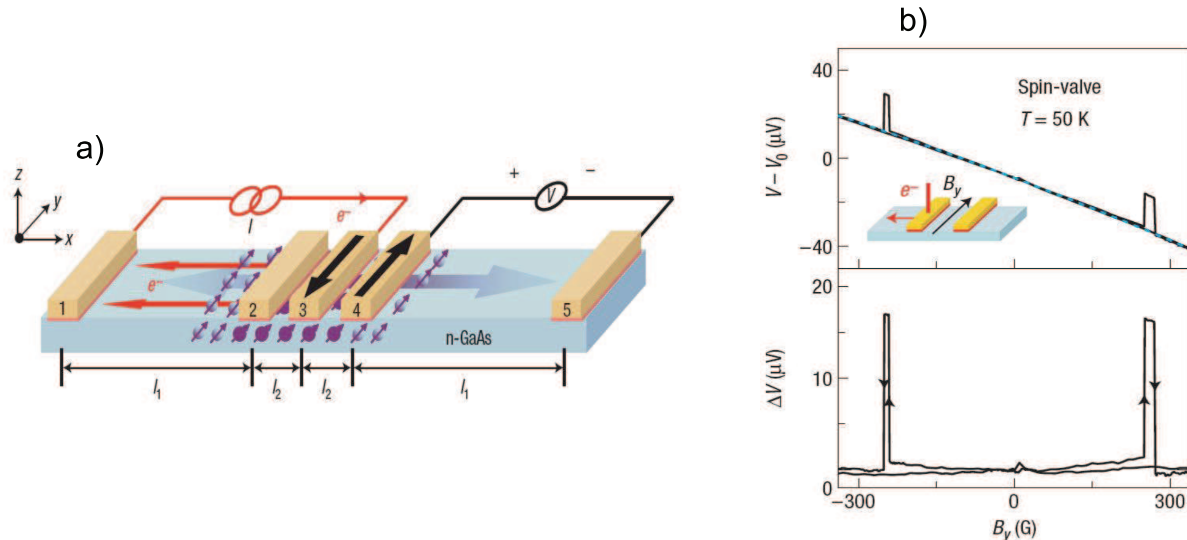

Figure 1.1: a) A schematic diagram of a non-local experiment with Fe contacts [Lou 07] and b) the measured spin-valve signal in the non-local geometry [Lou 07].

antiparallel magnetization state. Fig. 1.1c shows the measured voltage between contacts "4" and "5" (See Fig. 1.1b). In this case, a spin-valve signal is recorded. It is accompanied by a linear with magnetic field background (offset) voltage. This offset is much larger than the spin-dependent effects and is attributed to thermal effects. These thermoelectric effects are usually isotropic with respect to the magnetization of the contacts. Therefore, they are often neglected. However, in materials with strong spin-orbit coupling these effects can be more sophisticated and not so straightforward to be subtracted. Great care should be taken, when such materials, for example a ferromagnetic (Ga,Mn)As, are used as a injection / detection contact in the non-local geometry. The measured signals can be dominated by thermal effects and more knowledge on the physics of thermoelectric and thermomagnetic effects in (Ga,Mn)As is required before neglecting them. Moreover, most of the existing thermoelectric studies on this material system report on phonon drag dominated effects, whereas the electronic contribution to the thermoelectric effects remains unstudied. The diffusion thermopower (the band contribution) can be used as a tool for determination of the Fermi level position. This thesis aims to extend the knowledge on the band contribution to the thermoelectric / thermomagnetic effects in materials with strong spin-orbit coupling. A detailed study is presented on the diffusion thermopower and the Nernst effect of (Ga,Mn)As-based junctions. The work is organized as follows:

- A design and a fabrication scheme of device geometries for measuring the diffusion thermopower and the Nernst effect in ferromagnetic semiconductor (Ga,Mn)As - based junctions are introduced. The junction aims for a minimum phonon drag contribution.

- A heating technique is selected and its advantages are discussed. The main issue is

to heat the carriers but not the lattice.

- An electron temperature calibration is chosen. It is based on the Weak Localization (WL) Effect.
- The Seebeck and the Nernst effects are measured and the coupling of the anisotropy of DOS and these effects is studied.
- Models are proposed to describe the measured data.
- Future applications are discussed.

Chapter 2

Physics Background

This chapter contains a brief introduction on properties of the ferromagnetic semiconductor (Ga,Mn)As used later in the experimental part of this thesis. It also includes some of the main characterization transport techniques employed in the studies of magnetic properties and band structure of that material. Before adding to this group of techniques another magnetization sensitive effect and also a technique based on thermoelectrics and thermomagnetics, an overview of the physics of thermoelectricity and the field of the spin caloritronics is given.

2.1 (Ga,Mn)As - Anisotropies and Density of States

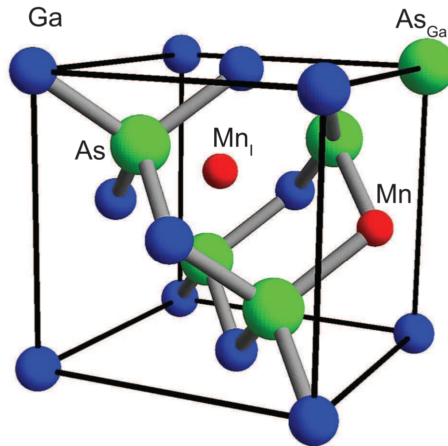

Figure 2.1: (Ga,Mn)As unit cell with defects: As_{Ga} is an As anti-site and Mn_I stands for Mn interstitial. Based on [MacD 05].

(Ga,Mn)As is a GaAs-based ferromagnetic semiconductor, where Mn atoms are incorporated into the lattice substitutionally (favouring the ferromagnetism) or interstitially (in minority) (See Fig. 2.1). It is grown by low temperature molecular beam

epitaxy (MBE) [Ohno 96]. Its position rose among the others ferromagnetic semiconductors after the demonstration of a Curie temperature T_C of about 110 K by Matsukura *et al.* [Mats 98]. The material system became a test-bed for research in spintronics and recently gained interest in the new field of spincaloritronics [Baue 10, Baue 12]. Applications followed as well - a (Ga,Mn)As based read-write logic device [Mark 11a] was recently demonstrated.

For some Mn concentrations, the material is ferromagnetic below a certain critical temperature T_C (the Curie temperature). Different theoretical models are used to explain the electronic structure and the origin of ferromagnetism in these systems. For relatively high Mn concentrations (2 to 9 %) hole-mediated ferromagnetism is observed and commonly described by the p-d mean-field Zener model [Diet 00]. The model implies that T_C depends on the way the Mn is incorporated into the lattice and also on the hole-carrier concentration. Thus the optimization of the Curie temperature can be achieved by increasing the substitutional Mn and by maximizing the free-hole population. Post-growth annealing can further improve these parameters reducing the number of growth imperfections. However, it might also have undesirable influence on some transport properties, in particular the layer anisotropies. These anisotropies are the actual interesting property of the material for transport and further (Ga,Mn)As device applications. Therefore, most of the transport on (Ga,Mn)As is done on as-grown samples at low temperatures, where a high T_C is not crucial. Before continuing with a description of the (Ga,Mn)As anisotropic properties we will briefly show and discuss on some electronic band calculations.

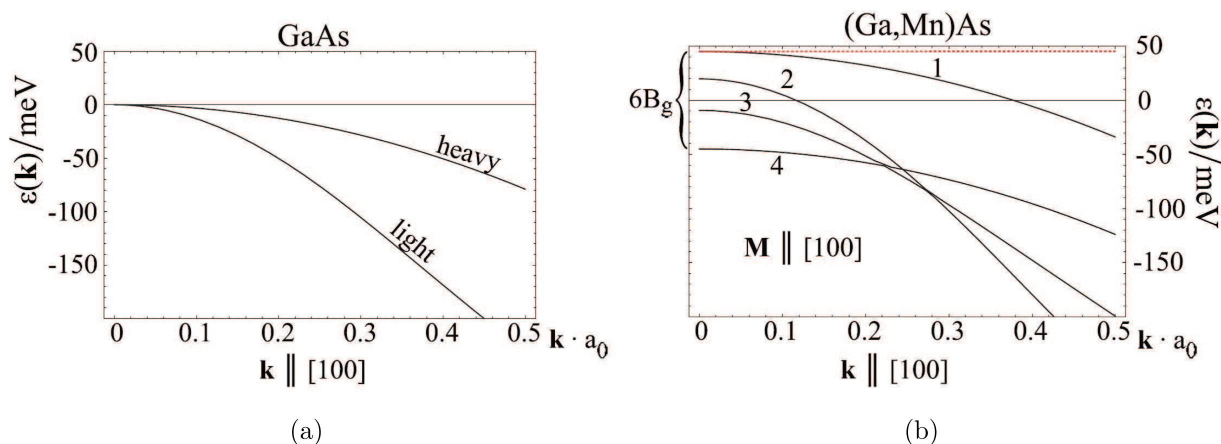

Figure 2.2: The top subbands of the valence band of a nonmagnetic GaAs and a ferromagnetic (Ga,Mn)As. The degeneracy at Γ in the nonmagnetic material is lifted in the magnetic material and the total spin splitting is $6B_g$ (B_g is some coupling constant and for this article is in the order of 15 meV.). Figure reprinted from ref. [Schm 07].

In Fig. 2.2, the difference between a nonmagnetic and a ferromagnetic band structure is shown. It can be seen that at the Γ-point the top valence band of the nonmagnetic material is degenerate, while for the ferromagnetic semiconductor the bands for spin-up

and spin-down are separated by the pd-exchange coupling. This energy separation results in anisotropic effective masses for small k and mixing of the bands due to the mean-field pd-exchange.

In their studies on the (Ga,Mn)As band structure Schmidt *et al.* [Schm 07] considered a magnetic host material and calculated the wave function of a trapped valence hole in the host potential. For the calculations the $k \cdot p$-method is used. The wave function for different directions of the magnetization is calculated and depicted on Fig. 2.3. In this approximation only the Γ point of the band structure contributes.

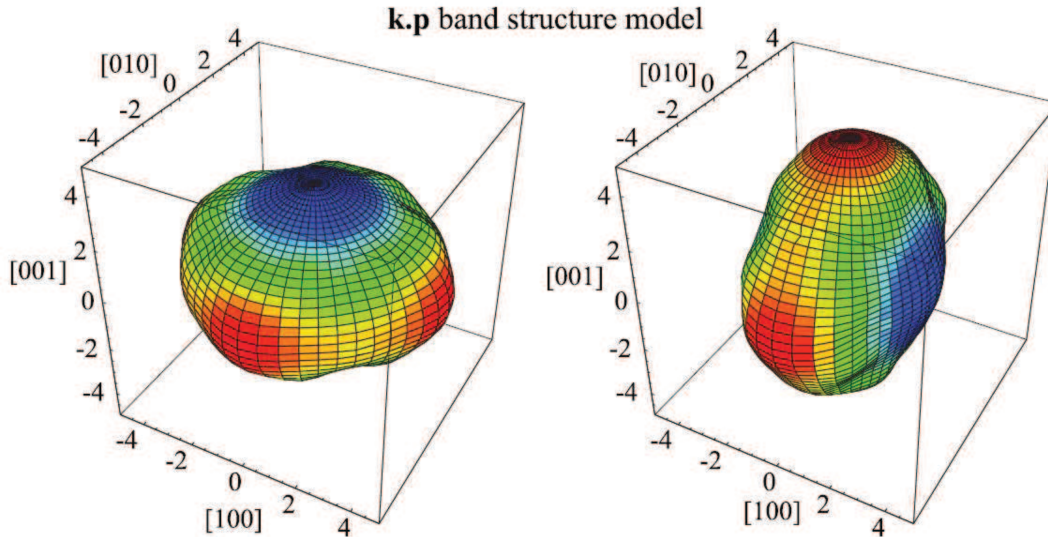

Figure 2.3: Shape of the bound-hole wave function calculated with **k.p** band structure model. The magnetization is oriented along [001] (left) and [100] (right), accordingly. Figure reprinted from ref. [Schm 07].

It can be noticed that the hole wave function is related to the magnetization in a way that it is extended in the direction perpendicular to the magnetization direction. That relation is attributed to the ferromagnetic band structure, where the effective mass at Γ in the host material is magnetization direction dependent. As a consequence, an enhanced anisotropy is observed.

Furthermore, the effect of growth strain on the bound-hole wave function is studied [Schm 07]. The results of the calculations are given in Fig. 2.4. The magnetic field for this experiment points along [010] and for a comparison the wave function with no induced strain is also presented. Tensile and compressive strain are considered. They both modify the wave function. The compressive strain extends it in-plane along the magnetization direction, while the tensile strain produces a large extend in the growth direction. A reason for that is found again to be due to a variation of the host band structure. A direct consequence of the growth strain is a broken symmetry between the [001] growth direction and the two in-plane easy axes - [100] and [010]. The last two have also revealed

a broken symmetry in experiments, but its origin is still controversial.

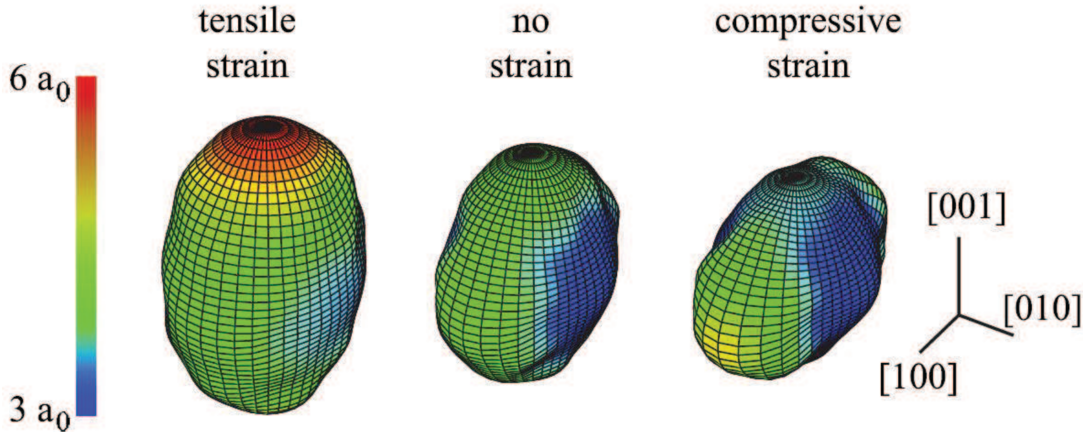

Figure 2.4: The impurity wave function in the presence of tensile (left) or compressive (right) growth strain. The nonstrained wave function in the middle is for comparison. The magnetization is along [010]. Figure reprinted from ref. [Schm 07].

At this point it is worth noting that the breaking of the symmetry has an influence also on the magnetic properties. Anisotropy of the ferromagnetic host DOS is linked to the magnetic anisotropies via spin-orbit coupling. Thus in compressively strained (Ga,Mn)As layers, for example, a biaxial anisotropy is observed, where the magnetization has two in-plane easy axes and an out-of-plane hard axis. An easy axis corresponds to a minimum anisotropy energy of a system. The anisotropy energy of (Ga,Mn)As is usually given with the following relation [Papp 07a]:

$$E = \frac{K_{cryst}}{4}\sin^2(2\theta) + K_{uni[\bar{1}10]}\sin^2(\theta - 135^\circ) + K_{uni[010]}\sin^2(\theta - 90^\circ) - MH\cos(\theta - \varphi). \tag{2.1}$$

The main components are the crystalline biaxial term, two smaller uniaxial terms and the Zeeman energy. The ratio between the anisotropy components of an unpatterned (Ga,Mn)As layer is usually $K_{cryst} : K_{uni[\bar{1}10]} : K_{uni[010]} = 100 : 10 : 1$. That ratio can vary for layers grown at different growth conditions (for example in different labs [Goul 08]) and also can be lithographically modulated [Weni 07, Hump 07]. The magnetization direction is determined by the external field along with anisotropy energy considerations. The mechanism for aligning the magnetization along an external magnetic field depends on the initial state and the required for the alignment energy. It can be a coherent Stoner-Wohlfarth rotation, a domain wall (DW) nucleation / propagation, or a combination of both. To make it clear for the reader, the anisotropy energy as a function of the angle of magnetization is depicted on Fig. 2.5. At the first place no field is applied and the three anisotropy components along with its envelope are presented as follows: sand colour is

the crystalline term, red stands for the uniaxial [$\bar{1}$10], blue is for the uniaxial [010] and the violet line is the total energy.

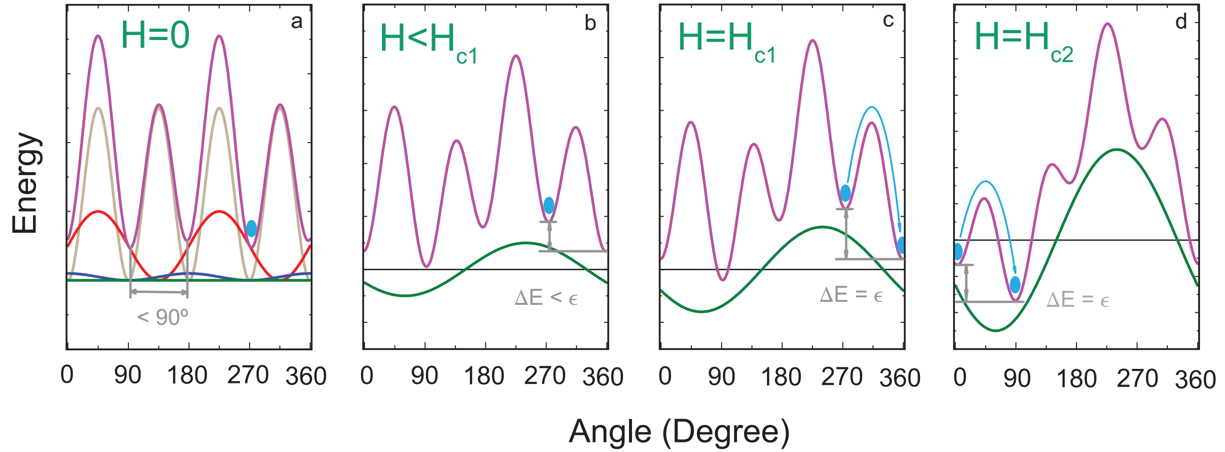

Figure 2.5: Anisotropy energy landscape for different applied magnetic fields.

The light blue dot indicates the magnetization direction and for the Fig. 2.5a this is initially chosen to be 273°. Then the magnetic field is swept along 60° and the evolution of the total energy is given for certain values of the external field. For small fields (smaller than H_{c1}) a rotation is visible on Fig. 2.5b. When the applied field is further increased to a value of H_{c1}, the energy of the system can be minimized through a magnetization reversal process. That involves a formation / propagation of a 90° DW in this case (See Fig. 2.5c). For a certain higher field H_{c2} a second magnetization reversal occurs and the magnetization direction jumps closer to the one of the external field as shown in Fig. 2.5d. The final alignment along 60° is completed with a Stoner-Wohlfarth magnetization rotation (not shown here). The described magnetization reversal through two 90-degrees DW is a characteristic for materials with cubic magnetic anisotropy [Cowb 95]. This behaviour can be observed either by means of magnetic properties characterization (SQUID) or utilizing certain transport techniques. The latter is summarized in the following sections.

2.2 AMR, TAMR and Planar Hall effect in (Ga,Mn)As based structures

Transport and magnetic properties can be anisotropic in some ferromagnets, in particular in (Ga,Mn)As. These anisotropies result in effects like anisotropic magnetoresistance (AMR), planar Hall effect (PHE) and tunneling anisotropic magnetoresistance (TAMR). These effects are usually used as a characterization tool and can bring some insight on the properties of materials. Moreover, these effects can be helpful explaining the physics of magnetism in materials and allow for small magnetic moments to be measured, where a standard magnetometry fails in detection. In this section a brief introduction to the physics of these effects is given. Afterwards we continue with the anisotropies of the thermoelectric and thermomagnetic effects in structures with one ferromagnetic contact.

2.2.1 AMR and PHE

Anisotropic magnetoresistance is an effect of electrical resistance changes in ferromagnetic metals / semiconductors depending on the direction of magnetization relative to the current [McGu 75]. The effect has two components - a non-crystalline and a crystalline term. The non-crystalline AMR can be positive or negative. Positive is when the resistance for magnetization parallel to the current is bigger than the one for perpendicular configuration of the two vectors. Negative is accordingly the opposite case. Bulk (Ga,Mn)As reveals negative non-crystalline AMR [Baxt 02, Mats 04] and the sign of the non-crystalline term is explained by the ratio of the magnetic and the non-magnetic scattering [Rush 09]. The crystalline component of the AMR is usually much weaker and starts playing an increasing role in thin (Ga,Mn)As films [Rush 07]. The two components can be independently accessed using different device geometries [Rush 06, Rush 07]. To measure the non-crystalline term a Hall bar is fabricated along a defined crystalline axis, whereas the crystalline AMR can be measured in a Corbino disk geometry [Rush 06, Rush 07].

In general, the relation between the electric field and the current (Ohm's law) can be divided into two components - parallel and perpendicular with respect to the magnetization [Doer 38, Jan 57, McGu 75]:

$$\mathbf{E} = \rho_{\|}\mathbf{J}_{\|} + \rho_{\perp}\mathbf{J}_{\perp}. \tag{2.2}$$

The longitudinal resistivity is then given by the following relation:

$$\rho_{xx} = \rho_{\perp} - (\rho_{\perp} - \rho_{\|})\cos^2(\theta), \tag{2.3}$$

where θ is the angle between the magnetization and the current vectors, and $\rho_{\|}$ and $\rho_{\perp}$ are the resistivity parallel and perpendicular to the magnetization.

In most 3d transition metals, the AMR effect is positive, meaning a higher resistance for a parallel current to magnetization configuration. That is different with respect to the

(Ga,Mn)As and it poses a question about the origin of the non-crystalline AMR term. Recently, a model describing the mechanism responsible for the non-crystalline term in (Ga,Mn)As was proposed by Výborný *et al.* [Vybo 09]. The physical origin of the AMR is ascribed to the combination of spin-orbit interaction (SOI) and broken symmetry due to the presence of magnetization [Vybo 09]. Three distinct mechanisms may lead to AMR and they are depicted in Fig 2.6. The most relevant for metallic (Ga,Mn)As samples according to Výborný *et al.* is the anisotropic scattering mechanism depicted in Fig 2.6b.

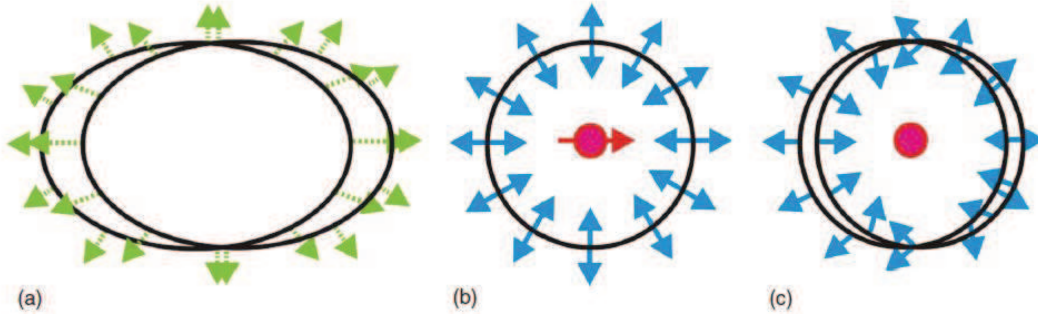

Figure 2.6: Three different mechanism in combination with magnetization and SOI can be responsible for the AMR effect and they are present as follow: (a) anisotropic Fermi velocities along the Fermi surface for the charge carriers, anisotropic relaxation rates due to (b) unpolarized bands scattered by anisotropic impurities, or (c) partially polarized bands scattered by isotropic impurities. For metallic (Ga,Mn)As the mechanism (b) is dominant. It predicts the correct sign and identifies its origin - destructive interference between the electric and the magnetic part of the scattering potential (of ionized Mn acceptors) for carriers moving parallel to the magnetization [Vybo 09]. Figure reprinted from ref. [Vybo 09].

When a magnetic field is applied perpendicular to the current direction in a non-magnetic material, the charge carriers experience the Lorentz force and the Hall voltage develops perpendicular to the current and the magnetic field directions. The resulting ordinary Hall resistance is proportional to the external magnetic field and the inverse of the carrier concentration. In magnetic systems, along with the ordinary Hall voltage, an anomalous Hall (AHE) effect also arises. The AHE is an antisymmetric transverse MR coefficient, described with the following expression: $\rho_T(M) = -\rho_T(-M)$ [Jung 13]. Here, M is the magnetization vector perpendicular to the plane of a Hall bar sample. Microscopically, spin-orbit coupling is defined as one of the factors determining the AHE and AMR in bulk materials [Jung 08]. As described earlier, the AMR results in a resistivity tensor, which is dependent on the angle θ between the current and the magnetization. The off-diagonal component of that tensor is given with the following expression:

$$\rho_{xy} = -\frac{\rho_\perp - \rho_\parallel}{2} \sin(2\theta). \tag{2.4}$$

This component is transverse to the current like a Hall effect but the magnetization stays in-plane. The arising voltage is know as the transverse AMR or planar Hall effect (PHE). As the AMR, it depends on the magnetization direction with respect to the current. In this case, $\rho_T(M) = \rho_T(-M)$, where M has an arbitrary orientation. The mechanism causing the planar Hall effect is thus different from one responsible for the anomalous Hall effect [Jung 08].

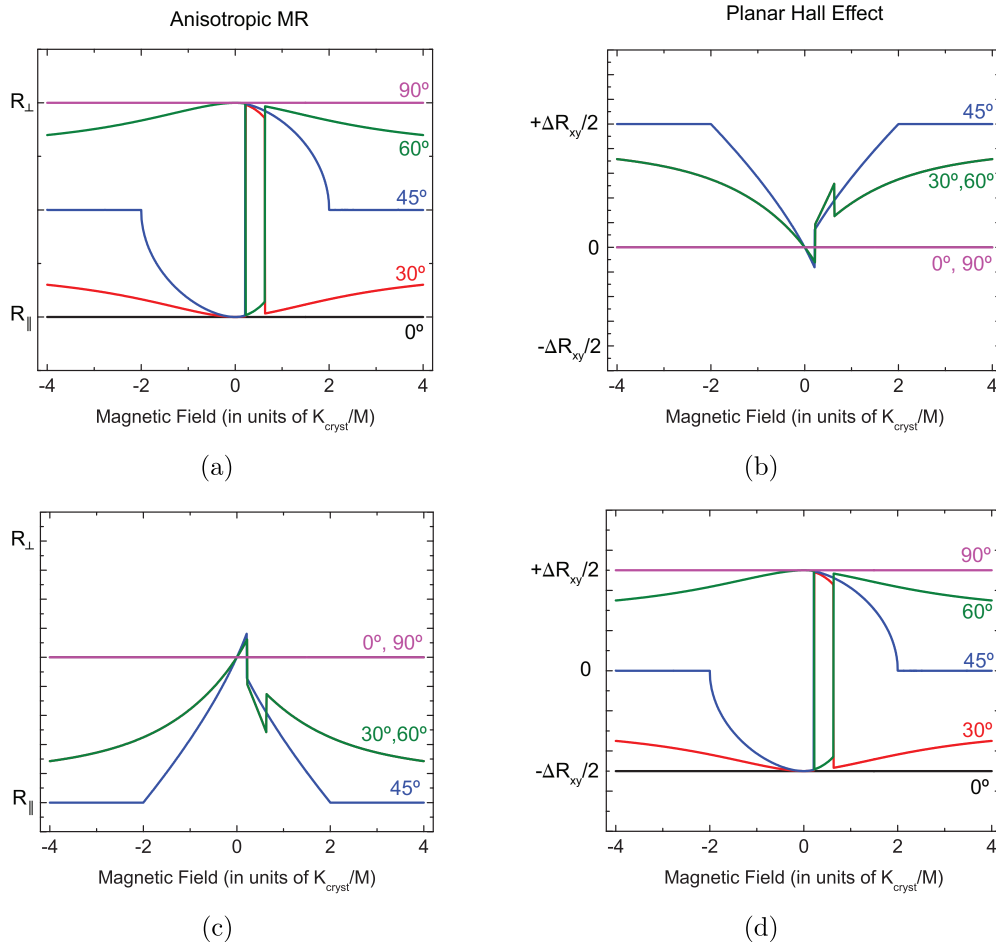

Figure 2.7: Calculated AMR and PHE curves for magnetic field sweeps along different in-plane angles. The underlying magnetic anisotropy is biaxial with easy axes along [100] and [010]. Figures (a) and (b) are curves for a current along [100] crystal direction. Figures (c) and (d) are calculated for an angle of 45° between the current and the [100] direction. All angles are with respect to the [100].

A giant planar Hall effect is reported for (Ga,Mn)As layers patterned in a Hall bar geometry [Tang 03]. The observed effect is 4 orders of magnitude stronger than found in metallic ferromagnets. It is demonstrated that the PHE provides an insight into the magnetization reversal process, and in particular the magnetic anisotropy of materials. Later, the effect is used to study the evolution of domain walls during the process of magnetization reversal [Tang 04, Jung 08].

According to the above mentioned equations, AMR and PHE signals have different dependences on the magnetization angle θ. The two functions describing the effects have different extrema with respect to θ. The AMR exhibits extrema at $\theta = 0°$ and $\theta = 90°$, whereas the PHE has extrema at $\theta = 45°$ and $\theta = 135°$. For studying the magnetic anisotropy of a ferromagnetic material (usually in a Hall bar geometry), one of the effects appears to be more sensitive than the other depending on the direction of the current flow. To clarify the last statement, we consider a Hall bar of biaxial (Ga,Mn)As. Fig. 2.7 depicts the calculations, where the two effects are studied in a Hall bar defined along different crystal directions on a biaxial (Ga,Mn)As layer.

From the figure 2.7 it becomes clear that when the current flows along one of the magnetic easy axis in the biaxial material, the anisotropies are easier to be studied with the help of the longitudinal magnetoresistance measurement, while for Hall bars along a hard axis transverse resistance (or planar Hall configuration) measurements are the only useful technique [Goul 04].

In the following section another technique for studying anisotropies of magnetic systems is described. It is proven as a useful tool since it provides a direct access to the density of states of the material of interest.

2.2.2 TAMR and its applications

The tunneling process in magnetic heterostructures appears to depend on the magnetization. In particular, when tunneling depends on the magnetization direction with respect to the crystallographic axes, the phenomenon is called tunneling anisotropic magnetoresistance (TAMR). The experimental discovery of the TAMR is reported first by Gould *et al.* [Goul 04] for a tunneling structure with one magnetic contact. A schematic of the TAMR sample is given in Fig. 2.8(a).

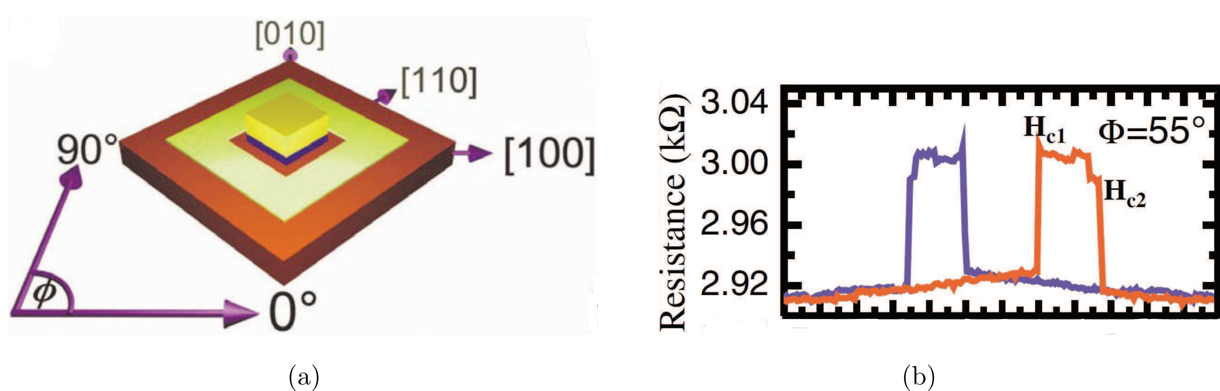

(a) (b)

Figure 2.8: (a) A schematic of the TAMR sample, consisting of a central Au/AlOx pillar allowing tunnel injection into (Ga,Mn)As and a surrounding Ohmic contact. (b) Signal of the TAMR sample for a magnetic field sweep along 55°. Figure reprinted from ref. [Goul 04].

The tunnel contact consists of a central pillar and a backside contact. The pillar contains Ti/Au layers (for contacting) evaporated on an AlOx barrier on top of a 70 nm ferromagnetic (Ga,Mn)As layer. The backside ring Ohmic contact is made of W and Au directly onto the (Ga,Mn)As layer. In this geometry, the tunneling magnetoresistance is measured when the magnetic field is swept back and forth in the plane of the sample. A magnetic field scan for a field applied along 55° in-plane is shown in Fig. 2.8(b). The switching events present in the scan remind of a traditional tunneling magnetoresistance (TMR) spin valve signal. This behaviour is present in each scan along different in-plane directions. The amplitude of the signal is about 3 %. The width and the sign of the TAMR feature are found to depend on the angle of the magnetic field with respect to the [100] easy axis. To describe the measured signal a simple model is introduced, where the tunneling current is given by the following expression:

$$I \propto \int_{-\infty}^{\infty} DOS_{(Ga,Mn)As}(E) \cdot T(E) \cdot DOS_{Au}(E-eV) \cdot (f_{SC}(E) - f_M(E-eV))dE \quad (2.5)$$

The above equation has for parameters the (Ga,Mn)As density of states $\text{DOS}_{(Ga,Mn)As}(E)$ and the Au contact $\text{DOS}_{Au}(E-eV)$, the Fermi functions $\text{f}_{SC}(E)$ of the semiconductor and $\text{f}_M(E-eV)$ of the Au contact. E is the total energy perpendicular to the barrier and $\text{T}(k_z)$ is the tunneling probability. The $\text{T}(E)$ and the $\text{DOS}_{Au}(E-eV)$ are, to a very good approximation, independent of the magnetic field. Further, theoretical analysis shows an anisotropy in the (Ga,Mn)As DOS with respect to magnetization orientation. However, this anisotropy alone is not enough to explain the measured 3 % signal. Additional considerations are made. Transport through the barrier is dominated by a subset of the DOS with high momentum perpendicular to the barrier. This actually means a reduced number of states contributing to the tunneling process. As a result, the anisotropy is increased and can reach the order of few percent, compatible with the experimentally observed resistance changes.

Further, the TAMR is studied in magnetic tunnel junctions (MTJ) [Sait 05] and also in junctions containing one ferromagnetic contact with a semiconductor [Mose 07] or antiferromagnetic spacer [Park 11] as barriers. Recently, the TAMR is demonstrated on the atomic scale [Berg 12]. As an example of applications, nano-TAMR pillars have the possibility of direct magnetization sensing in nanometer scale areas [Mark 11b]. The TAMR switchings in that work reveal a sharp magnetization event, consistent with a microspin behaviour, while the AMR scan hinted for a multi domain state. Moreover, the effect is implemented as a reading tool in the (Ga,Mn)As based 1 bit demonstrator read-write device reported by Mark *et al.* [Mark 11a].

In summary, the TAMR is a possible method to directly access, characterize and control the anisotropies of the density of states and the magnetic properties of magnetic systems.

2.2.3 Fingerprint method

To facilitate the analysis of the obtained datasets from AMR, PHE and TAMR measurements, a fingerprint technique is introduced by Pappert *et al.* [Papp 07a]. As earlier discussed, the above transport measurement techniques give the possibility to detect the presence of small magnetic moments. That is otherwise more difficult or not accessible at all for the bulk characterization tools as SQUID or vibrating sample magnetometry (VSM). In this section a brief description the fingerprint method is given. The technique is later utilized for a representation of the measured Seebeck and Nernst effects data.

The fingerprint is a colour coded polar plot and it summarises the results from a given transport measurement. Usually, the resistance is the measured value and its magnitude determines the colour coding. The method is faster than the traditional alternatives when studying the angular dependence of the magnetization switching fields. It offers a possible way to get a detailed mapping of the magnetic anisotropies. Moreover, it is proved to be more sensitive to secondary effects of strain, processing, contacting, etc. Below, a few examples are given to illustrate the sensitivity of the technique.

Figure 2.9 shows PHE measurements on a Hall bar oriented along the [110] crystal direction. First, a single magnetoresistance curve for a magnetic field applied along 80° is given (See Fig. 2.9(a)). The magnetic field is swept from -300 mT to small positive fields. At certain field values, a typical double switching event is observed. A high resistance value corresponds to a red colour in the scale and black stands for low resistance value. For many angles the MR-curves are collected and plotted in a resistance polar plot (RPP) in Fig. 2.9(b). The 80°-segment is marked by a dotted white line.

From the polar plot it is obvious that the innermost region which is actually the H_{c1}-pattern has a semi-square like behaviour. Square-like behaviour is a characteristic of a biaxial material with easy axis along the diagonal of the square. Here we use "semi" because the square is actually elongated and more rectangle-like. This is a signature of an additional uniaxial component with an easy axis bisecting the biaxial easy axes (here $[1\bar{1}0]$). Furthermore, some discontinuities in the middle of the rectangle indicate a uniaxial magnetic term collinear with one of the easy axes, here the [010] crystal direction. The contributions of the two additional uniaxial terms can be estimated from the dimensions of the rectangle. The $[1\bar{1}0]$ uniaxial contribution to the biaxial anisotropy can be calculated from the angle between the two easy axes. When working with the aspect ratio, instead of the angle, the $[1\bar{1}0]$ uniaxial component is given by the following expression:

$$\frac{K_{uni[110]}}{K_{cryst}} = \cos(2\arctan(\frac{W}{L})), \qquad (2.6)$$

where W and L are the width and the length of the rectangle, respectively. The discontinuity in the middle of the rectangle is a measure of the [010] additional uniaxial term and is equal to $\sqrt{2}K_{uni[110]}$. The domain wall nucleation/propagation energy can also be

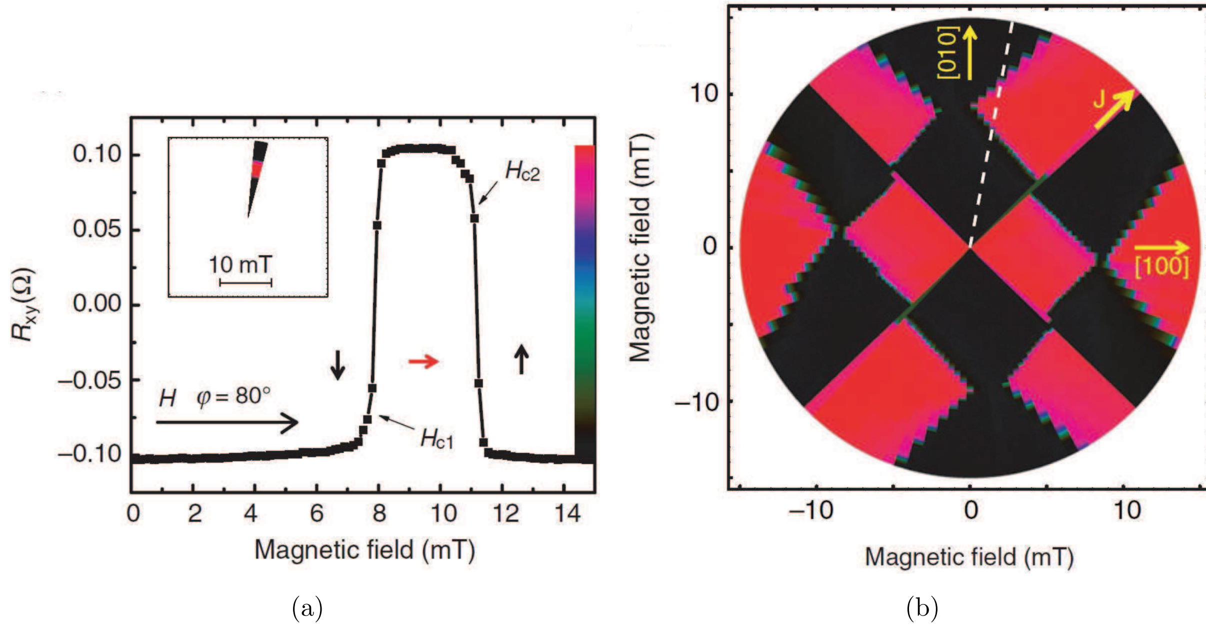

Figure 2.9: (a) PHE measurement with magnetic field along 80° and (b) a RPP compilation of PHE measurements for every 3°. Figure reprinted from ref. [Papp 07a].

estimated from the H_{c1}-pattern. It is half the length of the diagonals of the rectangular pattern.

In summary, the present fingerprint technique visualizes the symmetry components of the anisotropy and allows for a qualitative and quantitative determination of the different anisotropy terms. This method will be used later for studies of thermoelectric and thermomagnetic effects in a (Ga,Mn)As/GaAs tunnel junction.

Before continuing to the experimental part, the basic physics of thermoelectricity is briefly discussed in the following sections of this chapter.

2.3 Thermoelectric and thermomagnetic effects and the relations between them

In this part, a short overview on the basics of thermoelectric and thermomagnetic effects in metals and semiconductors is given. The relations between the thermoelectric effects are introduced and their validity in an external magnetic field is discussed. Magnetic materials are also considered. The combination of heat and magnetization is briefly discussed and the outline of the spin caloritronics is presented.

In an electrical conductor, the coupling between a heat flux and charges results in the occurrence of thermoelectric effects. The relations between the electrical (J) / thermal (Q) currents and the applied electric field (E) / temperature gradient (∇T) can be written with the following phenomenological expressions [Delv 65]:

$$E = \rho J + S\nabla T \tag{2.7}$$

$$Q = \pi J - \kappa \nabla T. \tag{2.8}$$

The coefficients in these relations describe the transport properties of the media. These are the resistivity ρ, the Seebeck coefficient (thermopower) S, the Peltier coefficient π and the thermal conductivity κ. The Seebeck coefficient across an open junction (zero electric current) is defined as:

$$S = -\lim_{\Delta T \to 0} \frac{\Delta V_{th}}{\Delta T}. \tag{2.9}$$

It is a measure of the effect of a voltage drop which develops in a electrical conductor due to an applied temperature gradient.

The detection of the thermopower is not straightforward [Ashc 76]. If a voltmeter is connected to points of a sample at different temperatures, this would cause a temperature gradient across the meter. That will result in a detection of an additional thermal voltage. To overcome this complication, a thermocouple is usually used (see Fig. 2.10a). In that geometry, a junction of two materials is kept at one temperature, while the ends of the junction (connecting points to the voltmeter) are at another temperature. Hence, no temperature gradient is present in the voltmeter and only the thermal voltage across the junction is measured. The resulting thermopower will depend on the properties of the materials comprising the junction. If one wants to measure the absolute thermoelectric voltage of a particular material, the second material in the thermocouple should not have a response to a temperature difference. A superconductor provides this requirement, since no thermovoltage develops across a superconducting metal [Ashc 76]. The thermopower over a normal - superconducting metal junction is then only due to the normal metal.

Similar voltages can occur when a temperature gradient is established across a magnetic material (Fig. 2.10 b). They are proportional to the temperature gradient and the phenomenon is known as the spin Seebeck effect (SSE). Its nature is different than this of the ordinary Seebeck voltage. By definition, the spin Seebeck effect is a spin voltage

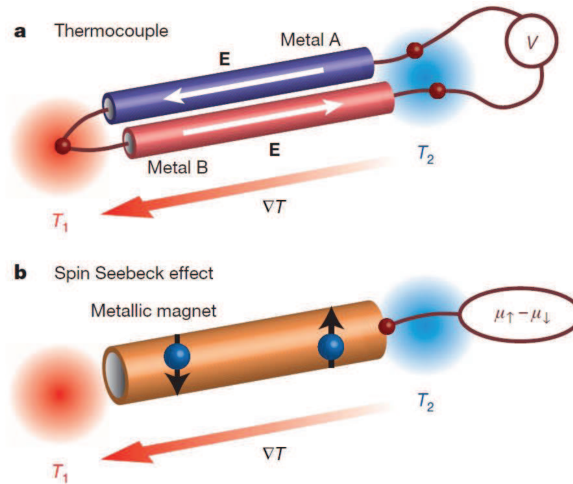

Figure 2.10: a) A thermocouple where an applied temperature gradient on a junction of two metals with different Seebeck coefficients causes a rise of a thermal voltage proportional to the temperature gradient. b) In a magnetic material the spin-up and spin-down conduction electrons have different Seebeck coefficients. Because of that, once subjected to a temperature gradient the magnet would develop a voltage drop, known as the spin Seebeck voltage and it is proportional to the temperature difference. Figure reprinted from ref. [Uchi 08].

generation, while the ordinary Seebeck effect is a charge carrier accumulation, both results of a temperature difference.

The ordinary Seebeck coefficient for metals can be expressed with the Mott formula [Cutl 69]:

$$S = -\frac{\pi^2 k_B^2 T}{3e} \frac{1}{\sigma(E)} \frac{\partial \sigma(E)}{\partial E}\Big|_{E=E_F}, \tag{2.10}$$

where σ is the conductivity. The expression predicts a linear dependence of S on temperature.

Furthermore, Amman *et al.* [Amma 92] calculated the thermopower coefficient for microscopic metallic junctions to be:

$$S = -\frac{\pi^2 k_B^2 T}{3e} \frac{[D_l D_r]'}{[D_l D_r] + \frac{1}{6}(\pi k_B T)^2 [D_l D_r]''}\Big|_{E=E_F}. \tag{2.11}$$

In that expression, D_l and D_r are the normalized density of states of the left and the right electrode. The prime and double prime correspond to the first and second derivative. Thus, S is dependent on the density of states (DOS) at the Fermi level. If the second derivative in the Eq. 2.11 can be neglected, the equation transforms to the old Eq. 2.10, according to which S is linear with T. In addition, the dependence on the DOS suggests that the Seebeck effect could be used as a useful tool in mapping the DOS anisotropies. That property of the thermopower is later used in this thesis to study (Ga,Mn)As-based junctions by means of the Seebeck effect.

Another thermoelectric phenomenon is the Peltier effect. It corresponds to a heat produced or adsorbed in a junction between two metals with different Peltier coefficients, when a current is passed through it. The Peltier coefficient π is defined as:

$$\pi = \frac{q}{I}, \tag{2.12}$$

where q is the rate of heating / cooling and I is the electric current. The Peltier coefficient π and the Seebeck coefficient S are related. Their relation is given with the first Kelvin relation [Thom 54](See Eq. 2.13):

$$\pi = ST. \tag{2.13}$$

Usually, the Seebeck coefficient is the easier to measure [Gold 09]. If S is known, the Peltier coefficient can be estimated using the first Kelvin relation (Eq. 2.13).

The second Kelvin relation connects the thermopower S with the Thomson coefficient τ of the material (junction). The Thomson coefficient is a measure of the rate of heating per unit length for a conductor, in which a unit temperature gradient is established and a unit current is flowing along it. The second Kelvin relation states:

$$\tau = T\frac{dS}{dT}. \tag{2.14}$$

All the thermal coefficients introduced up to this point are defined for a junction of two materials. If the absolute value of a thermal coefficient for a given substance is requested, a superconductor which can be used as a second material in the junction, since a superconductor is regarded as having zero absolute coefficients [Gold 09].

The Peltier and Thomson effects are reversible processes, while the Joule heating and thermal conduction are irreversible [Barn 72]. Both kinds of processes take place simultaneously in a conductor. The Kelvin relations are derived with the assumption that the reversible processes can be treated independently of the irreversible ones. Onsager has further included the irreversible processes into his generalized approach [Onsa 31a, Onsa 31b]. The Onsager method relates the "flows" (current and heat flows) arising in a system to the "forces" (electric field and temperature gradient) present. Using the Onsager relations, Callen [Call 48] derived the Kelvin relations Eq. 2.13 and Eq. 2.14 [Thom 54] and demonstrated the existence of relations among the coefficients in magnetic field. If a magnetic field is present, the coefficients, which are usually treated as scalars, become tensors [Flet 99]. Moreover, when the electrical current J is linear in electric field E and the thermal current Q is linear in temperature gradient ∇T, the following equations based on the Onsager theory are expected to hold:

$$\rho(-B) = \tilde{\rho}(B) \tag{2.15}$$

$$S(-B) = \tilde{\pi}(B)/T \tag{2.16}$$

$$\kappa(-B) = \tilde{\kappa}(B). \tag{2.17}$$

The tilde represents the transpose tensor for each coefficient.

Apart from these relations, another phenomenological relation can be written, where the new effects due to a presence of magnetic field are considered. This relation is:

$$\begin{pmatrix} E \\ Q \end{pmatrix} = \left[\begin{pmatrix} \rho & S \\ \pi & -\kappa \end{pmatrix} + \begin{pmatrix} R_H & N \\ E & L \end{pmatrix} B\times \right] \begin{pmatrix} J \\ \nabla T \end{pmatrix}. \tag{2.18}$$

The first matrix on the right side of the equation corresponds to the earlier introduced Eq. 2.8. The second matrix includes the new coefficients which are the Hall resistivity R_H, the Nernst N, the Ettinshausen E and Righi-Leduc coefficient L. A schematics of the effects described by these coefficients are given in Fig. 2.11.

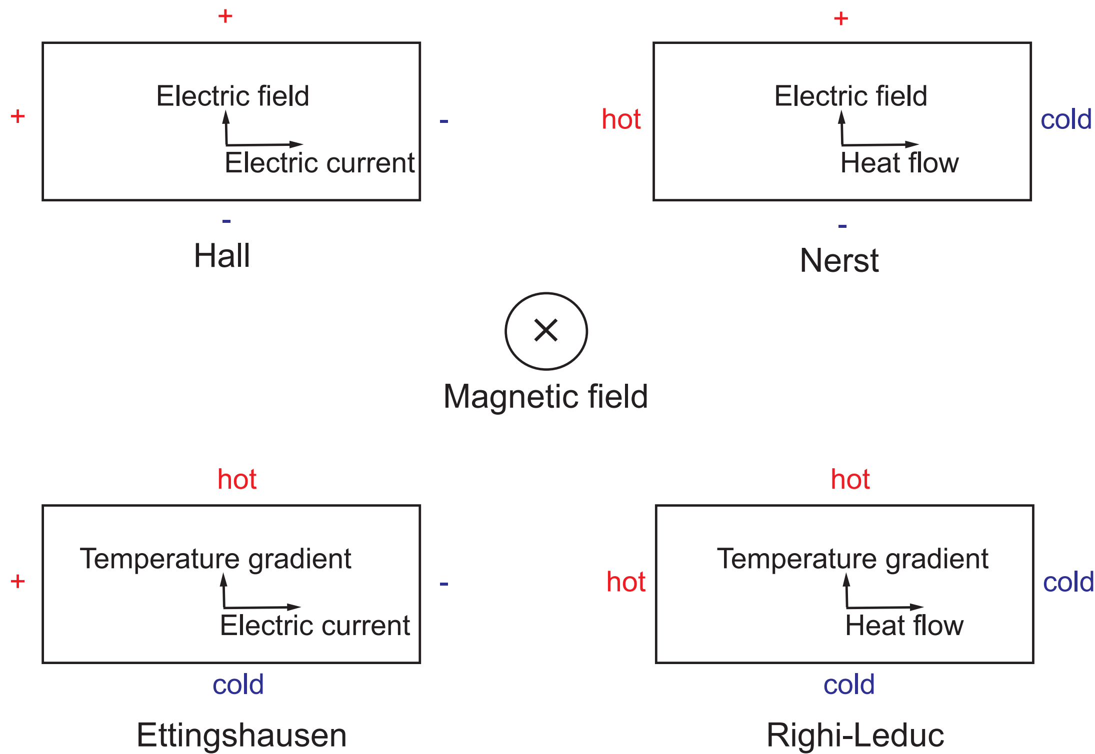

Figure 2.11: Schematic of the effects (thermomagnetic) arising in a conducting sample when an applied magnetic field couples to charge and heat flows. When the effects are in the direction shown in the diagram, the coefficients are positive. Figure according to ref. [Gold 09].

When a transverse magnetic field B_z is applied to a current, an electric field arises perpendicular to both the current and B_z. That describes the Hall effect and the sign of the characteristic Hall resistivity R_H depends on the type of the charge carriers. If instead of a charge current, a longitudinal temperature gradient or heat flow is applied perpendicular to a B field, a transverse Nernst voltage develops. Under the conditions of no temperature gradient along the direction of the detected thermomagnetic voltage and no electric current in any direction, the Nernst coefficient N is defined as follows:

$$|N| = \frac{dV/dy}{B_z dT/dx} \tag{2.19}$$

The Nernst effect is similar to the Hall effect, however its sign does not depend on the type of the carriers. The coefficient N is dependent on mobility, scattering mechanism and degree of degeneracy [Delv 65]. In magnetic materials, as it will be discussed later in detail, an anomalous Nerns effect (ANE) can occur. Its dependence on the scattering mechanism was used to probe the existing theory on the anomalous Hall effect (AHE). It was shown that AHE and ANE share common origin [Pu 08, Naga 10].

Another thermomagnetic effect is the Ettingshausen effect. It corresponds to a generation of a temperature gradient perpendicular to the plane defined by the applied magnetic field and a current flowing in a conductor, perpendicular to the field. Accordingly, the coefficient E [Gold 09] is equal to:

$$|E| = \frac{dT/dy}{i_z B_z}. \tag{2.20}$$

The Peltier and Ettingshausen effects are very small and they are usually swamped by some irreversible effects like Joule heating [Delv 65]. That is why it can be a challenge to measure them. A relationship, known also as Bridgman's relation, has been found between the Nernst N and the Ettingshausen E coefficients [Call 48]:

$$TN = \kappa E, \tag{2.21}$$

where κ is the thermal conductivity. That is used to estimate E when N is known.

To complete the picture of the first order thermomagnetic effects the Righi - Leduc effect has to be mentioned. That is the manifestation of a temperature gradient perpendicular to a plane of a heat flow and a magnetic field in a material:

$$|L| = \frac{dT/dy}{B_z dT/dx}. \tag{2.22}$$

This effect was expected to be only due to electrons. However, its amplitude has been found to be limited by the lattice thermal conductivity [Delv 65].

In general the thermonagnetic effects are difficult to measure and even to be correctly identified. Moreover, when the material of interest is magnetic in nature, the coupling of magnetization and heat can result in some new anomalous effects. Recently, the physics of the heat currents in combination with the spin nature of the electron became topic of the new field of spin caloritronics, introduced in the next section.

2.4 Magnetic materials and thermal effects, spin and heat coupling - spin caloritronics

The applications of thermoelectricity cover temperature sensors, power generators and coolers. However, their efficiencies seem to be limited [Baue 12, Goen 12]. The second degree of freedom of the electron - its spin - promises a possible way of further increasing these efficiencies. Coupling between the spin and the heat flow was predicted already by Johnson and Silsbee in 1987 [John 87]. Together with the detection of the spin Seebeck effect (SSE) (See Fig. 2.10) in Py thin films [Uchi 08] in 2008, which is a generation of a spin current due to a temperature gradient, these works initialized the new research field of spin caloritronics. The field covers different phenomena classified as (a) independent electron, (b) collective and (c) relativistic effects [Baue 12]. The effects studied in this work belong to the last group of phenomena. A sketch combining electron and spin - dependent thermal effects and the relations between them is presented in Fig. 2.12.

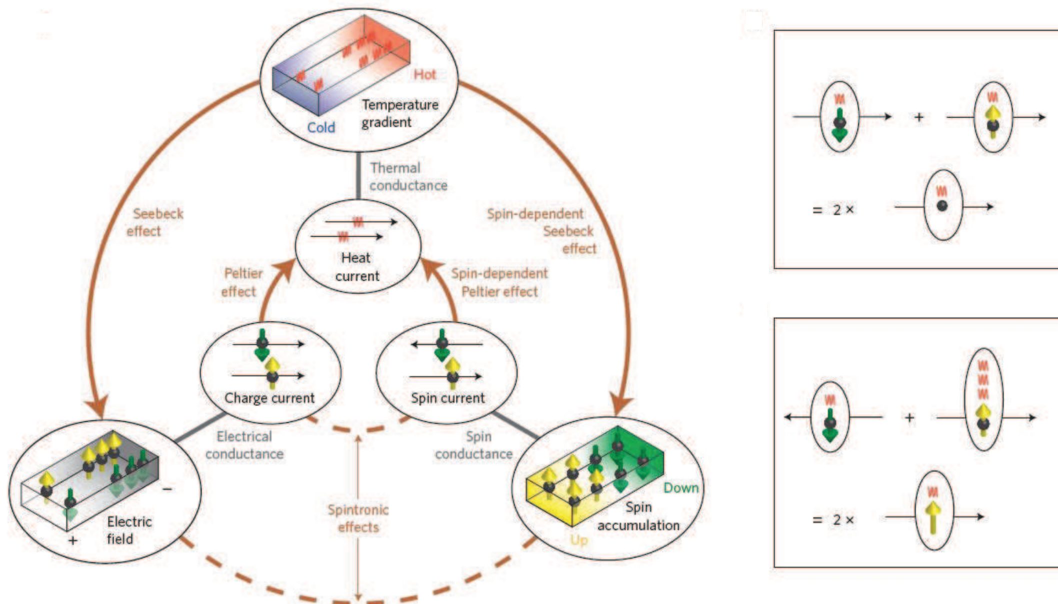

Figure 2.12: Left - conventional (due to charge carriers) vs. spin - dependent (due to spin) thermoelectricity. Right - a comparison between the heat per unit carrier for nonmagnetic (top) and magnetic (bottom) materials. Figure reprinted from ref. [Goen 12]

Based on their experiments, Flipse *et al.* found a difference in the amount of heat carried by a spin-up and a spin-down electron [Slac 10]. The same authors confirmed the validity of the Onsager - Kelvin relation for the spin-dependent Peltier and Seebeck coefficients in Py [Flip 12]. However, the physics of the spin-governed thermal effects remains still debatable and controversial, especially the nature of the lately discovered SSE [Uchi 08, Uchi 10b, Jawo 11, Schm 13]. Along with that, some of the thermal effects are still not measured. The above presented effects: Hall, Nernst, Ettingshausen and Righi

- Leduc are expected to have in total of about 16 variations - normal, planar, anomalous and a spin version [Le B 11]. Each of the effects relates three vector quantities from that list: thermal gradient, electric field, spin current, spin, magnetic field or magnetization. The effects which involve spin or magnetization are main subjects of the spin caloritronics. The latter promises a possibility for new thermoelectric devices, like the spintronics led to new types of electronic devices [Goen 12].

This work is devoted to the study of two thermoelectric / thermomagnetic effects in a ferromagnetic (Ga,Mn)As / GaAs tunnel junction. These are the thermopower and the Nernst effect. Both of the effects are found to be governed by the anisotropies of the (Ga,Mn)As density of states and possible applications are discussed.

Chapter 3

Diffusion Thermopower of (Ga,Mn)As/GaAs Tunnel Junction

This part of the thesis reports on the diffusion thermopower of a (Ga,Mn)As/GaAs tunnel junction. The phonon-drag contribution to the thermopower is minimized by designing the p-n junction interface and applying the heat directly to the electron system. The voltage response to a temperature difference in this junction is related to the energy derivative of the densities of states (DOS) in the magnetic material and thus found to be strongly anisotropic to the direction of the magnetization in the material. The dependence of the thermopower on derivative of the DOS makes it a useful tool for mapping the DOS, which is of particular interest for samples near the metal-insulator transition. The observed effect might be also relevant for the interpretation of some earlier spin injection studies. Parts of this chapter are also published in [Nayd 11].

3.1 Thermopower in (Ga,Mn)As - short overview

Major issues of modern information technologies are power consumption and heat dissipation. Recently, it was shown [Bakk 10, Nayd 11] that thermal effects can affect device operation, in particular the injection of spin polarized current into a nonmagnetic semiconductor [Lou 07, Cior 09]. Together with the initial reports on the spin Seebeck effect in metals [Uchi 08] and subsequently in magnetic semiconductors [Cior 09, Jawo 10], these topics developed as a building block for a new field of spin caloritronics [Baue 10].

Apart from being an obstacle, thermal effects can bring useful information about material properties and their electronic structure. They can be utilized to measure temperature or to generate heat locally at or close to an interface between different materials. For instance thermopower analysis gives information about carrier transport mechanism in layers with both metallic and non-metallic types of conductivity and allows determination of the carrier concentration and Fermi energy. The latter is still a hotly debated issue for (Ga,Mn)As layers and additional experiments are always helpful in this discussion

([Sliw 11] and citations therein).

There are not many experimental works on thermopower in (Ga,Mn)As. One of them is presented by Pu et al. [Pu 06] where they study the anisotropies of the thermopower in (Ga,Mn)As and report a new phenomenon named Planar Nernst Effect (PNE). Applying a step heating method, a temperature difference is created along Hall bars with a width of 0.1-1 mm. These are patterned along the [$\bar{1}$10] and [110] directions by means of standard photolithography. The Seebeck effect was measured when a magnetic field is swept in-plane. Longitudinal thermopower S_{xx}, which was measured along the direction of the temperature gradient, showed clear saturation when increasing the magnetic field (See Fig. 3.1). This is in contrast to the resistivity (unique for ferromagnetic semiconductors [Mats 04]) which strongly depends on H even above saturation of the magnetization (See Fig. 3.1).

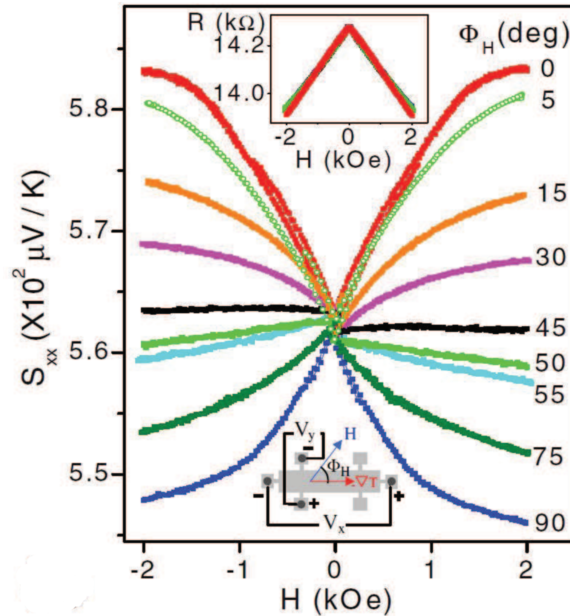

Figure 3.1: Angular dependence of the longitudinal magnetothermopower S_{xx} at 6 K; the sample is $Ga_{1-x}Mn_xAs$ (x = 0.039). The heat flow is applied in the [$\bar{1}$10] direction. Top insert shows the angular dependence of magnetoresistance of the sample, and the bottom inset is a sketch of the relative orientation of the heat flow -∇T and the external H. Figure reprinted from ref. [Pu 06]

As noticeable from Fig. 3.1, S_{xx} approaches the same final value S$\|$(S$\perp$) as long M is oriented parallel (perpendicular) to the direction of heat flow no matter whether M lies [110] or [$\bar{1}$10], or which path S_{xx} actually takes to the final saturation value. The magnitude of S_{xx} did not show a dependence on which crystallographic direction the magnetization lies, opposite to tunnelling anisotropic resistance in (Ga,Mn)As reported by Gould et al.([Goul 04]). Longitudinal magnetothermopower S_{xx} and the transverse magnetothermopower (the PNE) S_{xy} are shown to share common origin, which is related to the anisotropic scattering rate in the ferromagnetic phase of the diluted magnetic

semiconductor. From this study it can be seen that a large value for the bulk Seebeck coefficient of about 100 - 500 μV/K was measured. This was found to be in agreement with the calculations using microscopic scattering theory, implying a strong particle - hole asymmetry in the system [Hals 10].

Similar bulk values for the thermopower were presented in the work of Osinniy et al. [Osin 04]. In their study the thermopower measurements were done on a 10$\times$3 mm^2 piece of (Ga,Mn)As wafer. They applied a temperature difference of 0.4-2 K and monitored that difference by fine Au:Fe-chromel thermocouples attached to the (Ga,Mn)As layer by conducting silver paste. Some results for the thermopower are presented below in Fig. 3.2.

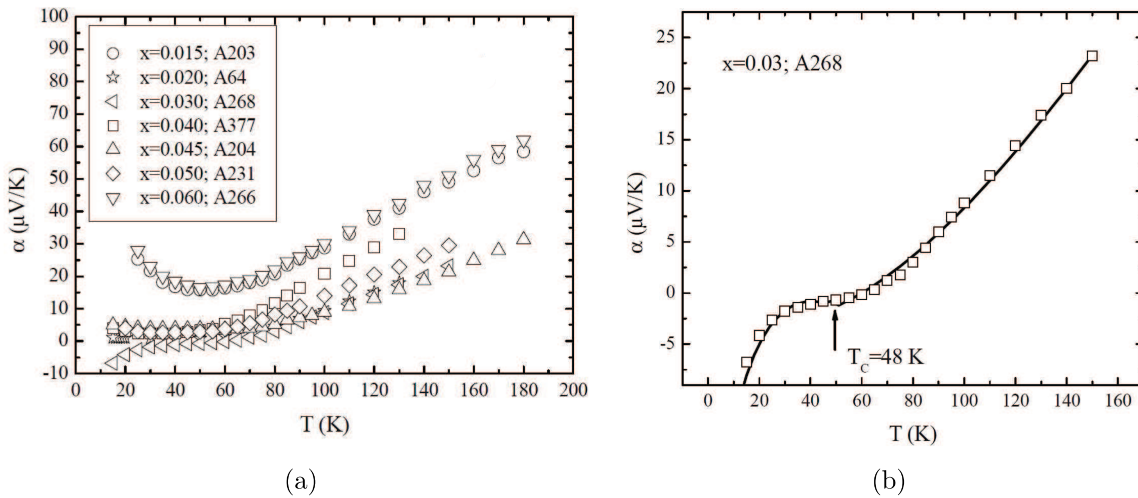

Figure 3.2: Temperature dependence of the thermoelectric power in (Ga,Mn)As layers. The line in the second figure on the right show fitting by a theoretical model involving diffusion, paramagnetic Kondo, and ferromagnetic Kasyua contributions. Figure reprinted from ref. [Osin 04]

Deviation from the linear behaviour is observed for the thermoelectric power in the samples with metallic type of conductivity in the low temperature range. An example is shown in Fig. 3.2b, where an addition contribution to the thermoelectric power is observed with a maximum close to the Curie temperature. This ferromagnetic contribution is described by the Kasuya model developed for thermoelectric effects in metallic systems with sp - d exchange coupling [Kasu 59]. The high temperature data are then use to determine the Fermi level position. That was found to reside 220 meV below the top of the valence band, whereas for samples with non-metallic type of conductivity, the Fermi energy value decreases by about 50 meV. These calculated values of the Fermi level in (Ga,Mn)As further support the valence band model ([Sliw 11] and citations there).

For both of the above presented works bulk thermopower was measured. The diffusion contribution to the thermopower in those cases, however,was not directly measured and additional contributions from drag effects were present in the above geometries. This

carrier-related thermopower probes the energy derivative of the (Ga,Mn)As density of states (DOS) and thus provides a way to directly measure it.

In this chapter a device design and measurements on diffusion thermopower at (Ga,Mn)As /LT GaAs/ GaAs interface will be presented. Before continuing with the main topic of this chapter, we will give some light on what is actually diffusion thermopower and how it can be distinguished from the other contributions to the thermopower.

3.2 Diffusion thermoelectricity and phonon drag

In general thermoelectric power contains diffusion and phonon drag contributions, as well as, in the ferromagnetic case, a magnon drag term. The magnitude of the drag terms scales with phonon and magnon relaxation times, so that they dominate at low temperatures, particularly in annealed (Ga,Mn)As samples. For example, a reduced concentration of the Mn interstitials may suppress relevant scattering [Sliw 11].

A main point here will be the difference between the two thermopower components - diffusion and phonon drag terms, in particular their temperature dependence.

Diffusion thermopower in metals is generally described with the Mott-relation [Cutl 69]:

$$S = -\frac{\pi^2 k_B^2 T}{3e} \frac{1}{\sigma(E)} \frac{\partial \sigma(E)}{\partial E}\Big|_{E=E_F}, \tag{3.1}$$

where σ(E) is the energy dependent electrical conductivity and T is the temperature. This relation is the case for temperatures $T < \theta_D$ (Debey temperature) as predicted from the free electron theory and no startling features are expected in the S-T relation at low temperatures. According to this theory, higher temperatures would result only in a change of the dS/dT slope. Thus according to Eq. 3.1, the diffusion thermopower is generally linear with temperature, depends on the Fermi surface and on the scattering mechanism. The above relation examines only an electron movement in response to an applied temperature gradient. The lattice is assumed to be in equilibrium and transport properties resulting from the temperature gradient in the lattice are ignored. This means a phonon system to be in equilibrium and implies strong interaction between phonons and other phonons, dislocations, boundaries and impurities. When such a strong interactions exist, from a thermoelectric point of view, the phonon system can be safely ignored. Under this quasi-equilibrium condition of the phonons that we regard, the thermopower is regarded as arising from a diffusion process, the so called diffusion thermopower. Phonon-phonon interaction increases with temperatures and it becomes dominant at temperatures $T > \theta_D$. An experimental evidence however, does not support the neglected lattice contribution and in fact in the low temperature region the thermopower of metals is found to contain a large number of unusual effects which the simple theory cannot explain. Apart from a anomalous scattering from residual impurities, there are still some features which remain also in highly pure metals extending up to room temperatures. These features usually take the form of a 'hump'in the thermopower - temperature dependence and it

may be positive or negative in sign [Barn 72]. That is explained in terms of a phonon drag effect which give rise to an additional term in the thermopower. When a temperature gradient is present, there is a higher density of phonons at the high temperature end with the metal than at the end with lower temperature. That results in a flux which is analogous to that existing in the electron system. It is the same phonon flow which provides the thermal conductivity of insulators. The flux by itself cannot make any direct contribution to the thermoelectric effects because phonons carry no electric charge. Nevertheless, when the two flows (carrier and phonon) exist, they are not independent. An interaction is present and it is both ways. The phonon system absorbs the energy and the momentum of the electrons moving along an electrochemical potential gradient or a temperature gradient existing in the system. Electrons can absorb phonons. The last is of lesser importance compared to the phonon emission process, as is exemplified by the production of Joule heat. At low temperatures, when the phonon-phonon interactions are less abundant, a non-equilibrium of the phonons is possible. When a temperature gradient is present in a system, the phonon flux occurring can impart momentum and energy to electrons rather than to the lattice. This happens via phonon - electron interaction. The imported additional net momentum results in a modified thermal e.m.f.. Phonon flow drags electrons with it and extra electrons tend to pile up at the cold end over and above those electrons which are there as a result of the diffusion process. The phonon drag effects are strongly dependent on temperature. In addition, they become smaller when the carrier concentration increases. This is partly due to the scattering of charge carriers on the donor or acceptor impurities, and more significantly, due to the so-called saturation effect. When the carrier concentration is high, momentum is increasingly transferred back to the electrons from the phonons [Gold 09].

In summary, diffusion thermopower is linear while phonon drag contribution to the thermopower is mainly non-linear with respect to temperature. Thus, measurements of the temperature dependence are a possible test to distinguish the two contributions to the thermoelectric power. In this work we present a device where the diffusion thermopower is measured. It consists of (Ga,Mn)As - GaAs tunnel junction. The phonon-drag terms are minimized through three layers heterostructure such that the phonon flow is strongly confined in between different interfaces. In addition to this, a current heating technique will be applied to selectively heat the electron system without heating the lattice. This issue is of a main concern in the next section. The advantages of the heating current technique will be discussed.

3.3 Heating current method

Different techniques are applied to create temperature difference or thermal gradients in materials and devices on the way of studying their thermoelectric properties. This includes laser heating [Walt 11], heaters directly or indirectly connected to the device

of interest [Lieb 11, Pu 08], and as well the heating current technique [Gall 90, Jong 95, Mole 90]. Among those methods, the heating current technique is the one which is chosen for the experiments in this work. The reason for that is the following. A significant temperature gradient in lattice temperature gives thermoelectric voltages of a few nanovolts which is in the same order as the Johnson noise [Gall 90]. On the other hand, increasing lattice temperature might lead to increased electron-phonon scattering and thus additional phonon drag effects. At elevated temperatures, phonons, electron-hole exitations and magnons co-exist and carry heat currents in parallel and coupling of different modes can be important for the thermoelectric phenomena [Baue 12]. To minimize the influence of these "side effects" and to measure the actual diffusion contribution to the thermopower in a material/device, a current is applied and directly heats the electron population without significantly affecting the lattice temperature. Selective Joule heating of electrons is then possible when the electron-phonon coupling is weak [Hout 92]. Based on this knowledge, a device design is presented in Fig. 3.4. It contains a Si-doped GaAs channel in which the temperature of the electron system is heated out of equilibrium with respect to the GaAs lattice by a low frequency ac current. The temperature of the electrons in the channel is later estimated using a quantum-mechanical effect as a thermometry tool. This effect is the weak localization effect and it is described in the following section.

3.4 Weak Localization

As a thermometer of the electron temperature in our device, the weak localization effect (WL) is utilized. In the following, a brief description of the physics of the effect is given.

WL deals with anomalous transport properties of electrons in disordered systems ([Berg 84]). It exists in one, two and three dimensions. For experimental investigation the most favourable is the two-dimensional case. The phenomenon is essentially caused by quantum-interference of the conduction electrons scattered by the defects in the system. Physically it represents an interference experiment with the conduction electrons split into pairs of waves interfering with the backscattered direction [Berg 83]. Fig. 3.3 gives a schematic representation of the WL effect.

The intensity of the interference (integrated over time) can be measured by the resistance and this usually is observed as anomalies in the resistance. The correction to the last is of order of 10^{-2} to 10^{-3} and can be easily measured with accuracy of 1%. It was found that the resistance of thin disordered films as a function of temperature is increasing with the logarithm of the (decreasing) temperature. One possible explanation was the WL, but an alternative mechanism was also suggested to account for this dependence - the effect of Coulomb interaction [Alts 80]. Thus more characteristic experimental investigation of WL was needed. The application of magnetic field provided such a possibility.

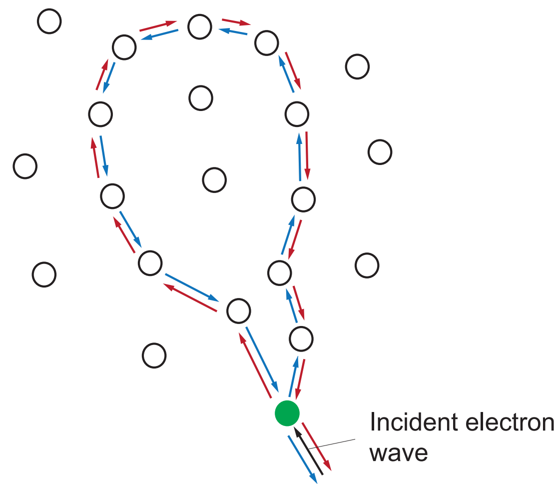

Figure 3.3: If an injected electron follows the path indicated with blue arrows, its quantum mechanical time-reversal image is also present (red arrows) with the same probability. A constructive interference can occur between the two paths, which results in an enhanced backscattering probability. That is the mechanism for the Weak Localization effect.

A magnetic field introduces a magnetic phase shift in the electronic wave function. That suppresses the interference and thus the localization. The resistance changes when a magnetic field is applied perpendicular to the film. On the other hand, the magneto-resistance is strongly temperature dependent. The response to a magnetic field is used to determine the characteristic times of the electron systems.

Based on that knowledge, the WL effect is used as a tool for measuring the local electron temperature in the heating channel of devices measuring the Seebeck and the Nernst effect in a (Ga,Mn)As/GaAs tunnel junctions. The results from the WL experiments for the Seebeck geometry are presented later in this chapter.

This work is organized as follows. First, a design and sample fabrication are described. At the second place, different measurements are presented and a value for the Seebeck coefficient of the junction is estimated. To complete the picture of the measured diffusion thermopower, a simple cartoon model is introduced in order to describe the measured system.

3.5 Design and Sample Fabrication

The device for measuring the thermopower of a (Ga,Mn)As tunnel junction consists of 20 nm thick single magnetic (Ga,Mn)As contact, separated from a highly doped Si:GaAs mesa (60 nm) by a 1 nm low-temperature GaAs spacer. The semiconductor layers are grown on a semi-insulating GaAs substrate and buffer by means of low-temperature molecular beam epitaxy, as shown in Fig. 3.4. Subsequently, and without breaking the vacuum, the sample is transferred to a UHV electron-gun evaporation chamber where Ti/Au (5 nm/30 nm) contacts are deposited on the (Ga,Mn)As layer. The growth is done

by Lars Ebel. The active manganese concentration is approximately 2% as determined from SQUID measurements.

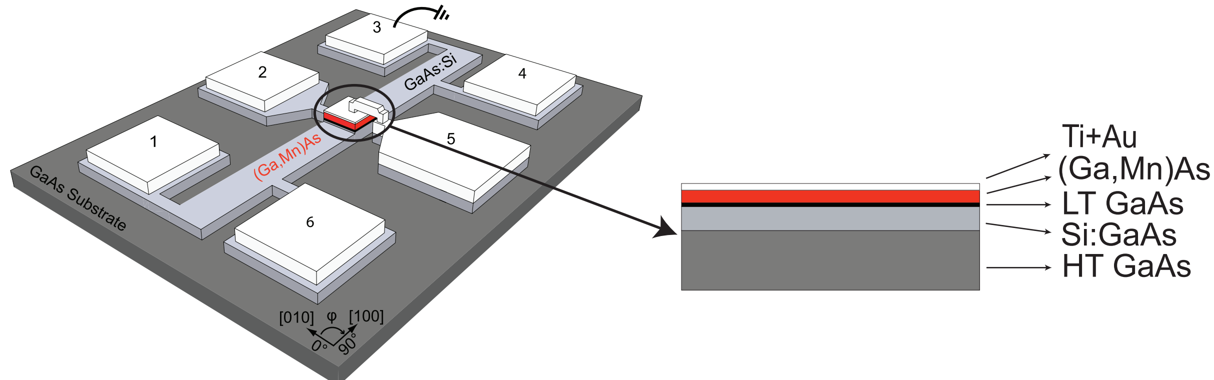

Figure 3.4: Schematic of the used layer stack (on the right) and the tunnelling anisotropic magnetothermopower (TAMT) device (on the left). The crystal directions are given with arrows. A heating current is applied on the Si:GaAs channel and the thermalvoltage is detected between contacts "2" and "5".

The as-grown sample is patterned into the shape depicted in Fig. 3.4 using a multi step optical lithography and etching process. The design and fabrication process are developed by Kia Tavakoli. As a first step a 50×50 μm^2 square of optical resist is defined on the sample surface using E-beam lithography and UV-light exposure. The edges of the square are parallel to the [100] and [010] crystal directions in (Ga,Mn)As. After developing the area around the square is dry etched to reach the Si doped GaAs. For that argon ion etching, HF dip and BCl_3 chemical assisted ion etching (CAIBE) are used. Once the junction is defined, a heating channel is established through optical lithography and etching with BCl_3 plasma. The channel is oriented along the [100] crystal direction and its width is 50 μm. Contacts are established by Ti/Au evaporation and lift-off. The top of the pillar is connected to a bonding pad through a gold air bridge fabricated using electron-beam lithography and a multiple acceleration voltage process [Borz 04]. The ready sample is then glued and bonded in a chip carrier.

3.6 Electrical Characterization of the (Ga,Mn)As / GaAs Tunnel Device

This section describes the measurements of the thermopower a ferromagnetic / non-magnetic semiconductor tunnel junction. Transport measurements are performed at 4.2 K in a variable temperature magnetocryostat fitted with a vector field magnet that allows for the application of a magnetic field of up to 300 mT in any direction.

Once the sample is cooled to 4.2 K, a current - voltage (IV) curve is measured across the junction in a 2 terminal configuration. The junction, as describe before, consists

of a low-temperature grown insulating GaAs layer in between (Ga,Mn)As layer and a Si doped GaAs channel. The IV-curve is presented in Fig. 3.5. It shows a non-linear behaviour. This non-linearity is in agreement with one of the criterion defined from Rowell to identify a tunnelling barrier [AAke 02]. This is an important issue on the way to measure the characteristic electron contribution to the thermopower of the system with minimized phonon-drag contribution.

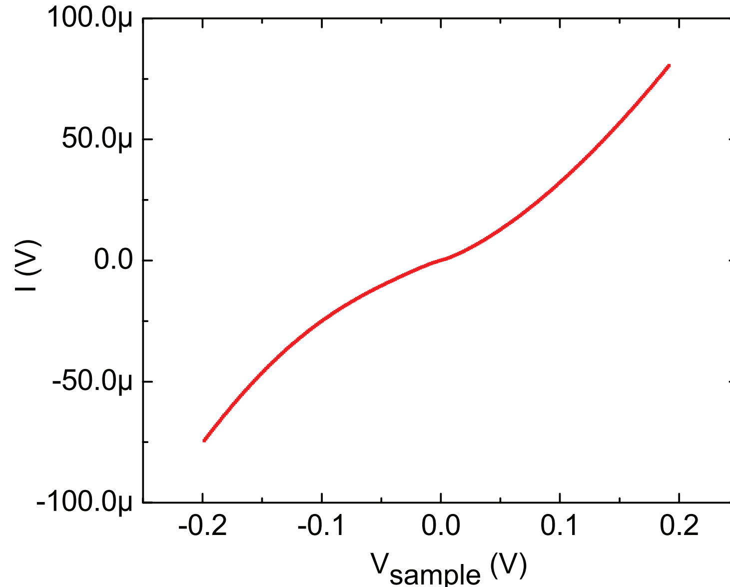

Figure 3.5: IV-curve measured at 4.2 K in 2 terminal configuration between contacts "2" and "5" (Fig. 3.4). No external magnetic field is applied.

A thermovoltage occurs when a temperature gradient is established across the junction. To create such a gradient, an ac heating current technique is used. A 13 Hz sine signal is applied across a GaAs heating channel (Fig. 3.4). The electron system is then heated out of equilibrium with respect to the GaAs lattice, while the (Ga,Mn)As contact remains at 4.2 K. The last statement is supported later in the text with an experiment where the thermal voltage is recorded as a function of magnetic field swept along different angles with respect to (Ga,Mn)As crystal directions. The thermal voltage response to the magnetic field is combined in a fingerprint plot. This anisotropy fingerprint of the (Ga,Mn)As remains unchanged when applying a higher heating current and is shown to be similar to the one measured in AMR configuration at 4.2 K [Papp 07a]. Here we would like to emphasize that the thermal voltage is measured over the junction where no current is flowing.

As a next step, a Hall measurement is done on the heating channel to estimate the carrier concentration in the channel. The result is used in the introduced cartoon model for the thermopower. The Hall resistance at 120 K is measured in the following configuration: current is sent between contacts "6" and "3", and the voltage is measured between "4" and "2" (see Fig. 3.4). Due to lithography imperfections, the contacts "4" and "2" are not

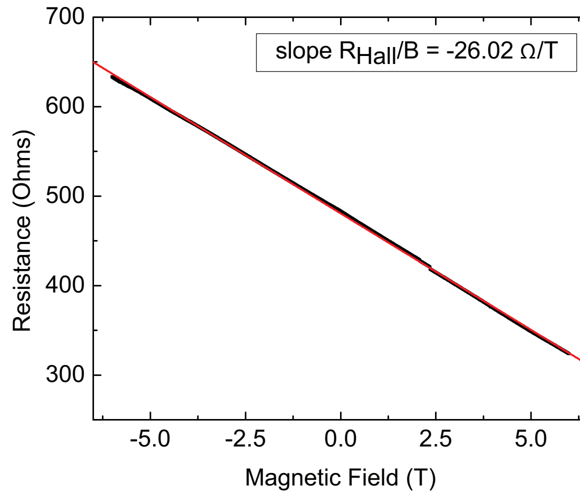

Figure 3.6: Raw data resistance measurement in a Hall geometry. Black stands for the experimental data, whereas red is for the linear fit.

aligned one against the other, like in a perfect Hall geometry. There is a lateral distance between the contacts. That results in a longitudinal pick up on top of the Hall resistance. That longitudinal resistance is symmetric with the applied out-of-plane magnetic field is applied, while the Hall effect is an asymmetric with magnetic fields. The longitudinal resistance pick-up is obvious in the Hall resistance measurement shown in Fig. 3.6. The red line is a linear fit to the experimental data points (in black). From the slope of the linear fit, the charge carrier density in the Si-doped GaAs channel is estimated to be $n = 4.0 \times 10^{18}$ cm^{-3}.

Applying a heating current on the GaAs channel results in temperature difference ΔT across the tunnel barrier. That generates a thermal voltage V_{th}. The latter is detected between contacts "2" and "5", as shown in Fig. 3.4. The amplitude of the thermal voltage depends on ΔT, or equivalently on the electron temperature in the GaAs channel. The heating is performed at sufficiently low frequencies that the electron temperature remains in quasistatic equilibrium and follows the applied power. This means that the thermal voltage will be related to the square of the applied voltage. The relationship is measured and presented in Fig. 3.7. It includes the thermal voltage measured for different heating voltages when a magnetic field of 300 mT is applied in-plane for different angles. The detection of the thermal response to the heating current is performed at double the heating signal frequency 2f, using a standard lock-in amplifier technique. The thermal voltage V_{th} for different angles is plotted versus the square of the applied voltage . From the plot, it can be seen that V_{th} for all of the presented angles has a linear dependence on the $V^2_{applied}$ or on the applied heating power. A blue line is drawn to guide the eye.

As a next step the temperature of the electrons in the heating channel is determined by means of a Weak Localization measurements.

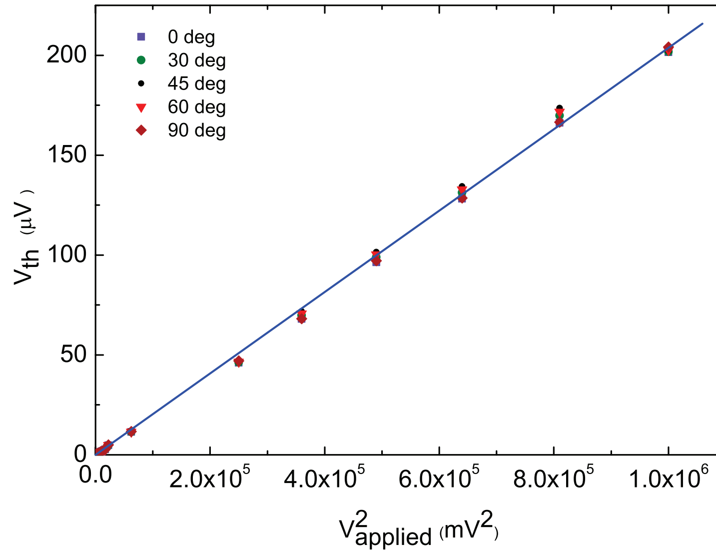

Figure 3.7: Thermal voltage as a function of the applied heating power in the Si:GaAs channel. A magnetic field of 300 mT is applied along different in-plane directions. The blue line is drawn to highlight the linear dependence for different magnetic field directions. The 0° direction coincides with the [010] crystal direction.

3.7 WL Measurements of the electron temperature

A heating current heats the electrons in the GaAs channel while the (Ga,Mn)As stays relatively at bath temperature. This is later proved by using the fingerprint method to map the anisotropies of the layer. To establish the relation between heating voltage / power and the electron temperature, a tool to measure that relation is needed. As a thermometry for the electron temperature, the weak localization (WL) effect is selected. Weak Localization measurements are performed at different bath temperature and at different heating voltages. In both cases an ac heating current of 13 Hz passes through the channel between contacts ”3” and ”1”, and the resistance of the same bit of the channel is measured when an applied out-of-plane magnetic field is swept from -300 mT to +300 mT.

First, we performed a measurement, where the bath temperature is changed, meaning the surrounding temperature of the whole device and in particular the (Ga,Mn)As layer. A sufficiently low heating voltage of 150 mVpp at a frequency of 13 Hz is used. While the magnetic field is swept out-of-plane, the voltage drop across the heating channel is recorded. Knowing the value of the reference resistance which is connected in series to the device, the heating current and then the resistance of the GaAs channel are calculated. Different bath temperature result in different weak localization features. To compare them, the resistance of the channel is normalized to the value of the resistance at zero magnetic field for the various temperatures measured. In Figure 3.8a the normalized channel resistance is plotted with respect to the magnetic field. One can be seen is that

increasing the bath temperature leads to an increased value of the width or the area of the weak localization feature. As a comparison, the width of the peak at 99.85% of the zero field resistance value is used. That value is chosen instead of the full width of half maximum (FWHM) because the FWHM can not be extracted it this case. The reason for this is that the measured WL curves are not saturated. To saturate the WL curves higher magnetic fields are required but not available for the limited magnetic field of this set-up.

The width of the curves from Fig. 3.8a are extracted and then plotted with respect to the bath temperature in Figure 3.8b. The data points correspond to the extracted widths and the red line represents an empirical fit for the investigated temperature range. This fit has no physical meaning and it is described best with a parabola. Nevertheless, a simple relation between temperature and width of the weak localization peak is established. The fitting parameters of the parabola are used later for the calibration of the electron temperature for different heating voltages.

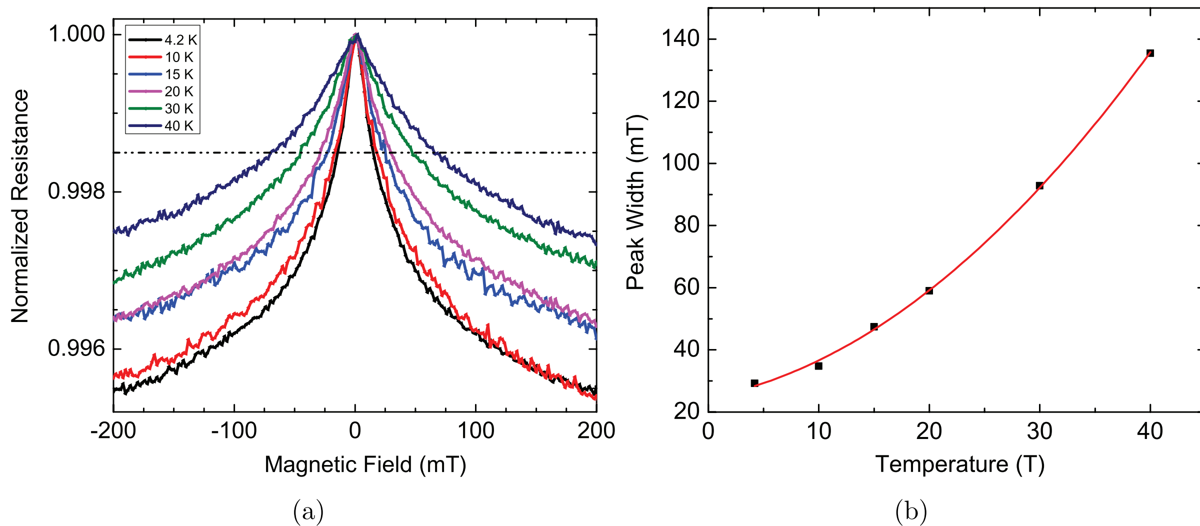

Figure 3.8: (a) Normalized channel resistance as a function of magnetic field for different bath temperatures. (b) Width of the WL feature plotted versus temperature (in black). The red curve represents an empirical fit to the extracted data points.

Subsequently, a WL experiment for different heating voltages ($V_{applied}$) at bath temperature of 4.2 K are performed. The resistance of the GaAs channel for magnetic sweeps for various $V_{applied}$ is calculated and normalized. The curves are shown in Fig. 3.9.

Different heating power results in a different width/area of the weak localization peak. As the heating voltage is increased the width of the feature is increased. The latter is extracted and the conversion width - temperature is estimated using the empirical fit parameters from the previous measurement. The obtained temperature vs. the applied voltage dependence is presented in Fig. 3.10. Higher heating voltage means higher carrier temperature. The experimental points are plotted together with the estimated error on

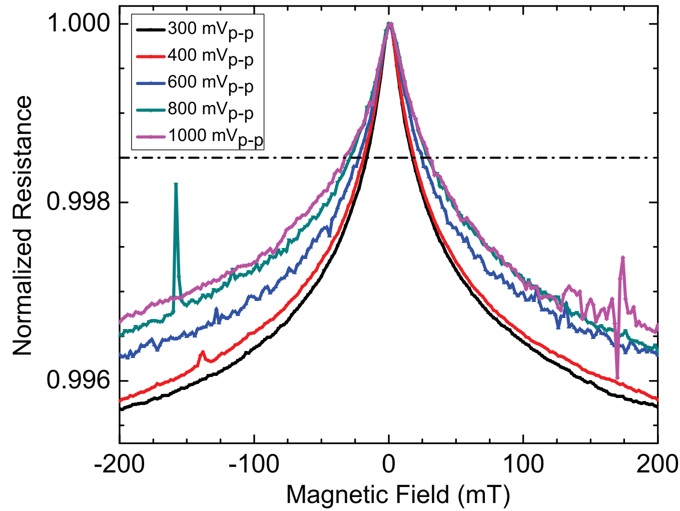

Figure 3.9: Normalized channel resistance versus applied magnetic field for different heating voltages.

them. The red line represents a fit based on the following assumptions: when no voltage is applied the temperature remains at bath temperature, in this case 4.2 K. Another assumption is that the temperature increase should be a power law of the square of the heating voltage. Taking these assumptions into account, a power function is found to relatively good describe the observed voltage dependence of the temperature. Two additional curves are drawn to visualize the estimated accuracy on the temperature as a function of the applied voltage. It is found that a heating areal current density of 5.5 A/m ($\approx$ 9.2 kA/cm^2) on the heating channel corresponds to an electron temperature of $\approx$ 22 K, with an estimate accuracy of about $\pm$1.5 K

3.8 Thermopower and Seebeck coefficient

The thermovoltage between contacts "2" and "5" is recorded at 4.2 K when a magnetic field of 300 mT is rotated in-plane and various temperature differences ΔT are applied. The temperature difference across the barrier is determined from the WL measurements. The thermal voltage angle dependence for different temperature differences is presented later in this work. At this point, only the value of the thermal voltage is extracted for various angles and plotted Fig. 3.11a with respect to the temperature difference. The dependence is non linear and the 0°-curve is fitted using a simple power function which value is zero when ΔT = 0. It is obvious that the measured thermal voltage is temperature dependent. Is a magnitude is in the μV range and that is comparable to the background voltages typically observed in the nonlocal measurements of other studies on spin-injection/spin-detection described earlier in this work.

Subsequently we divide the V$_{th}$ for the given angles by the estimated ΔT. That gives

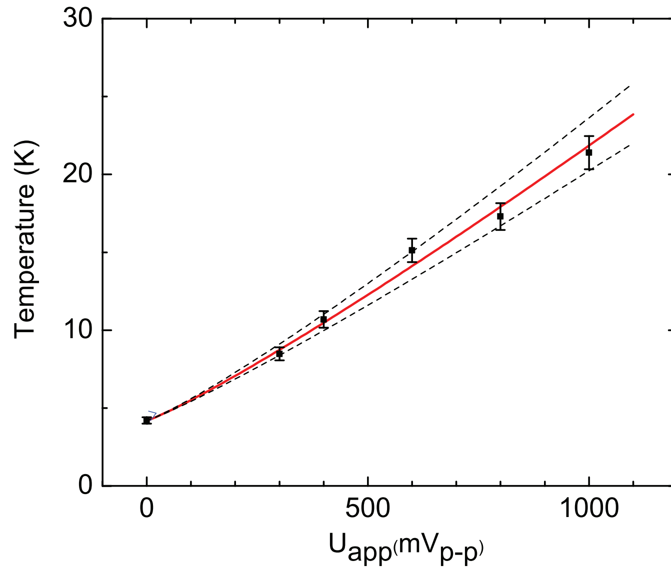

Figure 3.10: Temperature vs applied voltage dependence. Black squares with the corresponding error bars represents measured data. The red curve is the fit and the dash lines are the estimated accuracy.

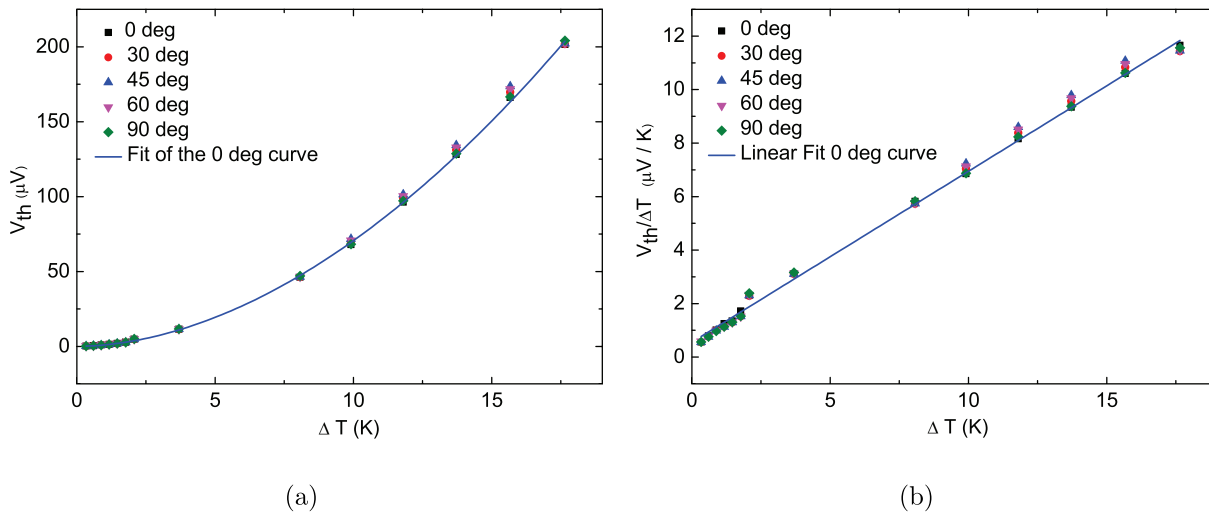

Figure 3.11: (a) Thermal voltage as a function of the temperature difference / electron temperature in the n doped GaAs channel for magnetic field of 300 mT applied along different in-plane directions. The blue curve is an empirical fit of the 0° data. (b) Thermopower vs ΔT for different field directions. Linear fit of the 0° curve is given by the blue line.

the value of the thermopower $\zeta = \frac{V_{th}}{\Delta T}$. The latter is plotted as a function of temperature gradient in Fig. 3.11b for various magnetic field directions. Figure 3.12 presents only for the 0°-curve and it contains. Figure 3.12 contains information about the estimated accuracy.

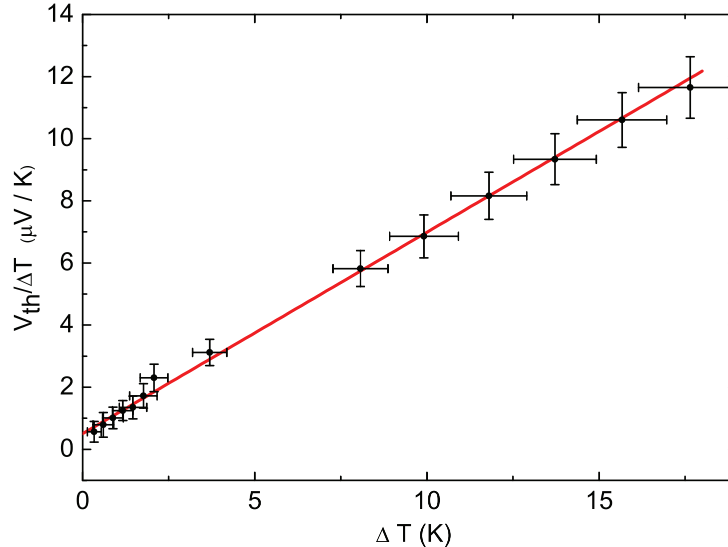

Figure 3.12: Amplitude of the thermopower signal as a function of the temperature difference across the junction.

The linear fit intercept with the y axis $S(4.2\text{ K}) = \lim_{\Delta T \to 0} \zeta = \frac{V_{th}}{\Delta T}$ yields a Seebeck coefficient of 0.5 μVK^{-1}. This number represents the diffusion part of the Seebeck coefficient at 4.2 K and is 3 orders of magnitude smaller than the phonon-drag dominated Seebeck coefficient measured in (Ga,Mn)As by Pu et al. [Pu 06]. This value is consistent with the calculations of the diffusion Seebeck coefficient at 4.2 K from a simple model of detailed balance across a p-n interface under the assumption that the carrier distribution on each side of the interface is represented by a Fermi function at a different temperature [Esak 58].

3.9 TAMT

Up to now, the measured thermovoltage over the junction is found to depend on the temperature difference and it is in the μV range. The junction contains material for which the density of states and the magnetic anisotropies are connected via a strong spin-orbit coupling and therefore are magnetic field dependent. Thermal voltage itself is as well related to the density of states of the materials in the junction and consequently magnetization dependence is expected. Since the (Ga,Mn)As DOS is the only magnetic field dependent term in Eq. 3.10, thermopower measurements should reflect its response to a magnetic field. More specifically, the product of $D_{(Ga,Mn)As}(E)$ with a Fermi function

leads to a response which is proportional to the energy derivative of the DOS of (Ga,Mn)As at the Fermi level. This implies that the observed signal should reflect the properties of the magnetic anisotropy of the (Ga,Mn)As DOS.

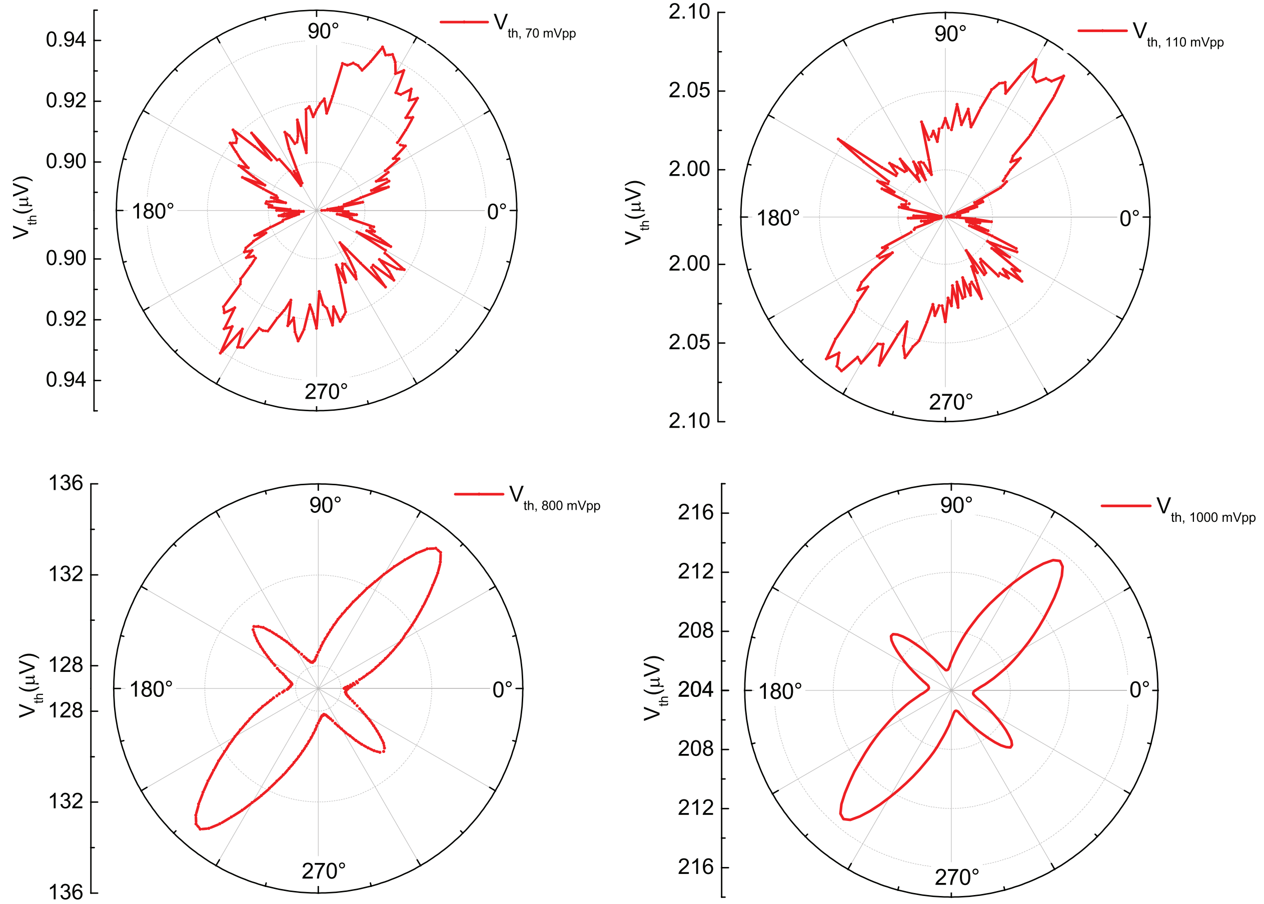

Figure 3.13: Thermovoltage in a magnetic field of 300 mT as a function of the field angle for different heating voltages. 0° is along [010] crystal direction.

In this part, some measurements on the volatile thermal voltage response of the system to a temperature gradient are present. Volatile here means in terms of magnetic field. A magnetic field high enough to saturate the ferromagnetic (Ga,Mn)As layer in a certain direction is applied. 300 mT are rotated in the sample plane, consequently perpendicular to the temperature gradient. That aims to study the magnetic anisotropies of the thermopower. In Fig. 3.13 a group of curves, so called saturation φ-scans, for different heating voltages are shown. A different heating voltage corresponds to a different temperature gradient and different thermal voltage. The latter increases when the temperature difference is increased, confirmed as well by the present φ-scans. A higher temperature gradient leads to a higher thermal voltage. The magnetic field angle is given with respect to the [010] crystal direction as denoted in Fig. 3.4. With increasing the heating voltage,

a fine structure is revealed. Four equivalent minima close to the [100] and [010] crystal axes and two sets of local maxima: a larger along [110] and a smaller one along [$\bar{1}$10] are observed. This symmetry is strongly reminiscent of (Ga,Mn)As TAMR measurements which map the symmetry of the (Ga,Mn)As DOS [Goul 04]. It is consistent with the thermovoltage mapping the energy derivative of the (Ga,Mn)As DOS as it depends on magnetization direction. We dub this spin caloritronic phenomena tunnelling anisotropic magnetothermopower (TAMT). The TAMT amplitude at 4.2 K and 300 mT is $\sim$ 5%.

A similar measurement is done applying the magnetic field out-of-plane, parallel to the layer plane. The thermal voltage is measured when the magnetic field is swept from -300 mT to 300 mT and 500 mVpp heating voltage is applied on the n-doped GaAs. The results are presented in Fig.3.14. The plot supports the observed in-plane magnetization dependence of the thermopower. That means that when the magnetization is aligned along magnetic hard axis, the thermal voltage gains a high value. Once the magnetization is saturated the thermal voltage saturates as well. When the external magnetic field is lowered the magnetization relaxes on an easy axis and so a lower thermal voltage is measured.

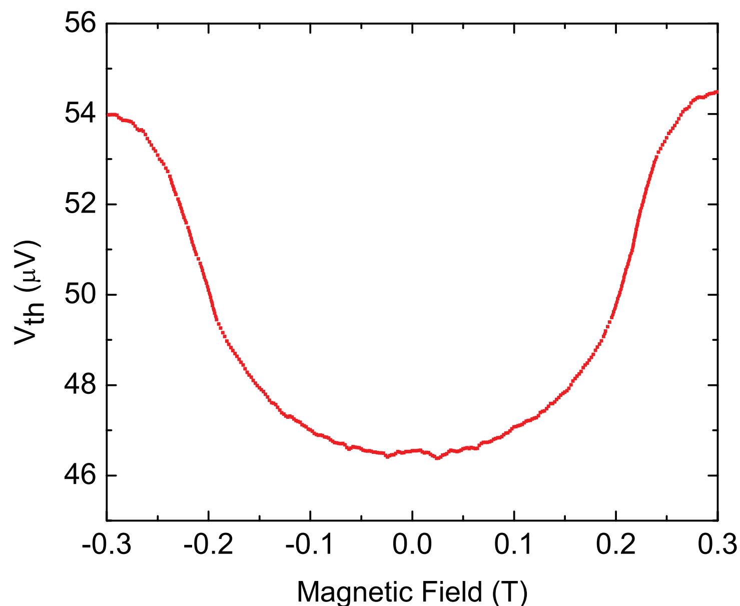

Figure 3.14: Thermovoltage as a function of an out-of-plane magnetic field sweep. To crate a temperature difference, a 500 mVpp heating voltage is applied.

In addition, a tunnelling anisotropic magnetoresistance (TAMR) measurement is done in a three terminal configuration on a junction. Current is sent between contacts "1" and "5". The voltage is detected between "5" and "3" (See Fig. 3.4). This three terminal non-local configuration is usually used to study the tunnelling properties in case where the tunnel barrier dominates. That eliminates the longitudinal resistance effects. In our device the tunnel and the longitudinal resistance are comparable and the result of the measurements are presented in Fig. 3.15a.

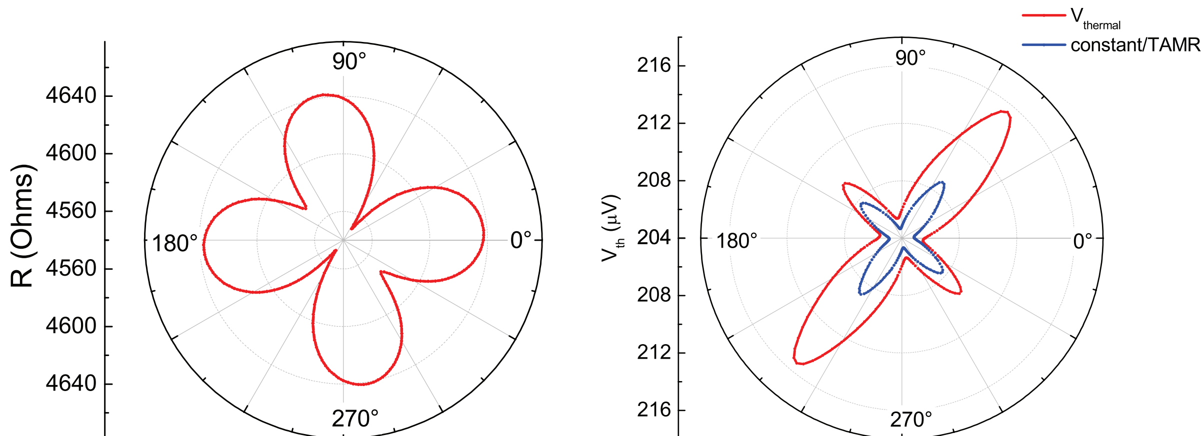

Figure 3.15: (a) TAMR measurement on the tunnel junction. Magnetic field of 300 mT is swept in-plane. (b) TAMT and inverse TAMR plotted for an in-plane swept B-field.

The resistance in this measurement is calculated dividing voltage by current for different magnetization configurations. The resistance is obviously dependent on the magnetization of the (Ga,Mn)As layer. A fourfold cloverleaf shape of the magnetization angular dependence is observed. The difference between the 0° and 90° is very small and it is difficult to distinguish between two magnetization directions. Otherwise, the difference between two minima along 45° and 135° is visible. The TAMR depends on the (Ga,Mn)As density of states (DOS), while the TAMT is a function of the derivative of the DOS in (Ga,Mn)As. Both effects are sensitive to the (Ga,Mn)As density of states which is dependent on the external magnetic field. In general TAMR and TAMT are complex effects since they both depends on the density of states of the two electrodes and the tunnelling coefficient, which describes the barrier. Calculations show that the size and the sign of the TAMR effect are very sensitive to the sample parameters [Goul 04] such as anisotropy of the (Ga,Mn)As density of states. In this sense, both effects can be seen as a tool for sensing the density of states of (Ga,Mn)As. The difference between them is the symmetry, meaning when a maximum is obtained for one direction in the TAMR measurement, a minimum is observed in the TAMT φ-scan. For comparison in Fig. 3.15 b the TAMT and the multiplicative inverse of the TAMR are plotted together. For the two effects the difference between the 0° and 90° direction is very small while the one for 45° and 135° is more obvious. In the TAMT scan the latter is even more pronounced, compared to the same in the TAMR scan.

Another issue is the difference between AMR (anisotropic magnetoresistance) and TAMT. Because TAMT maps the derivative of the (Ga,Mn)As DOS, the symmetry of the diffusion thermopower term in Fig. 3.13 is very distinct from the AMR-like symmetry ([McGu 75, Baxt 02]) observed in Ref. ([Pu 06]) for the phonon-drag dominated Seebeck coefficient. AMR has a $\cos^2\theta$ dependence on the angle θ between current and magnetization. Therefore, a two-fold symmetry is observed with a minimum in resistance when

the magnetization points along the current direction and a maximum for magnetization perpendicular to current. In our sample, the current in the GaAs heating channel is along the 90° direction, while the tunnel interface between GaAs and (Ga,Mn)As is not on the current path. The location of minima and maxima in Fig. 3.13 is crystal direction dependent and has no relation to the current direction, as confirmed on an identical structure with the heating channel oriented along [010]. The latter is present in Fig. 3.16. The heating channel is rotated 90° compared to the one from Fig. 3.4. The fourfold φ-scan for the heating channel along [010] is identical to the one with channel along [100].

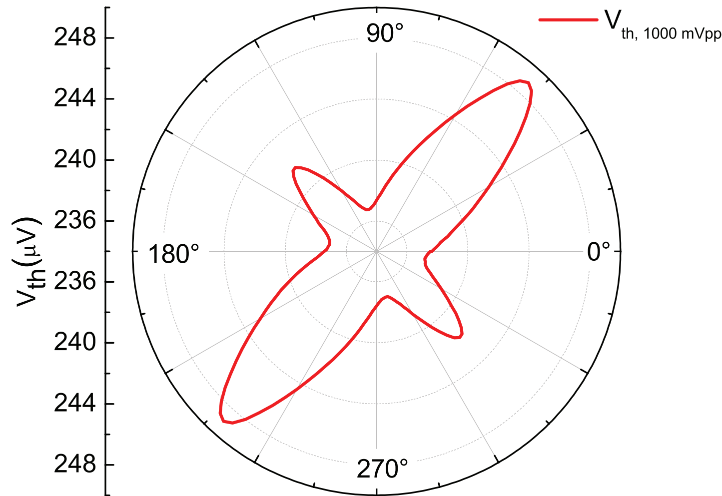

Figure 3.16: TAMT for a device, where the current is along [010] or 90° rotated with respect to the initially presented device.

In summary, the thermal voltage depends on applying an external magnetic field. Furthermore, the thermovoltage response upon magnetic field sweep is studied. That enhance the knowledge on the anisotropies of the thermopower in a system with a ferromagnetic layer and anisotropic DOS.

3.10 Anisotropies of TAMT

In this section an extensive investigation of the magnetic anisotropy of the thermal voltage is presented.

The thermopower is recorded during high resolution magnetic field scans from -300 mT to +300 mT along many in-plane directions. Applying 500 mVpp ac-voltage on the heating channel at a frequency of 13 Hz results in about 12 K temperature of the electrons in the GaAs heating channel. Bath temperature is at 4.2 K.

The magnetic field scans of the thermal voltage for some of the angles are presented in Fig. 3.17. The recorded thermal voltage changes with respect to the magnetization direction in the (Ga,Mn)As layer. That can again be explained by considering the (Ga,Mn)As magnetic anisotropy. When the magnetic field is swept from -300 mT to 300 mT, the

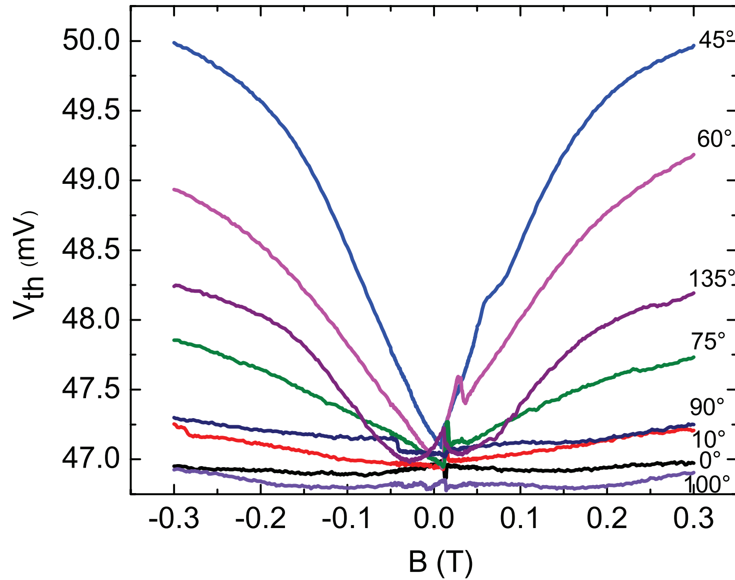

Figure 3.17: Thermovoltage as a function of magnetic field swept along various in-plane directions.

magnetization rotates towards an easy axis as the field approaches 0 mT, here towards 0° and 90°. It reverses at small positive fields in a mostly two-jump switching event. As the magnetization rotates, the thermal voltage changes smoothly. The largest magnetization rotation angle and thus the largest change in thermal voltage is observed when the magnetic field is swept along the 45° hard axes of the (Ga,Mn)As material ([110]). When sweeping the field along or close to a magnetic easy axis (0° or 90°), the magnetization stays along this easy axis direction, thus the thermal voltage is almost constant throughout the sweep apart from the one- or two-jump switching event. Figure 3.17 shows two distinct components of TAMT: a volatile contribution caused by the field holding the magnetization away from its easy axes at high fields and a non-volatile contribution associated with the difference in density of states when the magnetization switches between the two easy axis.

Furthermore, the non-volatile component of the TAMT for angles between 0° to 45° is shown in Fig. 3.18. These are the same scans from Fig. 3.17, presented in a smaller magnetic field range from 0 mT to 50 mT. In this range one- or two-jump events are observed. That corresponds to a switching of the magnetization in the (Ga,Mn)As layer.

As it was mentioned before, the thermal voltage is a function of the derivative of the density of states of the ferromagnetic (Ga,Mn)As. These DOS are magnetization direction dependent and thus making the thermal voltage also magnetization direction dependent. As an example, the 30°-curve is considered. Prior to the scan -300 mT are applied and subsequently the magnetic field is reduced to 0 mT and increased to small positive fields. For these fields, the thermal voltage undergoes small changes. They are due to the fact that the external magnetic field is not any more strong to keep the magnetization so

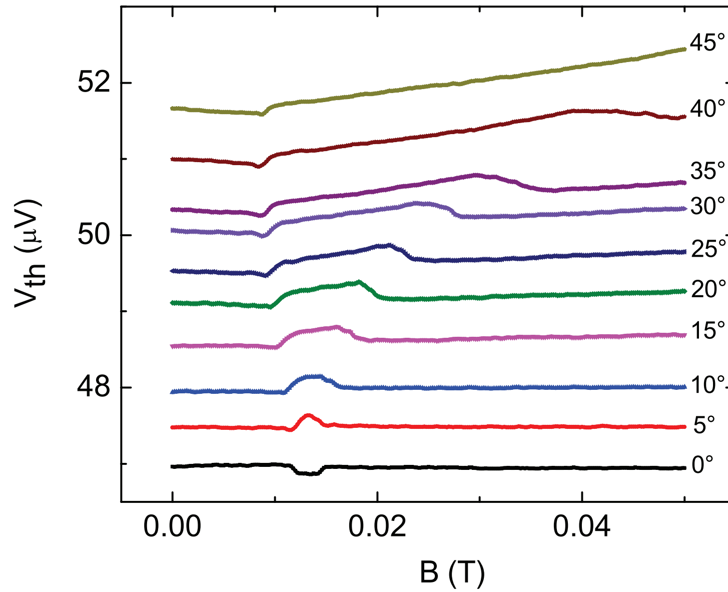

Figure 3.18: Thermovoltage scans for small in-plane B fields at different angles. An offset is introduced for clarity.

it relaxes to the closest energy favourable magnetic easy axis. In this magnetization direction the derivative of the DOS in the (Ga,Mn)As differs from the initial saturated state, resulting in a different thermal voltage response. At a certain positive magnetic field strength an abrupt jump is observed in the voltage signal. The jump happens when the magnetization switches between two easy axis in the biaxial (Ga,Mn)As. Before and after this first jump the thermal voltage attains two different values although the magnetization switches between two assumed to be equivalent states. This difference is actually a sign that the two magnetization states are not identical. There is a small uni-axial term which brakes the symmetry between the two easy axes. When continuing increasing the magnetic field, a second jump is observed in the 30° curve where the magnetization jumps from an easy axis into the external magnetic field direction. The thermal voltage in the last state is distinct from the one before the second and the first switching event. The DOS are anisotropic with respect to the different magnetization directions, which results in different thermal voltages. Equivalent magnetization direction give the same value of the thermopower. That can be seen in the 10° curve, where the measured thermal voltage before the first switching is almost the same as the one measured after the second switching.

The switching events in the recorded thermal voltage resemble a spin valve like signal. That is often reported in non-local measurements described in the previous chapter. As an example, Fig. 3.19 displays the 190° curve (field scanned from left to right) together with the 10° curve (field scanned from right to left) in spin-valve fashion showing a similar spin-valve signal to the one reported in Ref. [Cior 09].

For further analysis, the first and second switching fields of the magnetization reversal,

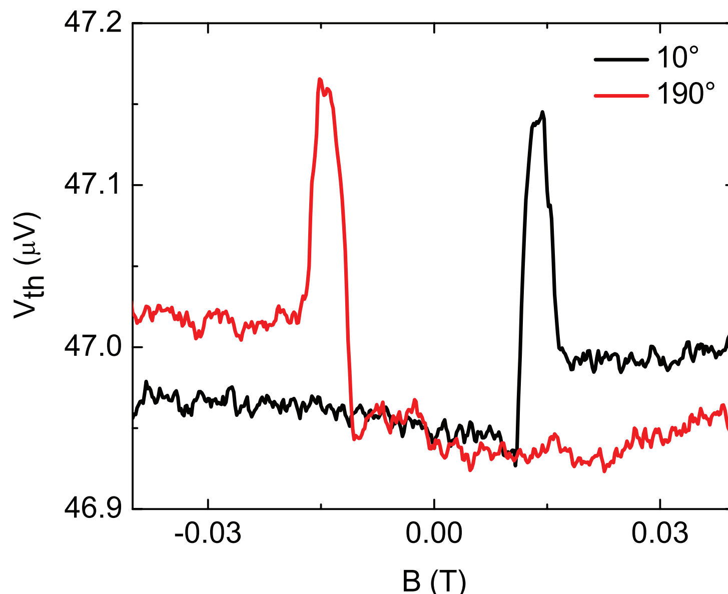

Figure 3.19: Enlargement of the low field part for 10° data and 190° scans. The 190° curve is offset by 0.15 μV to correct for a small thermal drift.

H_{c1} and H_{c2} respectively, are extracted from the above presented high resolution scans and plotted radially as a function of the field orientation φ in Fig. 3.20. The plot reveals the (Ga,Mn)As anisotropy components, just as in previous crystalline AMR [Papp 07b] and TAMR [Goul 04] measurements. The global easy axes correspond to the diagonals of the rectangular pattern of the first switching fields H_{c1}. As typical for (Ga,Mn)As [Goul 08], two small uniaxial anisotropy components along the [110] (elongation of the central square) and along the [100] (step features in the central shape) crystal direction are visible in addition to the main biaxial anisotropy.

To further support the statement that the anisotropies of the thermopower can be explained with the anisotropies of the (Ga,Mn)As layer, the data from the polar plot in Fig. 3.20 are fitted using the magnetic switching theory. The latter employed to describe the magnetization reversal of epitaxial magnetic metallic thin films [Cowb 95]. This theory has already shown a good agreement with previous TAMR results, where the material fits well to the theoretical assumption of a signal domain. This simplified model does not take into account the angle dependence of the domain nucleation energy, but for our idea to describe the anisotropies of thermopower, this issue is not of significant relevance. In Fig. 3.21 the experimental data are presented in blue and the fit is in red colour.

The fit is done using the following analytical expressions for the coercive fields associated with the double switching events presented:

$$H_{c1} = \frac{\varepsilon_{90^\circ} + \nu_1 K_u}{M(|\cos(\phi)| + |\sin(\phi)|)} \qquad H_{c2} = \frac{\varepsilon_{90^\circ} + \nu_2 K_u}{M||\cos(\phi)| - |\sin(\phi)||} \tag{3.2}$$

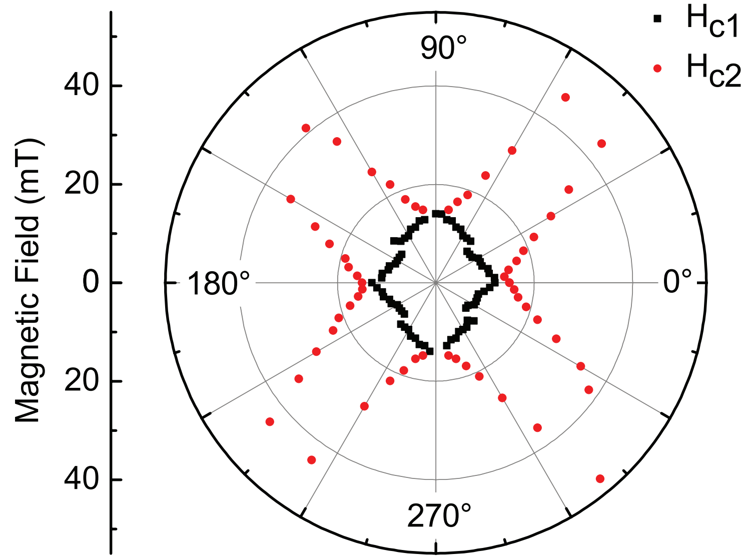

Figure 3.20: Polar plot of the magnetic field positions of the switching events H_{c1} and H_{c2} in the thermopower signal.

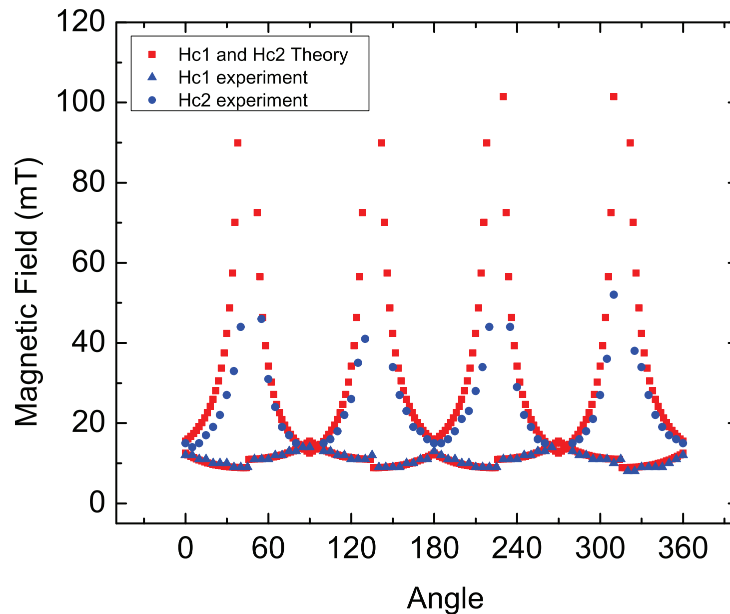

Figure 3.21: H_{c1} and H_{c2} vs angle dependence. Blue points are extracted from the experiment, red is the fit using relations 3.4.

The adjustable parameters here are the domain wall pinning energy ε_{90°/M and the strength of the uniaxial anisotropy $K_{uni[010]}/M$, both normalized to the sample magnetization. ν_1 and ν_2 are sign factors of ±1. The dependence of the sign on the angle ϕ is given in Table 3.1. From the diagonals of the inner square which corresponds to the measurements for H_{c1} in Fig. 3.20, the first parameter is estimated to be $\approx$ 14 mT. The second is estimated from the discontinuities of the same square at around 45° and 135° direction

to be in the order of 1.5 mT. In addition, the uniaxial component along [110] hard axis is estimated to be $K_{uni[110]}/K_{cryst} = 4\%$. The fit in Fig. 3.21 is done using the values of the adjustable parameters as determined from above. Despite the fact that the theory of the fit is done for magnetic metallic thin films, which have different electronic properties than the ferromagnetic semiconductor (Ga,Mn)As, the fit itself is in a good agreement with the extracted values for H_{c1} and H_{c2} from the thermopower measurements. Moreover, the values of the extracted anisotropy component of the (Ga,Mn)As are in the range of typically reported ones. As was discussed before in the previous chapter, this parameters are not a unique characteristic of the (Ga,Mn)As layers grown in Würzburg but rather they are a general property of the material.

ϕ/deg	ν_1	ν_2
0-45	-1	1
45-135	1	-1
135-225	-1	1
225-315	1	-1
315-360	-1	1

Table 3.1: Proper signs for ν_1, ν_2 as a function of magnetic field angle ϕ, to be used in conjunction with formula 3.4

Several times it is mentioned that, when a heating current technique is applied the electron temperature in the heating channel is changed. The device and particularly the (Ga,Mn)As stay at about 4.2 K, since the sample is diluted in liquid Helium. This is not directly measured but rather a comparison study is provided to support this statement. Here the thermal voltages from the positive field half of the high resolution magnetic field scans are collected and a compilation for all angles produces a fingerprint similar to the anisotropy fingerprint resistance polar plot (RPP). Such a fingerprint is given here for a heating voltage of 500 mVpp. Along with it RPP for three different lattice temperatures are present. The latter are measurements from earlier studies on the temperature dependence of the (Ga,Mn)As anisotropies and are measured on Hall bars in an AMR-geometry. A measurement for 1000 mVpp applied heating voltage has the same square pattern with the two uniaxial component presented and therefore is not shown here. The mainly biaxial anisotropy with nearly four-fold symmetry is revealed in the low temperature fingerprint. The uniaxial anisotropy term with an easy axis along the $[\bar{1}10]$ crystal direction dominates for measurements at higher temperature [Papp 07a]. The AMR amplitude and the switching events, meaning the size of the inner pattern of the fingerprint, decrease significantly with temperature (note the different magnetic field scales). In the case of the thermal voltage fingerprint the square pattern remains with no significant changes when the heating voltage is increased to 1000 mVpp. This means that the temperature of the (Ga,Mn)As layer does not undergo significant changes and it is close to the temperature in the chamber of 4.2 K. If this was not the case, the thermal voltage fingerprint

should develop in the way shown for AMR fingerprint. It is known that the biaxial and the uniaxial anisotropies exhibit different temperature dependence. That is due to their power-law dependence on the volume magnetization M. For the uniaxial the law is $\sim M^2$ and for the biaxial anisotropy term $\sim M^4$. As a result, the biaxial anisotropy component dominates the magnetic behaviour at 4.2 K and decreases faster in comparison with the uniaxial term when increasing the temperature. This leads to a transitions from a biaxial to uniaxial magnetic anisotropy when temperature is increased from 4.2 K to T_C. In the thermovoltage fingerprint there is no obvious transform of the magnetic anisotropy as it would be expected if the (Ga,Mn)As temperature differs considerably from 4.2 K. Therefore, the assumption of a (Ga,Mn)As layer at 4.2 K appears to be appropriate. That is taken into account in the simple model will be introduced to describe the observed temperature dependence of the thermopower.

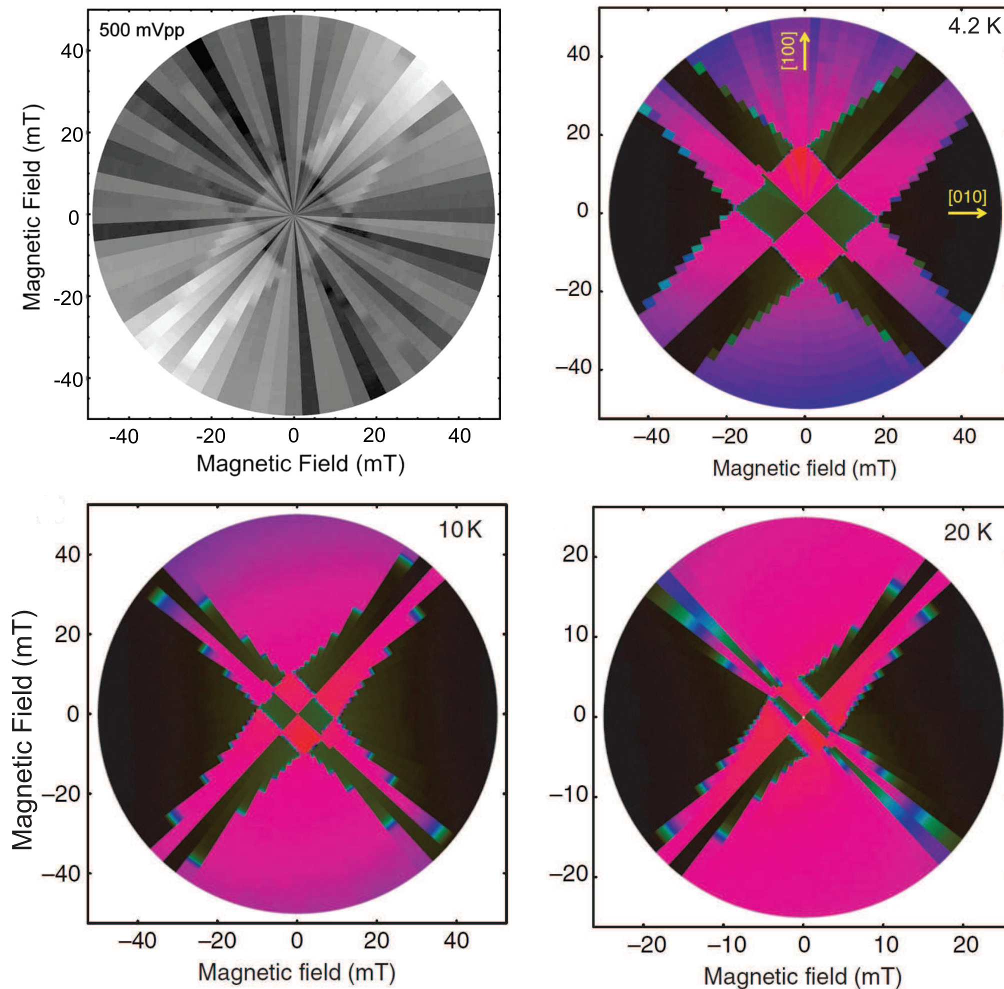

Figure 3.22: Fingerprints measured using different effects: the plot in grey scale is a result from a thermovoltage measurements. The coloured fingerprints are RPP and are reprinted form Ref. [Papp 07a].

3.11 Cartoon Model of TAMT

In this section, a simple descriptive model is presented to sketch the developed thermal voltage across a p-n junction and its dependence on temperature. The modelling is done by Philipp Dürrenfeld. Only a qualitative comparison is made between the model and the measured thermal voltage temperature dependence. The estimated values of the Seebeck coefficient are also compared. Before getting to the model, few assumptions are made. As it was already discussed, the (Ga,Mn)As temperature is kept constant during the experiment meaning at about 4.2 K. The temperature of the heating channel is varied applying different heating voltages. Both of the materials in the junction are thus at different temperatures and the temperature difference more or less drops over the 1 nm low temperature grown GaAs tunnel barrier. The carrier distribution on each side of the p-n interface is represented by a Fermi function for a free-electron type conductor at different temperatures [Esak 58]. For a simplification the barrier height at the interface is assumed to be large compare to the transport energy scales. The tunnel probability is energy independent and it is modelled by a delta function. A simplified energy diagram assuming a parabolic band model is depicted in Fig. 3.23.

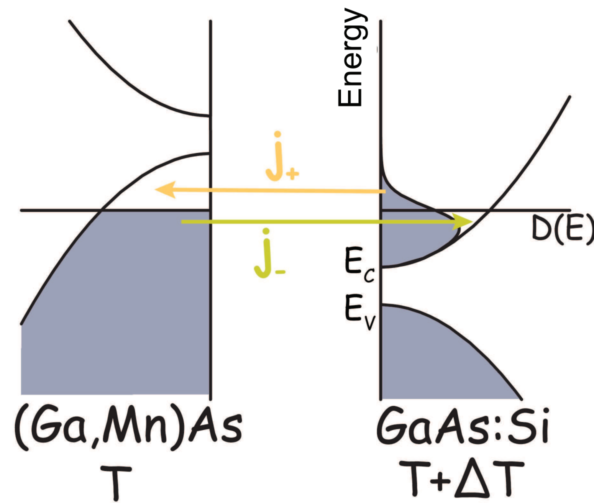

Figure 3.23: A simplified sketch of the p - n junction energy diagram. Arrows correspond to the currents which are present before a dynamic equilibrium is established.

The density of states on both sides of the interface for the valence and the conduction band near the band edge are given with the following expressions with respect to energy:

$$D(E) = \frac{1}{2\pi^2}\left(\frac{2m_e^*}{\hbar^2}\right)^{\frac{3}{2}}\sqrt{E - E_C} \quad \text{for the conduction band and} \tag{3.3}$$

$$D(E) = \frac{1}{2\pi^2}\left(\frac{2m_h^*}{\hbar^2}\right)^{\frac{3}{2}}\sqrt{E_V - E} \quad \text{for valence band.} \tag{3.4}$$

Here, the E_C and E_V are the bottom of the conduction band and the top of the valence-band, accordingly. The m_e^* and m_h^* stay for the effective electron and hole masses in the conduction and valence band, respectively. The Si-doped GaAs heating channel is highly doped. The total number of electrons (occupied conduction-band levels) is given by the total number of states $D(E)$ multiplied by the occupancy $f(E)$, integrated over the conduction band,

$$n = \int_{E_C}^{\infty} D(E) f(E)\, dE = \frac{1}{2\pi^2} \left(\frac{2m_e^*}{\hbar^2} \right)^{\frac{3}{2}} \int_{E_C}^{E_F} \sqrt{E - E_C}\, dE. \tag{3.5}$$

The occupancy $f(E)$ is a strong function of temperature and energy and it is represented by the Fermi-Dirac distribution function. The latter is assumed to be a step-function which value is 1 for energies below the Fermi level E_F and 0 above this level. That is use to be a valid representation for 0 K temperature. Thus, the integration takes place from the bottom of the conduction band to the Fermi level. The energy difference between these two then can be written as follows:

$$\Rightarrow E_F - E_C = \frac{(3\pi^2 \hbar^3 n)^{\frac{2}{3}}}{2m_e^*}. \tag{3.6}$$

This difference is calculated for the n-dope GaAs site taking the effective mass for electrons in the conduction band to be $m_e^* = 0.063 \times m_e$ [Sze 81]. The carrier concentration is extracted from the Hall measurements and it is $n = 4.0 \times 10^{18}\ cm^{-3}$. The estimated value for the difference is $E_F - E_{C,GaAs:Si} \approx 146$ meV, meaning that the Fermi level resides 146 meV above the bottom of the conduction band.

The same approach is made for the (Ga,Mn)As side of the junction. As a p-type highly doped metal-like semiconductor, the electronic correlations are usually less strong than in the case of very weak doping. Therefore, a single-particle picture often suffices [Jung 07]. The Fermi level position in the (Ga,Mn)As valence band is then estimated using similar equations like Eq. 3.5 and Eq. 3.6 adjusted for a disordered-valence-band regime:

$$E_V - E_F = \frac{(3\pi^2 \hbar^3 p)^{\frac{2}{3}}}{2m_h^*} \tag{3.7}$$

An average hole mass of $m_h^* = 0.50 \times m_e$ for the (Ga,Mn)As is used. Assuming carrier concentration of $p = 1.0 \times 10^{20}\ cm^{-3}$, $E_{V,(Ga,Mn)As} - E_F$ to be ≈ 157 meV. Consequently from this simple approach, a Fermi level is found to lie inside the (Ga,Mn)As valence band. That is in agreement with previously mentioned experimental works [Jung 07, Sliw 11]. This result is used for the rough calculation of the thermal voltage which appears on a junction once a temperature gradient is presented.

At the beginning, for simplicity the temperature of the GaAs:Si and the (Ga,Mn)As layers is assumed to be 0 K. In the real case of course, this is not true and the occupancy differs from a step function. When a temperature difference arises in a junction, the Fermi distribution function on both sides changes in a way that at the higher temperature end the tail of the distribution spreads to higher energies than at the other end of the junction [Barn 72]. Electrons are expected to move from the hotter to the cooler side and in this case currents are flowing from the Si:GaAs to the (Ga,Mn)As side. The current can be described with the following expression [Esak 58]:

$$\mathbf{j}_{+} = A \int_{-\infty}^{\infty} \Theta(E) \cdot D_{GaAs:Si}(E) \cdot f_{GaAs:Si}(E) \cdot D_{(Ga,Mn)As}(E - eV_{th}) \cdot (1 - f_{(Ga,Mn)As}(E - eV_{th}))\, dE \; . \tag{3.8}$$

The current is proportional to the number of empty states on the right side in Fig. 3.23, as well to the occupied states on the left side. $\Theta(E)$ is the tunnelling probability which is assumed to be $\Theta(E) = 1$. $D(E)$ and the $f(E)$ are the density of states and Fermi distribution function respectively. A similar equation can be written for the current flowing from (Ga,Mn)As to the Si:GaAs side.

$$\mathbf{j}_{-} = A \int_{-\infty}^{\infty} \Theta(E) \cdot D_{GaAs:Si}(E) \cdot (1 - f_{GaAs:Si}(E)) \cdot D_{(Ga,Mn)As}(E - eV_{th}) \cdot f_{(Ga,Mn)As}(E - eV_{th})\, dE \; . \tag{3.9}$$

The total current through the interface then is a sum of the above written $\mathbf{j}_{-}$ and $\mathbf{j}_{+}$:

$$\mathbf{j_{total}} = A \int_{E_{C,GaAs:Si}}^{E_{V,(Ga,Mn)As} - eV_{th}} D_{GaAs:Si}(E) \cdot D_{(Ga,Mn)As}(E - eV_{th}) \cdot (f_{GaAs:Si}(E) - f_{(Ga,Mn)As}(E - eV_{th}))\, dE \; . \tag{3.10}$$

When a dynamic equilibrium is established, the total net current should be zero and a numerical solution of the above equation gives an approximate value for the built-up electrostatic potential V_{th}. The numerical solutions of the integral 3.10 for different temperature difference is shown in Fig. 3.24.

Here, the variable parameter is the Si:GaAs temperature, while the (Ga,Mn)As temperature is kept 4.2 K. The numerical calculation is done with Mathematica code written by Philipp Dürrenfeld. The carrier density for the (Ga,Mn)As is taken to be $N_a = 1 \times 10^{21}\ cm^{-3}$. The thermal voltage follows a quadratic power dependence with respect to temperature difference and is qualitatively similar to the experimental results (Fig. 3.11 a). Quantitatively the model and the experimental results differ. More precise quantitative model would require a detailed treatment of the top four valence band levels, including their anisotropic effective mass.

Along with the thermal voltage, the thermopower vs. temperature difference dependence is presented in Fig. 3.11 b. The simple model, assuming only the band contribution

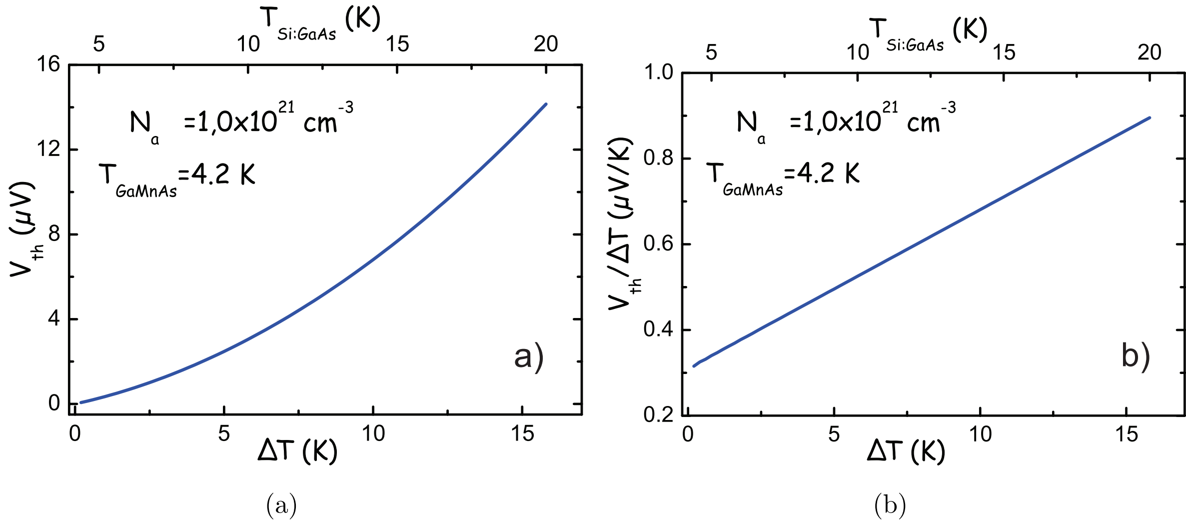

(a) (b)

Figure 3.24: Results from the calculations based on the cartoon model for a) thermovoltage vs. T, b) thermopower vs. T

to the thermal voltage, gives a linear dependence for the temperature range of interest which is expected in general for the diffusion Seebeck effect and is in qualitative agreement with Fig. 3.11b. When the temperature difference approaches zero, a Seebeck coefficient of 0.3 μV/K is estimated. This value is consistent with the experimentally obtained one of 0.5 μV/K. The slope of the line from Fig. 3.11b, however, is smaller than the experimentally observed one, but the model, as mentioned before, is too simplified to give an exact quantitative description of the measured effect. Nevertheless, this simplified model, implying a Fermi level deep in the (Ga,Mn)As valence band, is sufficient to capture the essence of the results.

In addition to the above present calculations, the Seebeck coefficient temperature dependence using the previously described model is depicted in Fig. 3.25. For the calculation, the temperature difference between the Si:GaAs channel and (Ga,Mn)As is set to be $\Delta T = 0.2$ K and the variable is the temperature of the Si-doped heating channel.

For the studied temperature range a linear relation is established between the S and T applying the simple model. This is in agreement with already mentioned Mott-Relation and the diffusion component of the thermopower.

In summary, the diffusion thermopower in a (Ga,Mn)As tunnel junction is measured. The behaviour of the measured thermovoltage is fully described by the magnetization direction in the (Ga,Mn)As layer, together with the thermal voltage dependence on the magnetization direction given in Fig. 3.13. Diffusion thermopower can be measured over a tunnel barrier between a magnetic (Ga,Mn)As layer at 4.2 K and a heated carrier system in a GaAs mesa. This diffusive component of the Seebeck coefficient is in accordance with theoretical estimates, and much smaller than the phonon-drag dominated Seebeck coefficient reported by Pu et al. [Pu 06]. Its magnetic field dependence is given by

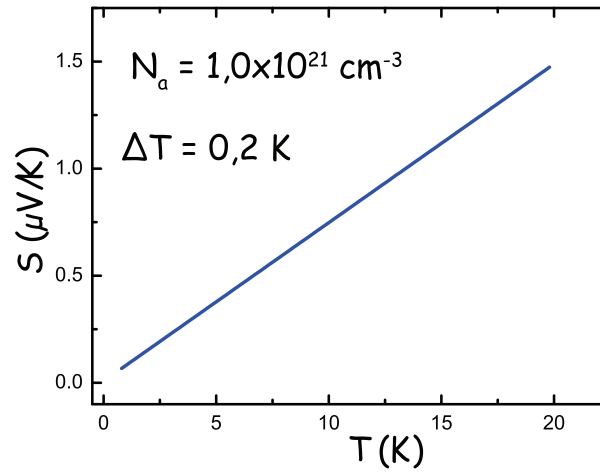

Figure 3.25: Seebeck coefficient vs. temperature dependence - simulated curve.

the derivative of the (Ga,Mn)As DOS and is also clearly different from the AMR-like symmetry observed in Ref. [Pu 06]. Moreover, this dependence of the thermopower on the derivative of the DOS could prove a useful tool in mapping out the details of the DOS, especially in samples near the metal-insulator transition.

Chapter 4

Anomalous Nernst Effect of (Ga,Mn)As/GaAs Tunnel Junction

This chapter deals with the next member from the family of thermoelectric / thermomagnetic effects. This is the Nernst effect of a (Ga,Mn)As/GaAs tunnel junction. We present a device geometry suitable for observation of the Nernst effect and then we measure the device at 4.2 K. At this temperature the (Ga,Mn)As layer is ferromagnetic and coupling of its magnetic properties to the thermomagnetic effect are studied and describes in the following sections.

4.1 Planar and Anomalous Nernst Effect in (Ga,Mn)As - State of Art

Spin caloritronics serves to establish a full and consistent physical picture of the anomalous transport mechanism in systems with strong spin-orbit coupling [Naga 10]. One of the pioneering works in the field of spin caloritronics is the observation of spin-Seebeck effect (SSE) [Uchi 08]. The SSE has been reported for metallic magnets [Uchi 08], magnetic insulators [Uchi 10b, Uchi 10a, Adac 10], Heusler compounds [Bosu 11], and also for the ferromagnetic semiconductor (Ga,Mn)As [Jawo 10, Jawo 11]. It is defined as the generation of a pure spin current when a temperature gradient is applied. The physics of this phenomenon remains complex and debatable. In some of the recent studies a phonon drag was assigned to govern the SSE [Adac 10, Jawo 11]. In addition to that, Huang *et al.* [Huan 11] demonstrated that the anomalous Nernst effect (ANE) might obscure the spin-dependent thermal transport([Uchi 08, Uchi 10b, Uchi 10a, Adac 10, Bosu 11, Jawo 10, Bakk 10]). The anomalous Nernst- Ettinghausen effect is a thermoelectric analogue of the anomalous Hall effect. It appears as a response in a ferromagnetic metal/semiconductor subjected to a temperature gradient [Slac 11]. The effect has been studied in ferromagnetic metals [Niel 34, Vasi 72, Miya 07], oxides [Sury 99, Miya 07], spinels [Lee 04, Miya 07, Hana 08] and diluted magnetic semiconductors [Pu 08]. It has

turned out that in ferromagnetic materials the ordinary Nernst coefficient is smaller in comparison with the anomalous Nernst coefficient [Niel 34].

The ANE can provide some useful information about the scattering and the electronic structure in materials. The effect might be used as a test of the existing theory on the anomalous Hall effect (AHE) [Naga 10]. Up to date, there are two significant works on the ANE in the ferromagnetic semiconductor (Ga,Mn)As [Pu 08, Jawo 10]. In both of these studies the ferromagnetic layer has an out-of-plane easy axis and the bulk properties are examined. Moreover, the present data in [Pu 08] are suspected to be influenced by a phonon drag effect. Thus, no study on the electron contribution to the anomalous Nernst effect in (Ga,Mn)As with an in-plane biaxial anisotropy has been reported. Therefore, in this chapter a device geometry for measuring the ANE in biaxial (Ga,Mn)As layers is proposed and measured. Before continuing to the experimental section, we briefly describe the preceding studies on Planar Nernst effect (PNE) and ANE in (Ga,Mn)As reported by Pu *et al.*[Pu 06, Pu 08]. These works are performed mostly below the Curie temperature of the ferromagnetic material, thus relevant to our experiment.

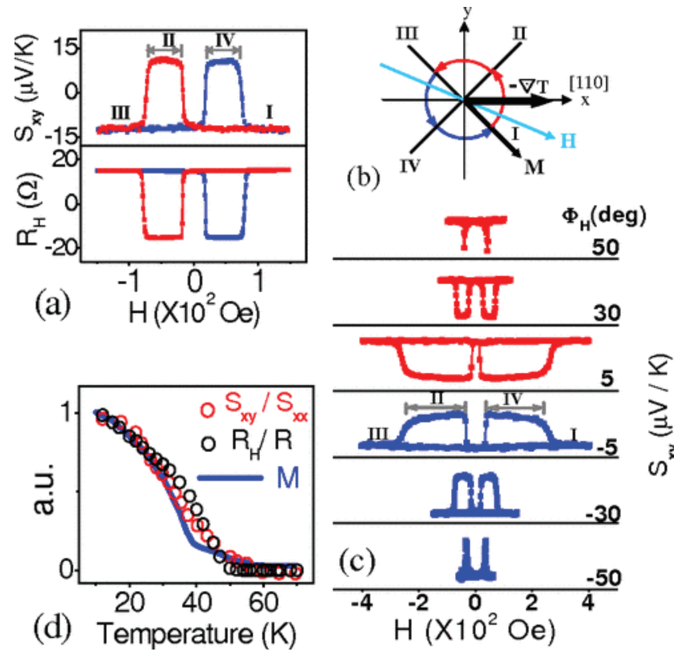

Figure 4.1: (a) Planar Nernst effect (PNE) and planar Hall effect at 6 K Φ_H =–30° for $Ga_{1-x}Mn_xAs$ (x = 0.039). Sketch of the relative orientation of $-\nabla T$, M and H. four direction marked as I, II, III, and IV are easy directions of the M. (c)Angular dependence of PNE. (d) Comparison of S_{xy}/S_{xx} and R_H/R, and sample magnetization M measured by SQUID. Figure reprinted from ref. [Pu 06].

The Planar Nernst Effect [Pu 06] in (Ga,Mn)As is first observed in a Hall bar geometry present in Fig. 3.1. A large transverse signal of about 15 μV/K is detected when applying a temperature gradient along [$\bar{1}$10]. The magnetization is along one of the easy axes, in this case close to [100] crystal direction. The measured signal is linear with the applied

temperature difference and changing in a nonmonotonic way when the magnetic field is swept in plane. The reported value for the measured transverse voltage drop is much greater than the conventional Nernst effect [Zeh 90, Xu 00]. As will be seen later in this chapter, the Nernst coefficient in the Pu et al. [Pu 06] studies is also greater than the one estimated for our device geometry.

In Fig. 4.1 different magnetic sweeps are shown. Two switching events are present in each sweep. They correspond to the switching fields in planar Hall measurements, also given in Fig. 4.1. These events are explained with the magnetization reversal. Their dependence on the angle between the temperature gradient and the magnetization is found to be consistent with the two anisotropy model discussed for the Hall effect in this material [Tang 03]. Subsequently, the jumps in PNE are normalized by the longitudinal thermopower and plotted as a function of the temperature. It is observed that the ratio decrease steadily with increasing temperature and approaches zero when the magnetization vanishes at T_C. In summary, the longitudinal and the transverse thermopower are found to be intimately related through the sample magnetization.

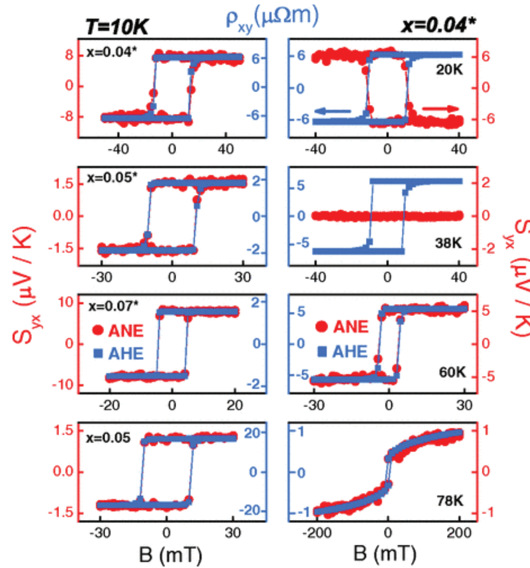

Figure 4.2: AHE and ANE loops at T = 10 K for different samples (left column) and at different temperatures for the 4 % annealed sample (right column). Figure reprinted from ref. [Pu 08].

The Planar Nernst effect, as described above, arises in a plane where both the temperature gradient and the magnetization are lying. The orientations of the vectors are different in comparison with the ordinary or the anomalous Nernst configuration. The condition for the last two effects to appear is that the M and ΔT vectors are perpendicular to each other. The resulting Nernst voltage is a cross product of the magnetization and temperature gradient.

For the observation of the anomalous Nernst effect in (Ga,Mn)As Pu *et. al* [Pu 08] proposed layers with out-of-plane easy axis. Some of the samples are annealed in air at

250° C for 60 min.. The annealed samples reveal dramatically increased T_C, decreased resistivity and slightly increased coercive field. Different layers are then patterned into Hall bars with long axis oriented along [110] crystal direction. In the Nernst experiment a temperature gradient is applied along [110]. When the magnetic field is swept, a transverse voltage response is recorded and shown as a function of the applied field in Fig. 4.2.

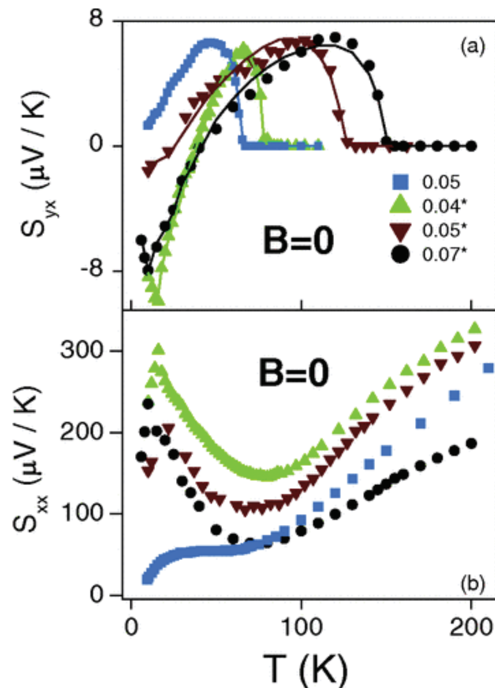

Figure 4.3: Temperature dependence of S_{yx} (a) and S_{xx} (b) for all samples measured at zero magnetic field. Figure reprinted from ref. [Pu 08].

The ANE and AHE loops are plotted in the same graph for each sample and temperature. For different Mn concentration and at temperature of 10 K the ANE and the AHE curves are found to "match exceedingly well (up to a scaling factor)". This suggest that both of the anomalous effects scale with the magnetization in the same fashion. However, a big difference between the ANE and the AHE is found when changing the temperature. Increasing the temperature to some intermediate T the ANE undergoes a sign change, whereas the AHE remains positive at all temperatures (the right column in Fig. 4.2). The change exists for all the annealed samples. No explanation of the observed change is given. The nearly perfect match is then again pointed as a sign of the common physical origin of the two effects.

Furthermore, both the longitudinal Seebeck and the transverse Nernst signal are recorded as a function of temperature in zero magnetic field. The curves for different samples are given in Fig. 4.3. A commentis made only for the Nernst response. Above the Curie temperature the anomalous Nernst signal disappears. This is consistent with the fact that the effect scales with the spontaneous magnetization. These zero field dependences are

then used to verify the Mott relation for AHE and ANE. The intrinsic origin for both of them is demonstrated.

The above described experiments comprise most of the important work done in the direction of anomalous Nernst effect in (Ga,Mn)As to date. Nevertheless, it has not been reported yet how would the ANE look like in the case of a biaxial (Ga,Mn)As. This is of particular interest since most of the (Ga,Mn)As based logic devices [Mark 11c] employ the fourfold anisotropy for its functionalities and operation. Therefore, in the present chapter we propose a device geometry for measuring the ANE in a biaxial (Ga,Mn)As. The device fabrication and characterization are discussed in the following section.

4.2 Nernst Geometry and Device Fabrication

As previously mentioned, when a thermal gradient is present in a ferromagnetic metal or semiconductor, one can observe the anomalous Nernst effect (ANE). It describes the occurrence of an electric field perpendicular to both the temperature gradient and the magnetization. So far, the ANE was observed in (Ga,Mn)As layers with an out-of-plane easy axis [Pu 08]. However, no study on layers with in-plane magnetic easy axis is reported up to date. In this chapter we present a device for measuring anomalous Nernst effect based on a (Ga,Mn)As tunnel junction with in-plane anisotropy. Here, the junction is used to reduce the phonon drag contribution to the magnetothermal effect.

For the device, a similar layer stack is used as the one for the thermopower measurements (see Chapter 3). The stack consists of 20 nm thick ferromagnetic semiconductor (Ga,Mn)As, 1 nm undoped GaAs and 80 nm highly doped Si:GaAs on top of 200 nm undoped GaAs (See Fig. 4.4). All are grown with a standard low temperature molecular beam epitaxy. Subsequently, 5nm Ti and 30 nm Au are deposited in UHV electron-gun evaporation chamber where the sample is transferred without breaking the vacuum. Because of the lattice mismatch to the GaAs buffer, the (Ga,Mn)As layer is compressively strained. Therefore, its magnetic easy axes lie in the plane perpendicular to the growth direction [Shen 97].

The design of the device for measuring the Nernst effect is present on Fig. 4.4. It is similar to the one used for the observation of the diffusion thermopower in (Ga,Mn)As [Nayd 11]. However, there are some differences between the two devices. The single top contact utilized to detect the TAMT effect is replaced with four small top contacts. The device is defined using electron beam lithography (EBL), multi-step optical lithography, Chemical-assisted Ion Beam etching (CAIBE) and wet etching. First, four small Ti/Au contacts are defined in a 50 x 50 μm^2 square by E-beam lithography and Ar-plasma etching. The residues of Ti are etched away with $HF:H_2O$ = 1:200 solution. This ensures a free of electrical shorts area between the small voltage probes on the (Ga,Mn)As top surface. Subsequently, a square under the small contacts is patterned with another E-Beam step. The material around it is etched up to the Si:GaAs with BCl_3- plasma and so thus the junction of interest is formed. Afterwards, a 600 μm long n-doped GaAs heating channel is defined along [100] (Ga,Mn)As magnetic easy axis by means of optical lithography followed by BCl_3- plasma etching. Additional bonding pads are established with optical lithography and lift-off process. Finally, four metallic air-bridges are fabricated using EBL [Borz 04]. They connect the voltage probes attached around the edges of the (Ga,Mn)As element to the big bonding pads. The design and the fabrication are developed by Kia Tavakoli.

The electrical characterization of the device is performed at 4.2 K in a 3D cryostat with a vector field magnet, capable of producing fields up to 300 mT in any spatial direction. A detailed analysis and results are given in the following sections of this chapter.

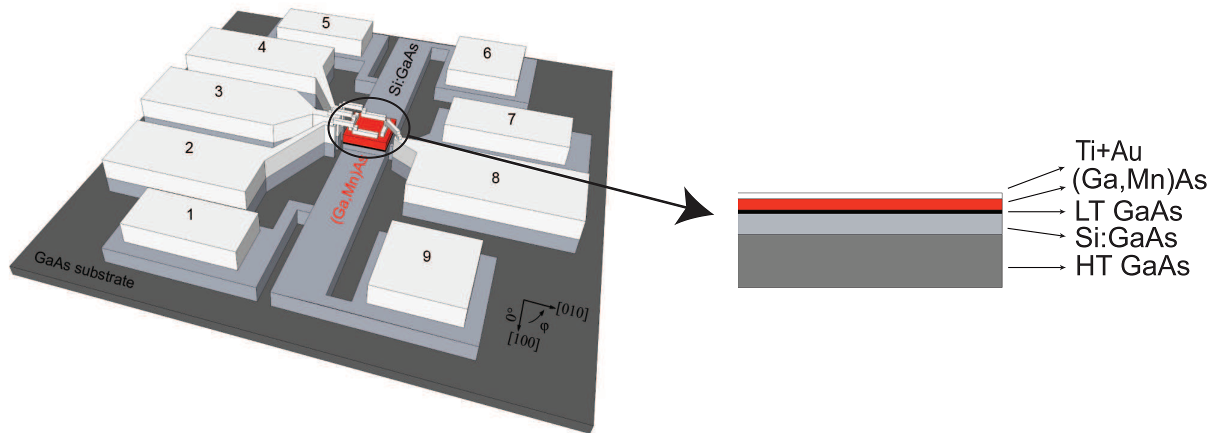

Figure 4.4: Schematic diagrams of the device geometry and the layer stack used in the study of the Nenrst effect. The temperature gradient is perpendicular to the plane defined by [100] and [010] crystal directions.

4.3 Weak Localization Measurements and Temperature Calibration

Before continuing with the detection of the Nernst effect, a temperature calibration is performed by means of the Weak Localization effect (WL). For that purpose, the experimental set-up in Fig. 4.5 is used. It is similar to the one from the thermopower experiment in Chapter 3. A 14 Hz AC-current is used to heat the electron population in a Si:GaAs heating channel (light grey colour), while the device, in particular the junction (in red), remains at 4.2 K. That results in a temperature gradient across the junction. The resistance response to an applied out-of-plane magnetic field is used as a reference for the temperature of the electrons in the heating channel. For the detection of the channel resistance, the voltage drops on the channel and on a 1 kOhm reference resistor connected in series are measured with model a 124 Lock-In amplifier. That is equipped with 116 Differential Preamplifier and for the WL measurements a band pass filter is used. The output signal of a function generator (FG), which heats the electrons in the channel, serves as a trigger for the lock-in amplifier. The lock-in amplifier, which is actually a voltmeter, is connected to the laboratory clean ground. The correct realization of the WL measurements requires a floated source. That guarantees a lack of multiple grounds on the sample and unknown current paths. The function generator is floated by an isolation tape attached to the grounding point of the instrument. In addition, a 1:1 transformer is utilized to separate the Lock-In / sample ground from the floated FG.

For the first experiment, different heating voltages are applied, while the sample stays at liquid Helium temperature. The magnetic field is swept out-of-plane. The resistance of the heating channel is calculated from the measured voltage drops on the channel and the reference resistor. Several normalized resistance curves (normalized to the resistance

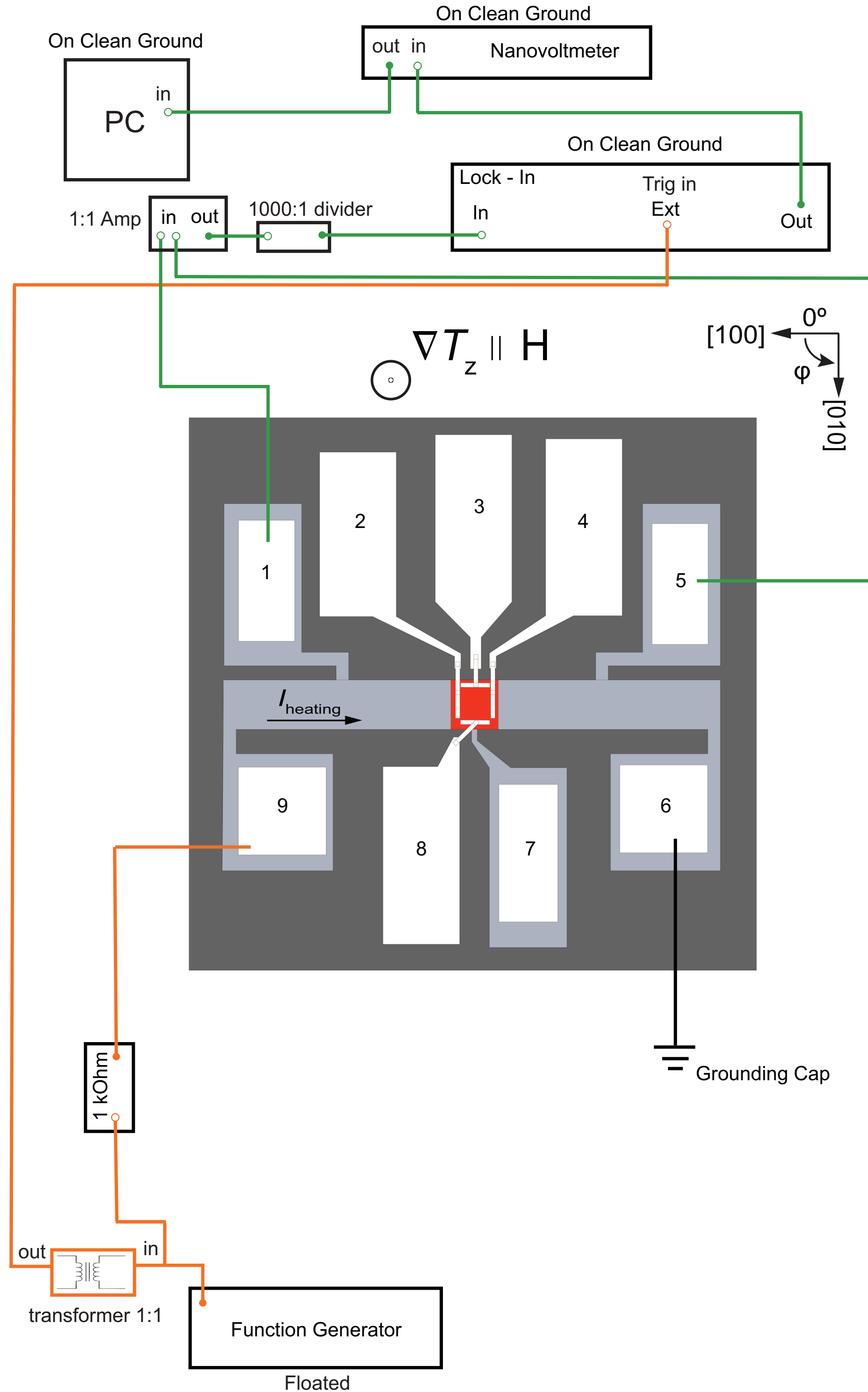

Figure 4.5: WL-measurement set-up. A function generator is used to apply a heating voltage between contacts "9" and "6". A Lock-In amplifier measures the voltage drop between contacts "1" and "5", and across the 1 kOhm reference resistor.

value at B = 0 T) with respect to the applied magnetic field are present in Fig. 4.6. For heating voltages below 1 Vpp the width of the WL feature remains approximately unchanged. This suggests that for these voltages the temperature of the electrons in the channel does not undergo significant changes with respect to the device temperature (4.2 K). As a result, no temperature difference is established across the junction and no Nernst signal is detected. That fact is used to choose an appropriate heating voltage for the WL experiment where the bath temperature is varied and the electrons are in equilibrium with the bath. From Fig. 4.6 it can be noticed that above 1 Vpp the width of the WL feature (peak) increases when increasing the heating voltage. For an empirical comparison, the width of the curve at an arbitrary hight of 99.83 % from the maximum resistance value at B = 0 T is used. The width serves to estimate the electron temperature once the resistance is calibrated for different bath temperatures.

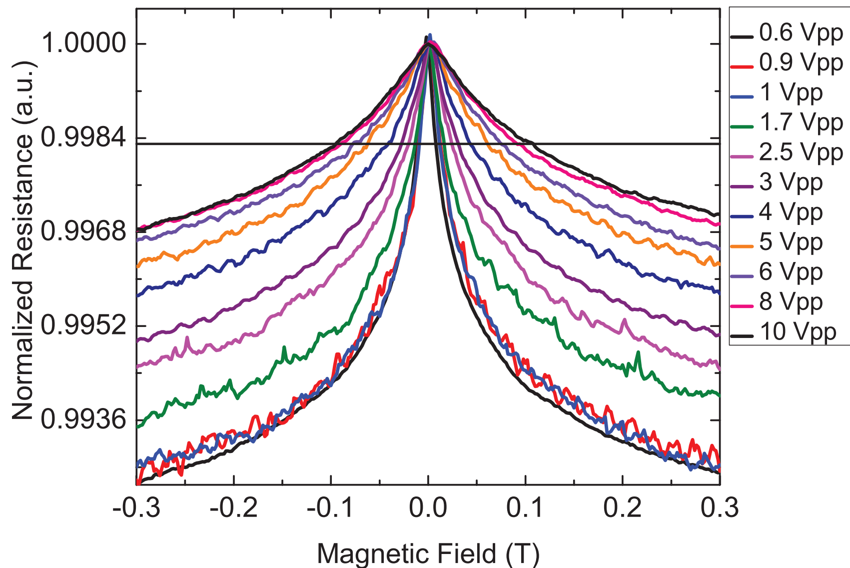

Figure 4.6: WL-measurements at 4.2 K for different heating voltages. It can be noticed that for the first three values of heating voltages the width of the WL-peak does not change significantly. This suggests that the temperature of the electrons in the GaAs heating channel remains relatively unchanged. That observation is used to measure the WL-effect for different bath temperatures. The small slope in the measured curves is due to temperature drift.

As a next step, the resistance of the channel for different bath temperatures is measured. 1 Vpp sine signal is applied on the channel and the magnetic field is swept out-of-plane. At this heating voltage the electrons in the channel have relatively the same as the bath temperature. Normalized resistance curves for different bath temperatures are shown in Fig. 4.7. The width of the curves at 99.83 % from the maximum resistance value (at B = 0 T) is extracted. The relation between the width and the bath temperature for different heating voltages is found to be described by a parabola (not shown). That relation is used to estimate the electron temperature for different heating voltages from Fig. 4.6. From there, the relation between temperature difference and heating power

can be found and is plotted in Fig. 4.8. It can be noticed from Fig. 4.8 that below cer-

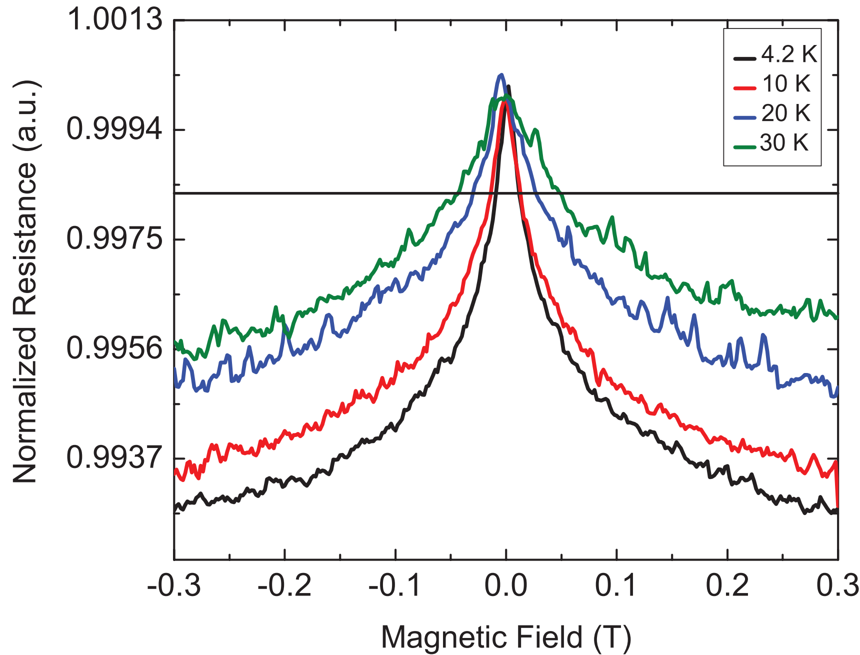

Figure 4.7: The channel resistance with respect to an out-of-plane magnetic field sweep. The measurements are performed for different bath temperatures and a heating voltage of about 1 Vpp.

tain heating power the temperature difference increases linearly with the applied power. Above that power, the linear dependence slope tends to decrease and the curve reaches a saturation. This might be attributed to a cooling effect. Its contribution increases with the temperature difference. A red curve in Fig. 4.8 is an empirical fit of the observed dependence of the temperature difference (ΔT) on the heating power. The curve is used later for the estimation of ΔT and also of the Nernst coefficient.

Furthermore, Fig. 4.9 presents a comparison between some curves at 30 K and at 4.2 K. At 1 Vpp heating voltage and 30 K bath temperature the electrons in the channel are in equilibrium with the bath. The 10 Vpp resistance curve at 30 K seems to overlap with the one for the same heating voltage but at 4.2 K. That suggests a temperature of the electrons in the heating channel of about 50 K for both temperatures. The noise and the small drift coupled with the measured WL curves are attributed to temperature fluctuations and instability.

It should be noticed, that it is difficult to do WL measurements at higher than 4.2 K temperatures in the 3D cryostat. This difficulty is due to the fact that for measurements at higher temperature, when the latter is stabilized with the accuracy of $\pm$0.01 K, the cryostat reaches an equilibrium state similar to a resonant column. In that state the temperature in the sample chamber oscillates and it can be detected in a resistance measurement. The temperature sensor does not see these oscillations because it is not directly mounted on the sample. To circumvent this difficulty, the WL measurement is

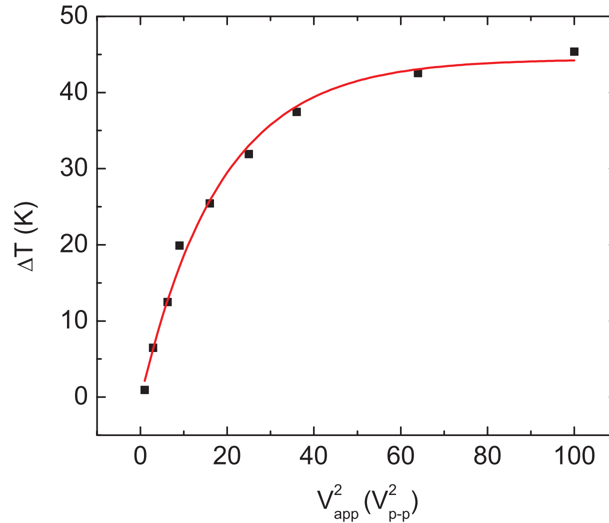

Figure 4.8: A relation between the temperature difference and the applied heating power. The red curve is an empirical fit to the observed dependence.

started once the temperature is stable with an accuracy of ±0.5 K. Then, no oscillations are present for this accuracy but small fluctuations or drift can be still present in the temperature and observed in the resistance curves. For the Nernst detection, however, the temperature is stabilized with accuracy of ±0.01 K.

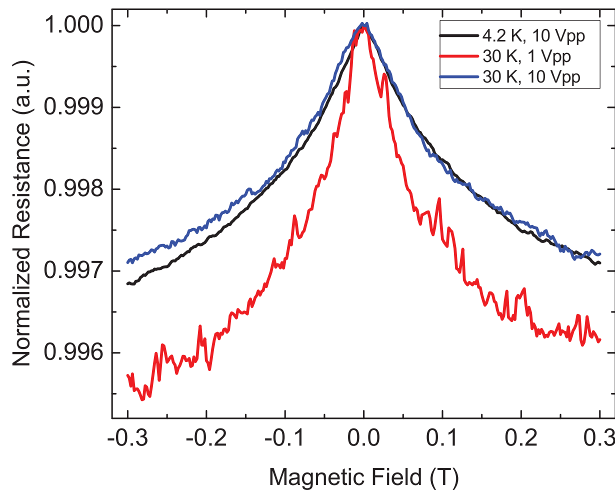

Figure 4.9: A comparison between the WL-curves for different bath temperatures. The 10 Vpp results in approximately identical WL-peak for 4.2 K and 30 K bath temperatures.

With this the temperature calibration is considered to be completed for the measured temperature range. Further, the detection of the Nernst effect of the studied junction is the described in the following sections.

4.4 Detection of the anomalous Nernst Effect of a (Ga,Mn)As/GaAs tunnel junction.

In this section the Nersnt effect of (Ga,Mn)As / GaAs tunnel junction is studied. The set-up for the experiment is shown in Fig. 4.10. An ac-voltage is applied between contacts "6" and "9". It is used to heat the electron gas in the Si:GaAs channel, while the 50 $\times$50 μm^2 (Ga,Mn)As contact (in red colour in Fig. 4.5) remains at 4.2 K (later verified by an experiment). That results in a temperature gradient (∇T) across the (Ga,Mn)As/GaAs junction. When a magnetic field H is applied perpendicular to ∇T, a voltage drop develops perpendicular to both H and ∇T. The latter arises perpendicular to the plane and H is applied along different in-plane directions. The voltage response is recorded on contact pairs "3" and "8" or "2" and "4". Because the contact pair "2" and "4" got damaged during measurements, only few measurements from this will be shown in the Appendix. They are not used for quantitative analysis but only to support the observations from contact pairs "3"-"8". The detection of the voltage drop between these contacts is performed with a lock-in amplifier set to measure the $2f$ component of the total signal. This suggest only thermal signal to be detected (see Chapter 3). The $2f$ detection is done with a Notch filter to cut the $1f$ contribution and triggering at $2f$. The function generator remains floated like in the WL experiment.

At the first place, an ac-voltage with a constant amplitude of 4 Vpp and with different frequencies is used. A magnetic field of 300 mT is rotated in-plane. The current areal density is about 9.2 A/m (11.5 A/cm^2) and that gives a temperature difference over the junction of 30 K (as determined from the WL measurements). The voltage scans for several frequencies are shown in Fig. 4.11. These frequencies are orders of magnitude smaller than the characteristic frequencies related to the electron thermalization or scattering times. Therefore, one would expect that the measured effect in this frequency range is not frequency dependent. That is obviously not the case for the curves shown in Fig. 4.11. The magnitude and the amplitude of the voltage change when increasing the frequency. Another issue is that the Nernst effect is asymmetric with the applied magnetic field. That means a voltage which amplitude is equal for two magnetic field directions which are 180° apart, but different in sign. This is also not observed in the measured signal shown in Fig. 4.11. A possible explanation for this is that the measured signal is a superposition of different effects which have different response to a magnetic field. Therefore, a symmetrization is performed on the raw signal.

The results from the symmetrization are shown in Fig. 4.12. The first graph on the left is the part of the signal which is asymmetric with the applied field direction. The graph next to it is the symmetric with the magnetic field component. As it can be seen, the asymmetric signal is not dependent on the frequency. It symmetry reminds to the Nernst effect. The symmetric part on the other hand changes magnitude and amplitude when the frequency is varied (for the measured frequency range).

In summary, the measured voltage drop between contacts "3" and "8" consists of

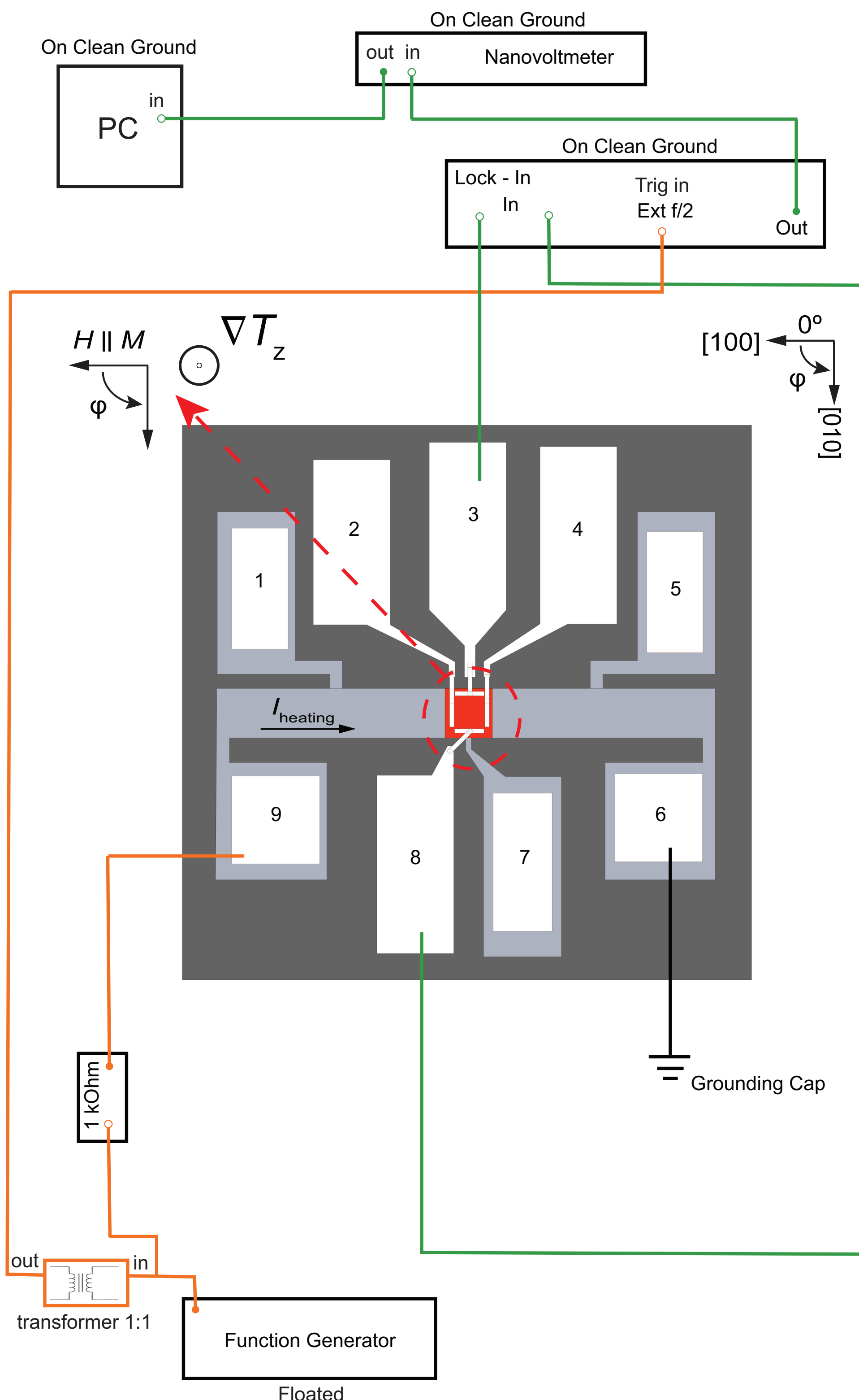

Figure 4.10: A scheme for measuring the Nernst effect of a (Ga,Mn)As / GaAs tunnel junction. A heating voltage is applied between contacts ”6” and ”9”. That results in a temperature gradient ∇T perpendicular to the device plane. An external magnetic field H is applied parallel to the device plane. The directions of the temperature gradient and the magnetic field along with the (Ga,Mn)As crystallographic axes are given with arrows. A thermomagnetic response is detected between contacts ”8” and ”3”.

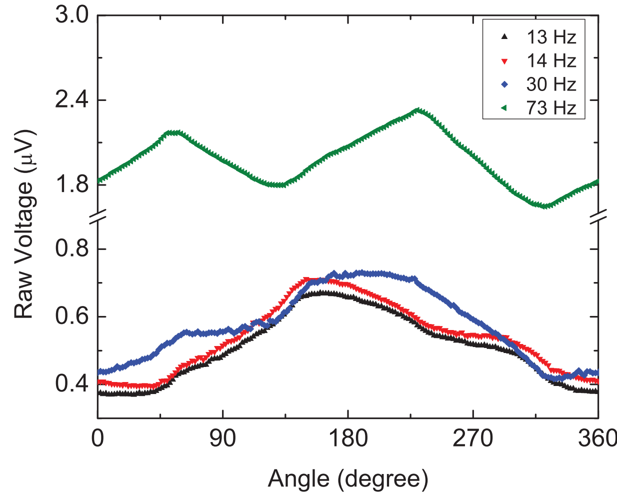

Figure 4.11: The measured voltage between contacts "3" and "8" with respect to the magnetic field direction. Curves for different frequencies of the heating current are presented. The frequency has an influence on the detected signal.

two components. One is symmetric and another is asymmetric with the direction of the applied magnetic field. The former one is frequency dependent and the second has the Nernst symmetry. The frequency dependence in this frequency range suggests that the symmetric component is kind of a spurious signal. To further verify that statement additional test are performed.

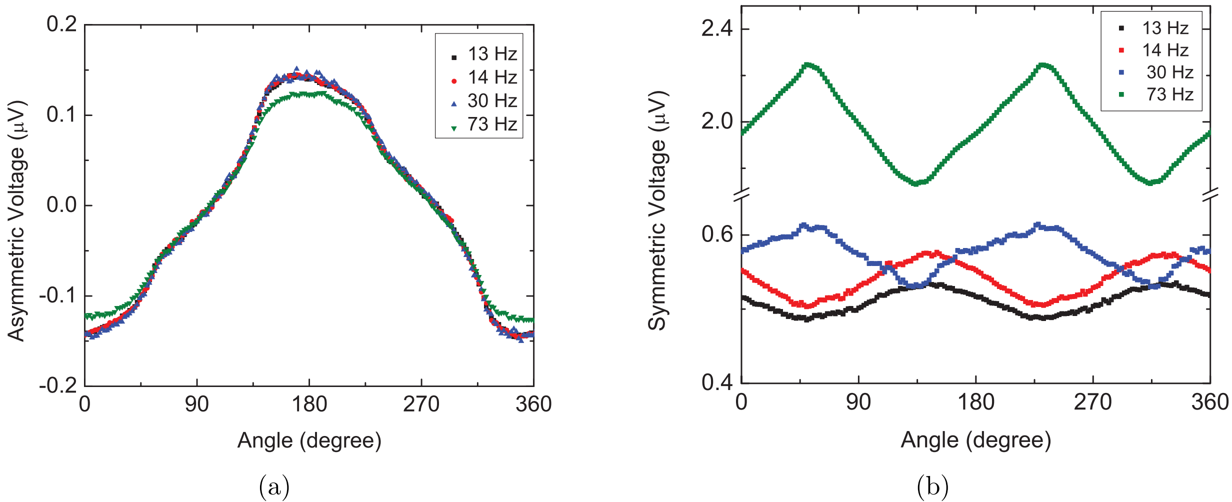

Figure 4.12: Asymmetric and symmetric components of the measured signal between contacts "3" and "8" for different frequencies of the heating current. The asymmetric component has a Nernst like symmetry and is not dependent of the frequency, while the symmetric contribution looks to depend on frequency.

In the beginning, before each measurement the Notch filter of the lock-in amplifier is adjusted to cut the $1f$ contribution to the measured signal. Afterwards, the instrument is

set to trigger at $2f$ and phase corrections are made. For each measurement, the phase is set always to be positive after being adjusted. That is the way of measuring the second harmonic of the voltage between contacts "3" and "8" in our experiment. Two voltage scans for 4 Vpp and 8 Vpp heating voltage are detected in the way described above. The results, symmetric and asymmetric are given in Fig. 4.13(a) in blue and red colour. Subsequently, the output signal of the lock-in amplifier is adjusted again for 4 Vpp and then the heating is increased to 8 Vpp. Without any Notch or phase adjustment the signal between "3" and "8" is recorded for 8 Vpp. The curves of that measurement are depicted in black in Fig. 4.13.

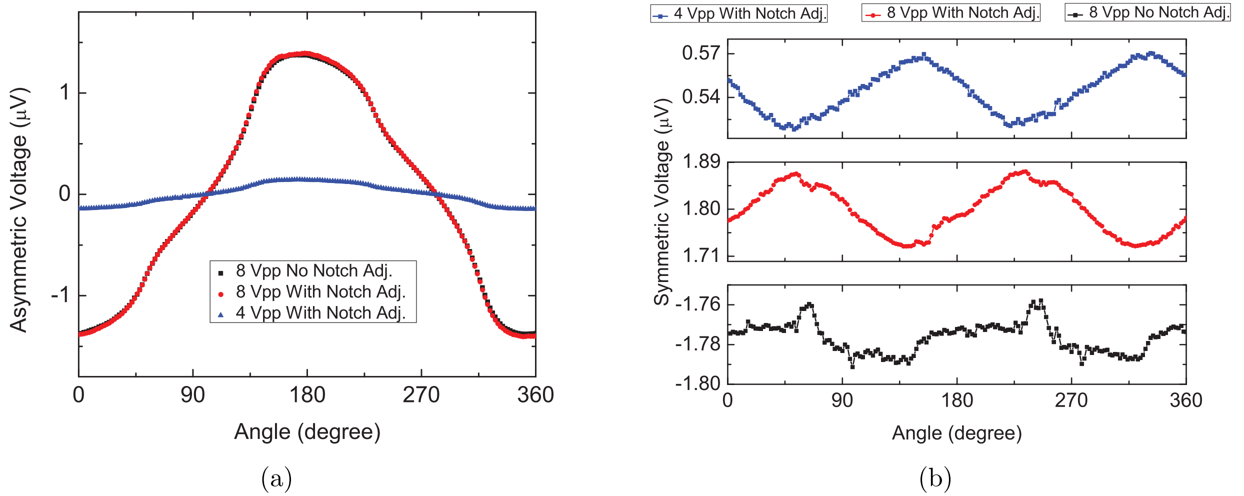

Figure 4.13: Asymmetric and symmetric components for different Notch and phase settings. The asymmetric voltage response does not appear to be sensitive to Notch and phase corrections when the heating voltage is increased. In contrast to it the symmetric component is strongly influenced by their settings.

It can be noticed that the asymmetric signal (symmetry and sign) is not influenced by the Notch settings. However, the symmetric contribution does sense these settings. Together with the frequency dependence, these both suggest that the symmetric component is kind of a spurious effect due to a capacitive coupling.

Further experiments are done with a heating current at 14 Hz. The varied parameter is the amplitude of the heating voltage. A magnetic field of 300 mT is swept in the device plane and the detection is done on contacts "3" and "8". The Lock-In amplifier is adjusted only for the first heating voltage applied. As mentioned earlier, the (Ga,Mn)As temperature stays relatively unchanged with respect to the bath temperature. Different heating voltages then mean different temperatures for the electrons in the heating channel. These should result in different temperature gradients and consequently magnitudes of the measured voltage. The results from such measurements are shown in Fig. 4.14. The raw data symmetry seems to be dominated by the symmetry of the asymmetric component (the Nernst effect contribution). The amplitude of the signal increases with increasing the

heating voltage. However, the raw signal undergoes a sign change for higher heating power. This sign change can not be simply explained by the Nernst effect theory. Therefore, before trying to look for a physical explanation, a symmetrization of the raw data is again applied and present in Fig. 4.14. From the figure it becomes obvious that the symmetric part is the one which changes its sign. The asymmetric signal, which is associated with the Nernst effect of the junction, does not undergo a sign change. Its amplitude increases when applying higher heating power (the power here is a square of the applied heating voltage).

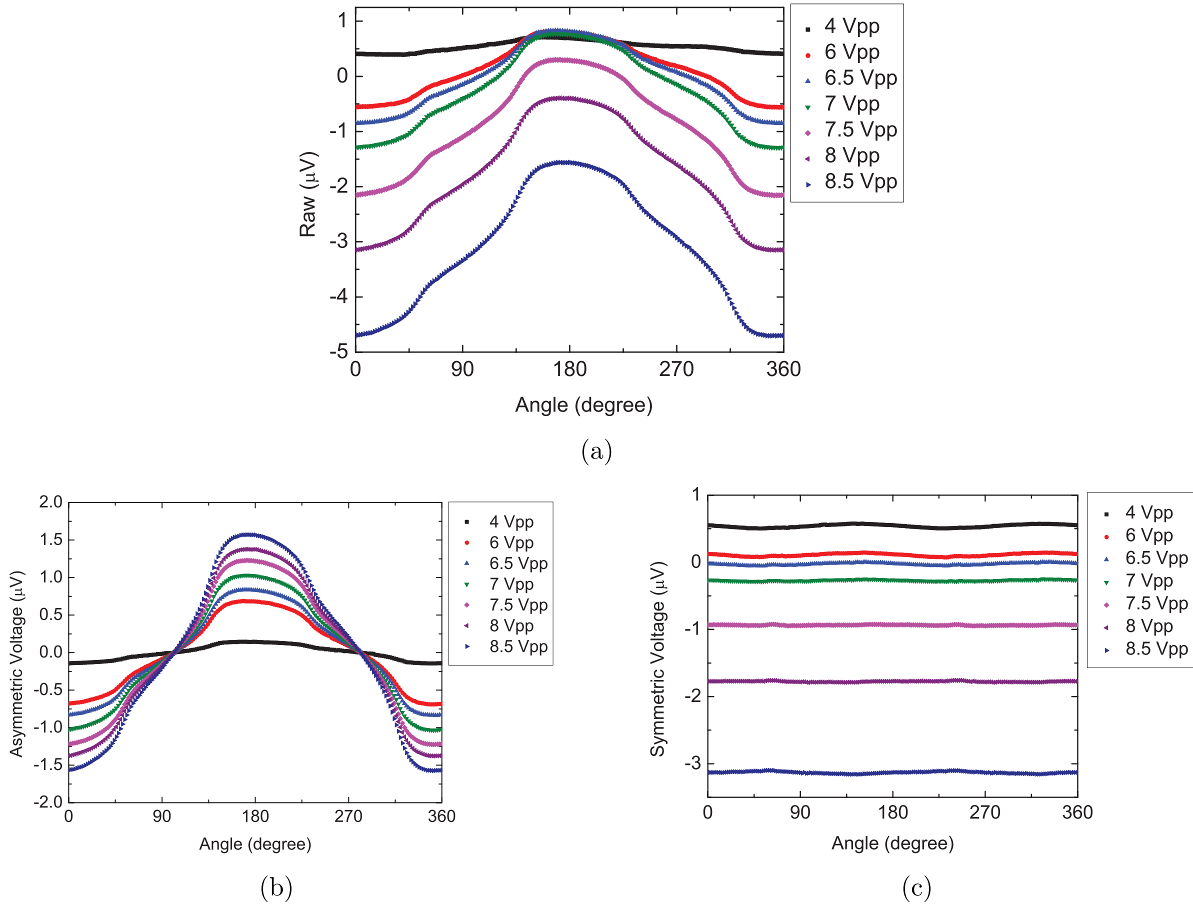

Figure 4.14: Voltage drop between contacts "3" and "8" with respect to the magnetic field direction for different heating voltages. The raw data are present along with the corresponding graphs of the asymmetric and symmetric contribution to the measured signal.

In summary, the measured voltage across the (Ga,Mn)As / GaAs junction contains two components - one symmetric and another asymmetric with the magnetic field. The symmetric part is frequency dependent and can be modified by changing the Notch settings of the Lock-In amplifier. Its value might change sign when varying the heating power. The asymmetric component does not change sign or symmetry for different frequencies or applied heating voltages. Its amplitude scales with the heating power and the

symmetry suggest that this component is actually the Nernst signal of the junction.

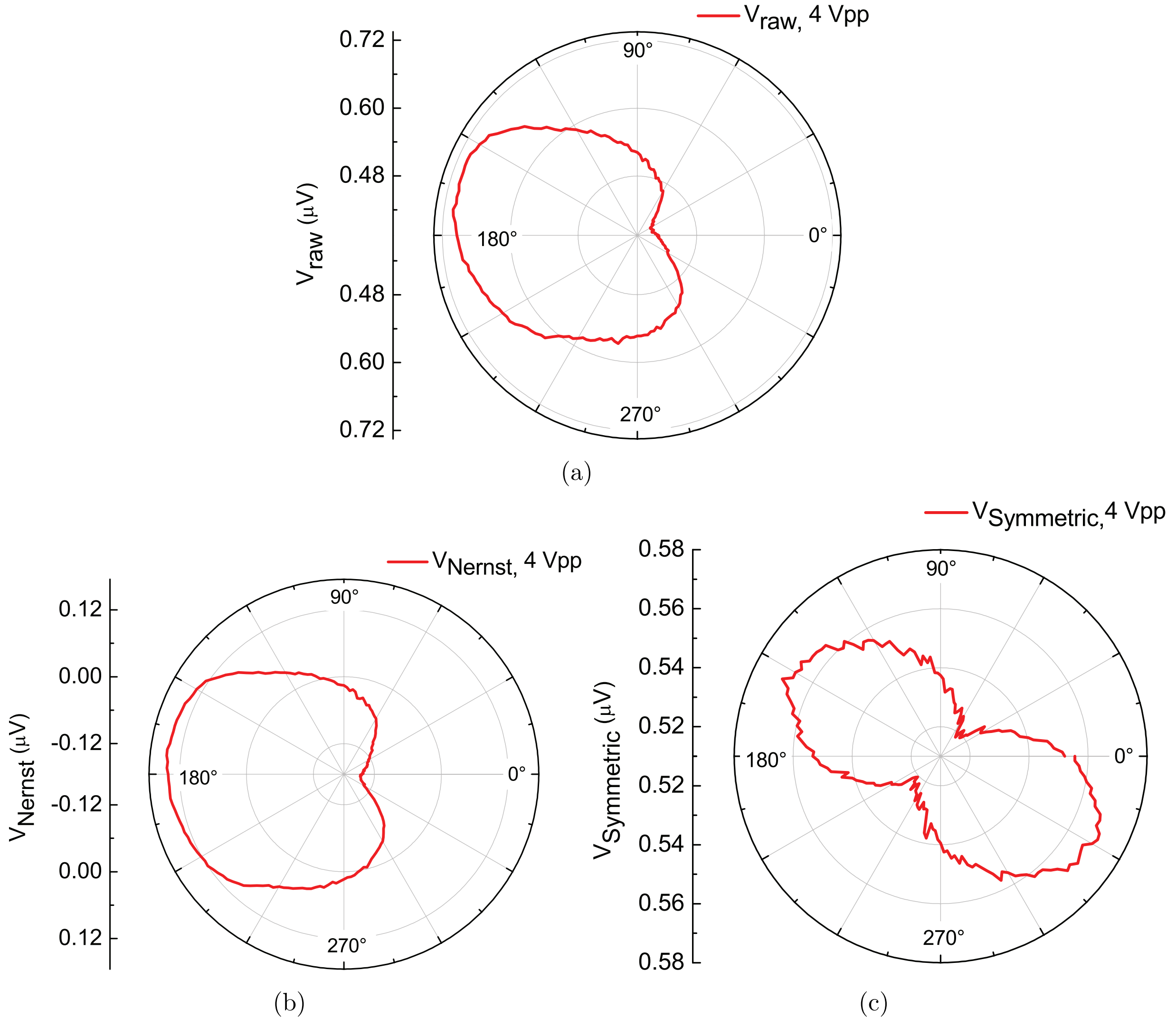

Figure 4.15: A φ-scan representation of the measured thermal signal for 4 Vpp heating voltage. For this voltage the corresponding temperature of the electrons in the heating channel is 30 K. The raw signal is split into asymmetric and symmetric component. The 0° is oriented along [100] crystal direction.

In Fig. 4.15 the measured thermal voltage across the junction for 4 Vpp heating is present in a φ-scan plot. This is done in order to emphasize the difference between the thermopower signal described in the previous chapter and the Nernst symmetry. The latter is dominant in the raw data signal in Fig. 4.15(a). Images of the Nernst signal only and the rest (the symmetric) part are depicted in Fig. 4.15(b). Both the Nernst and the symmetric component have different dependence on the magnetic field direction in comparison with the Seebeck effect from Chapter 3. Since the symmetric component is assumed to be a spurious effect, we consider only the Nernst effect (the asymmetric part).

The Nernst signal for 4 Vpp is plotted (black dots) in a 2d-plot in Fig. 4.14 with respect to the magnetic field direction.

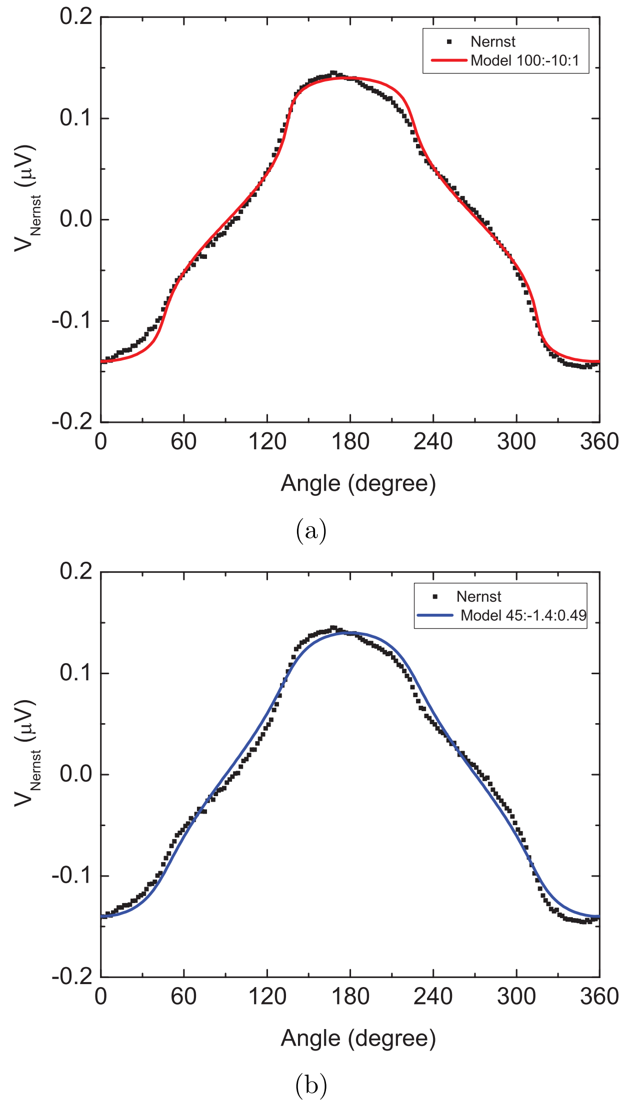

Figure 4.16: The Nernst signal for 4 Vpp heating voltage versus the magnetic field direction. The red and the blue curves are model calculations for different ratios of the anisotropy constants.

From the 2d-plot is obvious that when the magnetization is close to the 0° direction (which coincides with the [100] crystal direction), a minimum of the Nernst voltage is detected, whereas at 180° it gains a maximum value. In between these two directions the signal attains a reflection symmetry, where the 90° and 270° have similar values for the measured voltage. This description is accurate for all the asymmetric voltage scans. At this point it should be reminded that the ordinary Nernst effect is a product of two vectors - the temperature gradient and the applied magnetic field. However, only the applied magnetic field does not manage to describe the observed dependence in Fig. 4.16.

It turns out that for the correct description the magnetization of the (Ga,Mn)As layer is the important parameter. To support that statement the asymmetric part in Fig. 4.16 is fitted to a simple cosine function with a variable the angle between the magnetization direction and [100] crystal axis. This angle for 300 mT applied along different in-plane directions is calculated from the minimum of the anisotropy energy function [Papp 07a]. The latter is given with the following expression:

$$E = \frac{K_{cryst}}{4} \sin^2(2\theta) + K_{uni[\bar{1}10]} \sin^2(\theta - 135°) + K_{uni[010]} \sin^2(\theta - 90°) - MH \cos(\theta - \varphi). \tag{4.1}$$

The first term is the biaxial crystalline anisotropy contribution and the last term is the Zeeman energy. The origin of the two uniaxial terms participating in the above equation is not yet fully understood [Mark 11c]. θ and φ are the angles between the magnetization or the external field and the [100] crystal direction, respectively.

The anisotropy function is plotted in Figure 4.17 with respect to the magnetization angle θ. Two curves are presented - for magnetic fields of 0 mT and 300 mT applied along 60° with respect to [100] crystal direction. For the calculations of the function a ratio of 100:-10:1 for the different anisotropy component is considered. The "-" sign in that ratio means an easy hard axis along 45°. This ratio is taken from a comparison study on different (Ga,Mn)As layers provided by several working groups [Goul 08]. The value of the anisotropy components, however, can be also extracted from a Fingerprint measurement. Such a measurement is performed later in this chapter and from it a ratio of 45:-1.4:0.49 is estimated. The two ratios are used for the calculations and the corresponding model curves are present in Fig. 4.16.

Before comparing the two model curves with the experimental one, a comment on the role of the ratio in determining the magnetization direction is made. For that purpose, the anisotropy energy plot in Fig. 4.17 is considered. When no field is applied, the energy landscape is represented by the green curve in Fig. 4.17. The dominating biaxial anisotropy term results in four energy minima between 0° and 360°. Applying a magnetic field modifies the anisotropy energy function (the red curve in Fig. 4.17) and the numbers of the energy minima, accordingly. In the case of a 300 mT field, a single minimum is visible and it defines the preferred magnetization direction. The later is marked with a big black dot. The blue dash-line in the same graph emphasizes that the corresponding angle to the energy minimum is shifted with respect to the direction of the external magnetic field. The reason for this is that 300 mT field is not high enough to saturate the magnetization along the external field direction.

Once the angles on the magnetization for different direction are estimated for both ratios, cosine functions $V(\theta) = b * cos(\theta)$ are calculated and plotted in red and blue in Fig. 4.16. b is the amplitude of the Nernst signal. The model curves describe relatively good the observed magnetic field dependence of the measured signal. However, if one compares the two fits, the red curve with ratio taken from [Goul 08] tends to better describe the effect. The blue curve which is calculated with the ratio extracted from the

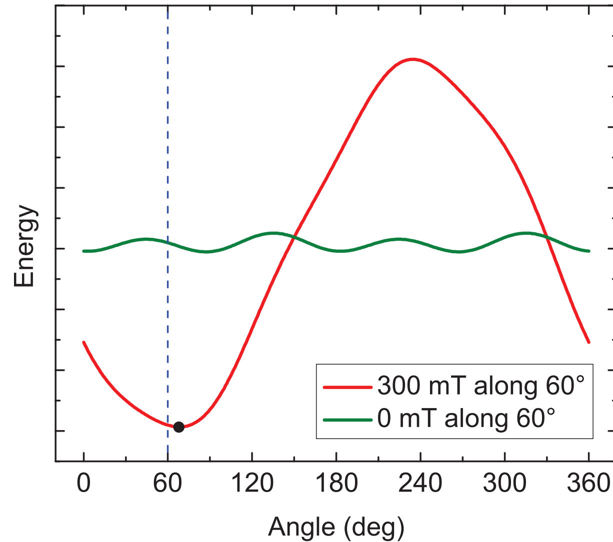

Figure 4.17: Energy landscape for 0 mT (green) and 300 mT (red) applied along 60° with regards to the [100] crystal direction. The dash-line shows the direction of the external magnetic field. The black dot presents the minimum of the function which is actually the magnetization direction.

experiment, does not describe in detail the observed dependence. The reason for this remains unclear and it requires further analysis.

To summarize, the measured effect is described with the magnetization direction and not with the external magnetic field. This suggests that the measured effect is actually the anomalous Nernst effect (ANE) of the junction. For ferromagnetic materials the anomalous Nernst effect dominates the normal Nernst effect [Niel 34].

In the following, a study on the temperature dependence of the ANE is conducted. The amplitude of the ANE is defined as the half of the difference between the Nernst voltages for 0° and 180° direction. That is measured for different temperature differences (ΔT). The latter is estimated from the WL experiment. The amplitude is then divided to the corresponding temperature difference. The product of the division, which we call the ANE coefficient, is plotted as a function of ΔT in Fig. 4.18 with the blue squares. The estimated error bars on several data points are also given.

Because the magnetization acts on the electrons moving along the temperature gradient, which is described by the ANE, one would expect that the ANE of the junction is related to its thermopower. If the latter scales linearly with ΔT that suggests a linear with ΔT ANE coefficient. To check if that is the case for the studied junction, the thermopower from Chapter 3 is plotted also in Fig. 4.18. It can be seen that for the temperature range of the thermopower measurements, the ANE coefficient is linear with ΔT (See the inset in Fig. 4.18). The linear behaviour of the thermopower in the same ΔT range is well described by the cartoon model introduced in the previous chapter. The latter assumes parabolic bands on both sides of the junction. For higher temperatures, a

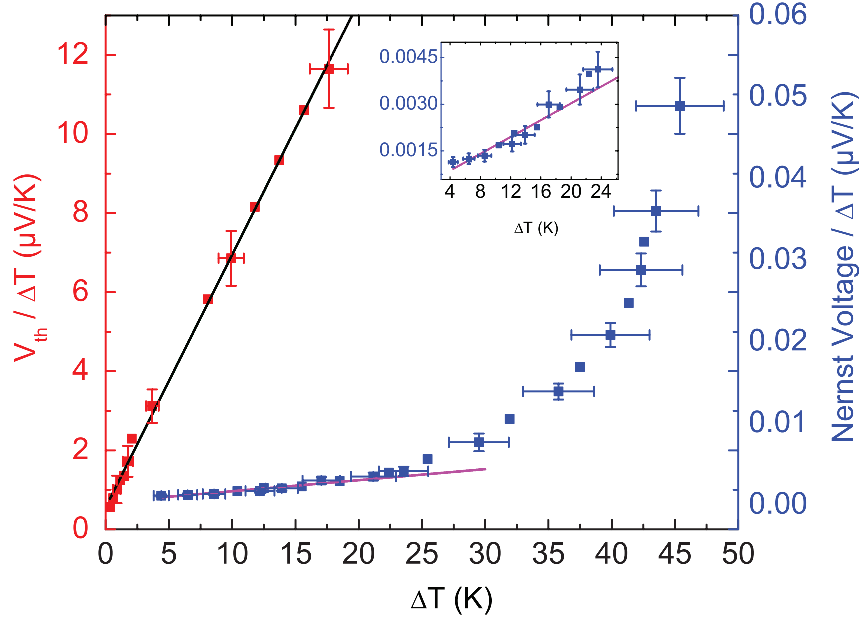

Figure 4.18: The Nernst voltage (blue squares) for different temperature difference ΔT as a function of ΔT. The thermopower (red squares) from the previous chapter is also plotted for a comparison. For a certain temperature range both coefficients have linear dependence of the applied temperature gradient. A deviation from the linearity is observed in the Nernst coefficient for higher temperature gradients.

deviation from linear behaviour is observed in the ANE coefficient vs. ΔT dependence. When the temperature is increased, the thermal broadening of the Fermi function is of order of $2k_BT$. In our experiment, this energy is roughly about 5 meV. Such broadening, as it can be seen in Fig. 2.2(b), other bands might start participating in the transport from the (Ga,Mn)As side of the junction. Consequently, the introduced cartoon model appears to be too simple to account for the observed nonlinear temperature dependence of the ANE coefficient. Further modelling including the detailed picture of the (Ga,Mn)As DOS would be required to support that explanation.

At this point, a note should be made about the term ANE coefficient. When above ANE coefficient is mentioned, this actually is not the real anomalous Nernst coefficient. The real transverse thermomagnetic coefficient is defined as:

$$\alpha_{ANE} = \frac{E_{ANE}}{m * \nabla T} \ , \tag{4.2}$$

where m is the unit vector of magnetization, ∇T is the temperature gradient and E_{ANE} is the resulting Nersnt electric field. For its calculation, the physical dimensions of the junction have to be taken into account. In addition, some assumptions should be made. The anomalous Nernst voltage which develops for an infinitesimal small temperature difference at 4.2 K is estimated from Fig. 4.18. That is found from the intercept of the linear fit for ∇T→0 K. The fit is given in magenta colour in Fig. 4.18. Its value is of about 0.32 nV/K. The (Ga,Mn)As is assumed to remain at 4.2 K and the temperature of the electrons in the

heating channel is varied. Therefore, the temperature difference is assumed to be distributed over the (Ga,Mn)As/Si:GaAs interface. A thickness d = 1 nm is assumed for this interface region. The ANE voltage is detected between voltage probes which are w = 50 μm apart. Knowing the ANE voltage, the ANE electric field can be estimated. Assuming a magnetization for the (Ga,Mn)As to be 37 kA/m ≈ 46 mT [Papp 07c], the anomalous Nernst coefficient of the junction is calculated to be - $\alpha_{ANE} \approx 1.3 * 10^{-13}$ VT^{-1}K $^{-1}$. This value is several order of magnitude smaller than all ordinary and anomalous coefficients for any material reported in the literature ([Weil 12, Weis 13] and references therein). For Co_2FeAl (CFA) with in plane magnetization (M_s = 1050 kA/m) and transverse temperature gradient, Weiler *et.al.* [Weil 12] obtained $\alpha_{ANE,CFA} = 9.5 * 10^{-8}$ VT^{-1}K^{-1}. Usually, the Nernst effect is a material property. In our case the effect is a combination of tunneling and ANE from the ferromagnetic layer. Therefore, one possible explanation for the small ANE coefficient of the studied junction might be the fact that the anomalous Nernst coefficient is a fraction of the Seebeck coefficient [Huan 11, Slac 11]. The latter is estimated to be about $\zeta = 0.5$ μV/K. That value is found also to be about three orders of magnitude smaller than the one reported in the earlier studies [Pu 06]. Another issue which might be crucial for small ANE coefficient is the small hole mobility of the (Ga,Mn)As layer. It is reported that for p-doped GaAs the lower hole mobility in comparison with the carriers in n-type gallium arsenide results in a lower absolute value of the anomalous Nernst coefficient [O Em 61]. More detailed modelling and analysis are required for more precise justification of the coefficient.

4.5 ANE magnetic field sweeps and Nernst Fingerprints

This section studies the response of ANE to a magnetic field sweep. It aims to support the fact that the measured voltage is related to the ANE of the (Ga,Mn)As layer. For this purpose, the voltage drop on contact pair "3" - "8" is recorded when the field is swept from -300 mT to 300 mT along different in-plane directions. Figure 4.19 presents several scans for different angles in the (100) plane. The scans are not symmetrized. The curves are recorded for a temperature difference of about 25 K (applied 4 Vpp heating voltage). The bath temperature is at 4.2 K.

As it can be noticed from Fig. 4.19, the measured voltage at 0 T B field is different for different angle scans. Three different values of the voltage are measured for 40°, 70° and 140° at B = 0 mT. For non-magnetic materials this zero-field voltage is zero, whereas for a ferromagnetic semiconductor this is not obviously the case. Once the material is magnetized in a certain direction and the field is removed, the magnetization relaxes along the closest (in terms of energy) magnetic easy axis. This initial state of the magnetic layer determines the zero-field response known as anomalous Nernst effect. The latter is proportional to the cross product of the sample magnetization and the applied temperature

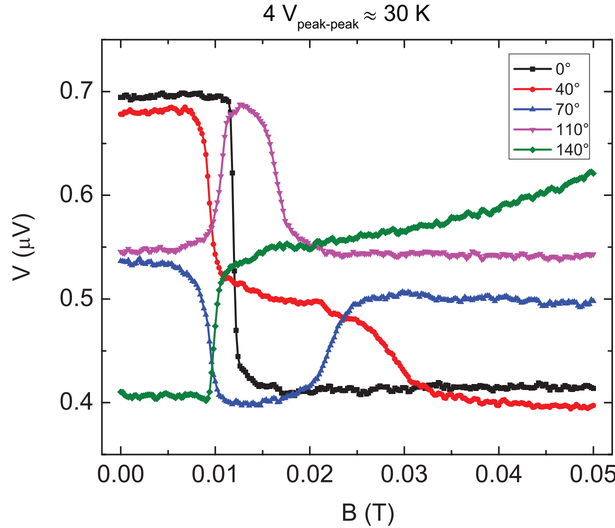

Figure 4.19: The Nernst signal for magnetic field sweeps along different in-plane directions. The bath temperature is 4.2 K, while the temperature of the electrons in the channel is about 30 K. The 0° coincides with the [100] crystal direction.

gradient.

Along with the anisotropic non-zero voltage at 0 T, the voltage scans reveal pure single or double switching events. Not surprisingly, these events can be explained with magnetization dynamics of the ferromagnetic biaxial (Ga,Mn)As. The observed cubic magnetic anisotropy in this material is the reason for the magnetic reversal process via two 90° switches [Cowb 95]. From the positions of the switches, the characteristic switching fields for the (Ga,Mn)As, H_{c1} and H_{c2} can be extracted. To demonstrate that the magnetization reversal of the (Ga,Mn)As layer is responsible for the switching events in the measured signal in Fig. 4.19, the 70° voltage scan is described. Prior to every magnetic field sweep, the sample magnetization is saturated along a certain direction, in this case the 70° direction, applying -300 mT (not shown in the graph). Then the magnetic field is reduced to 0 mT and swept to positive fields. During the sweep from negative to small positive fields the magnetization relaxes to the closest easy axis which for the 70° direction is $[0\bar{1}0]$. In this magnetization configuration, the electric field developed to balance the Lorenz force acting on the carriers moving along the temperature gradient has a zero cross section with contacts ”3” and ”8”. Thus no Nernst signal is measured but only the previuoly discussed symmetric component due to a capacitive pick-up. Further sweeping the field, at a certain small positive field H_{c1} a 90°-DW nucleates and propagates through the layer. This results in a reorientation of the magnetization M direction to the $[\bar{1}00]$ direction. When M is parallel to $[\bar{1}00]$, a maximum cross section with the detecting probes is yielded. An abrupt change in the measured voltage drop between contacts ”3” and ”8” is then recorded. This corresponds to the first switching event observed in Fig. 4.19 for the 70° curve. When increasing the magnetic field to a certain value (H_{c2}), another 90°-DW forces the magnetization close to the [010] easy axis. Here, a second abrupt change in

the voltage is observed. The cross product of M and the temperature gradient - E-field - has a zero cross section with the detecting contacts "3" - "8". Continuing increasing the external magnetic field, the magnetization rotates towards the field direction. The scans for the other angles can be explained in the same manner. A point should be made, that the amplitude of the switch in the 0° curve is equal to the amplitude of the effect determined from the φ-scan for the same heating voltage. The switching event for the 0°-curve is related to the nucleation and propagation of 180°-DW. Therefore, one can conclude that the voltage scans are dominated by the anomalous Nernst effect of the ferromagnetic contact. Each switching event can be completely described by the magnetization reversal process of (Ga,Mn)As layer which behaves like a macro spin. This description of the observed thermomagnetic effect favours the fact that the observed anomalous-Nernst effect appears to be very sensitive to the magnetic anisotropies of the ferromagnetic layer, also reported for Heusler compounds [Weil 12].

In addition, the anisotropies of the anomalous Nernst effect of the (Ga,Mn)As / GaAs junction are studied. The voltage scans for every 5° to 360° are collected for contact pair "3" - "8". For each direction the magnetic field is swept from -300 mT up to 300 mT. A compilation of all the curves is plotted in a Voltage Polar Plot (VPP) graph in Figure 4.20. The VPP is similar to the earlier reported RPP [Papp 07b].

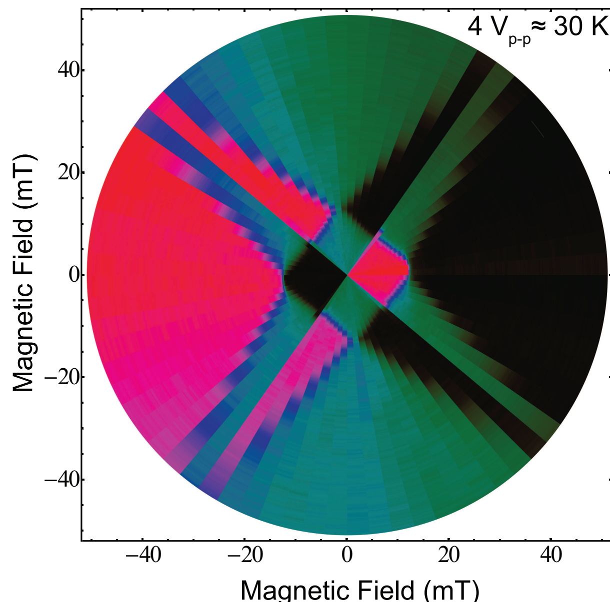

Figure 4.20: A Voltage Polar Plot of the anomalous Nernst signal for a temperature of the electrons in the Si:GaAs channel of about 30 K. That gives a temperature difference of about 25 K. The magnetic field is applied in-plane and the colour code is as follow: green - low, blue - middle, red - high Nernst voltage.

Only the low field region from -50 mT to 50 mT is present in the Fig. 4.20. For the fingerprint, the following colour code is used: green corresponds to a small value of the Nernst voltage, blue is for an intermediate value and the red is for high voltage. This

fingerprint is similar to these from AMR, Planar Hall or TAMR experiments [Goul 04]. However, there are also some differences as the three states which are observed. In the case of AMR/TAMR usually there are only two states - low and high resistance state. Here, high, middle and low voltages can be recognized. Nevertheless, when we say three states this does not mean that there are three favourable magnetization directions. The magnetization preferred directions are determined from the rectangle pattern in Fig. 4.20. The (Ga,Mn)As remains biaxial so there are two magnetic easy axis which are along the diagonals of the rectangle - [100] and [010] crystal directions, accordingly. The colour code itself is related to the specifics of the Nernst geometry in combination with the cubic magnetic anisotropy of the (Ga,Mn)As. Using the polar plot, the basic anisotropy components can be extracted. The domain wall nucleation energy ϵ/M, given by the length of the diagonals, is calculated to be about 12.4 mT. The uniaxial anisotropies components are also calculated from the same region in the VPP and they are as follow: $K_{uni[110]}/K_{cryst} = 3.1$ % and $K_{uni[010]}/M = 0.5$ mT. These values of the uniaxial anisotropy are lower in comparison with the usually observed ones. The fact that they are smaller with respect to the biaxial term is a good proof that the (Ga,Mn)As, despite the current heated Si:GaAs, remains at about 4.2 K.

Similar fingerprint is also recorded for contact pair "2" and "4" and shown in the Appendix.

Further, the influence of a higher by means of amplitude applied heating voltage on the anomalous Nernst signal is studied. Figure 4.21 presents the Nersnt voltage for 10 Vpp applied heating voltage. That corresponds to a temperature difference of about 45 K (as determined from the WL experiment).

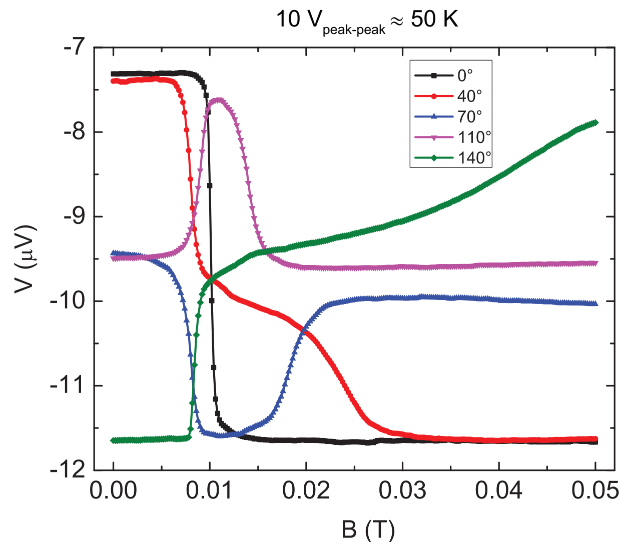

Figure 4.21: The ANE signal for a temperature difference of about 45 K and different magnetic field directions.

Switching events are still present in the measured voltage scans for 10 Vpp heating

voltage. They are similar to the ones for 25 K temperature difference and are related to the magnetisation reversal process of the ferromagnetic layer.

A compilation of all the scans at $\Delta T \approx 25$ K from 0° to 360° is present in a VPP in Fig. 4.22. From the fingerprint it is obvious that the biaxial anisotropy is still the dominating anisotropy. The anisotropy constants are estimated from the fingerprint to be: $\epsilon/M = 10.6$ mT, $K_{uni[010]}/M = 0.4$ mT $K_{uni[110]}/K_{cryst} = 0.6$ %. These values, however, are not exact numbers. Therefore, they should not be used for a comparison. However, a slight change in the size of the inner square for the 10 Vpp VPP with respect to the 4 Vpp one can be noticed.

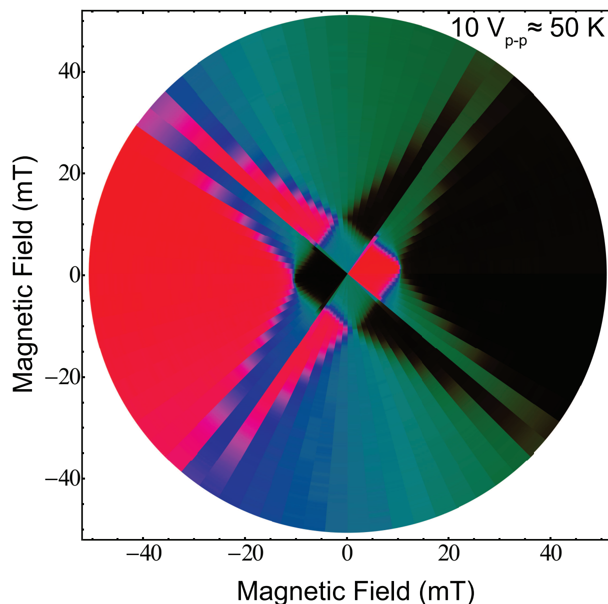

Figure 4.22: The ANE Voltage Polar Plot for a temperature of the electrons in the Si:GaAs channel of about 50 K. That gives a temperature difference of about 45 K. The colour code remains as the one for the VPP from Fig. 4.20: green - low, blue - middle, red - high Nernst voltage.

To make this change more visible, the normalized value of the Nernst voltage scans for 4 Vpp and 10 Vpp heating voltage are plotted in the same graph in Fig. 4.23.

The 110° curves for the two temperature differences are shown in Fig. 4.23(a). A double-step switching event is recorded for both heating voltages. There is a clear change in the switching fields H_{c1} and H_{c2}, as well a change in the width of the double-step switching. For the higher temperature difference these parameters move to smaller values. An interesting observation is that the H_{c1} changes less than H_{c2} for different temperature differences. This might be related to a possible difference in the temperature dependence of the DW nucleation/propagation energy and that of the coherent rotation. The first defines the H_{c1} and depends on crystal defects. The coherent rotation depends on the magnetization (anisotropies) and is associated with the H_{c2}. Therefore, a different temperature dependence might be expected. The justification of that statement requires

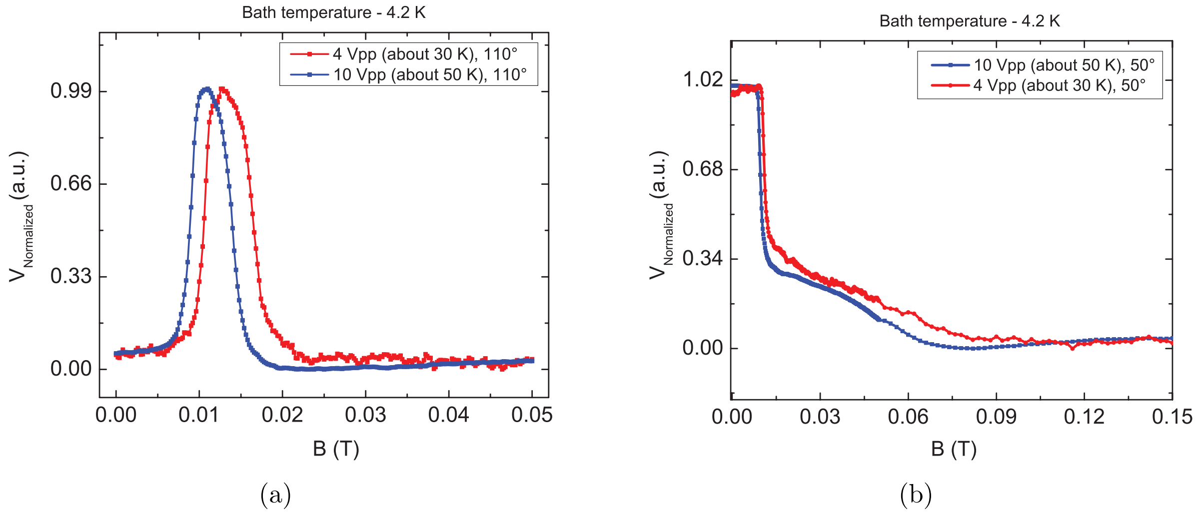

Figure 4.23: A comparison of the Nernst voltage sweeps for two different heating voltages. In the first graph on the left the switching fields are demonstrated to depend on the temperature difference. In the graph on the right hand side the anisotropic field is shown to depend on the applied Joule heating.

additional studies. If the change of H_{c2} is about 4 mT for $\Delta T = 20$ K and the change is assumed to depend linearly on ΔT, for $\Delta T = 1$ K, the H_{c2} is expected to change with 0.2 mT. The change can be attributed to a heating of the (Ga,Mn)As electron system. That can influence the crystalline anisotropy. To demonstrate it, the Nernst voltage is measured along the magnetic hard axis of the (Ga,Mn)As layer, estimated to be along 50°. The latter is usually along 45°, but the sample is rotated about 5° form the 0° direction of the magnetic field in the cryostat. The rotation is observed also in the measured φ-scan and the fingerprints. The 50° curves for 4 Vpp and 10 Vpp heating are shown in Fig. 4.23(b). The anisotropy field slightly changes to smaller values when increasing the temperature difference.

Another set of measurements is done, where the Nernst effect and its anisotropies are investigated at bath temperature of 30 K. 10 Vpp are used for these experiments. It results in about 50 K temperature of the electrons in the channel, and therefore 20 K temperature difference across the junction. Figure 4.24 shows a saturation φ-scan of the ANE contribution to the measured total signal.

The symmetry of the φ-scan is slightly different than one at 4.2 K present in Fig. 4.15(b). This can be explained with the change of the anisotropy constants with increasing bath temperature. That statement is supported by voltage scans along different in-plane directions. Single curves are given in Fig. 4.25 and a compilation of all the measured Nernst scans for angles between 0° and 360° is present in Fig. 4.26. For both graphs it is obvious that the switching events become smaller when the bath temperature is increased. The size of the inner region, which corresponds to the H_{C1}, is smaller than these of Fig. 4.20 and Fig. 4.22. Determination of the anisotropy constants at 30 K bath temperature is

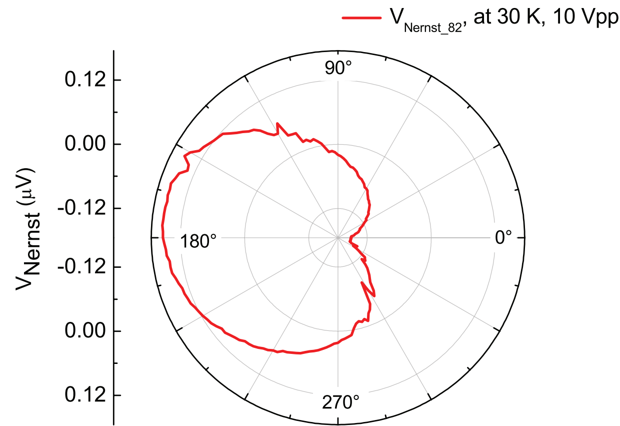

Figure 4.24: A saturation φ-scan of the anomalous Nernst effect of the (Ga,Mn)As / GaAs tunnel junction at a bath temperature of 30 K and a temperature difference of about 20 K.

more complex [Papp 07c] and only a qualitative description is given here. The small uniaxial anisotropy at 4.2 K stars to dominate and modifies the energy landscape at higher temperatures. That causes respectively changes in the magnetization reversal and consequently in the Nernst response.

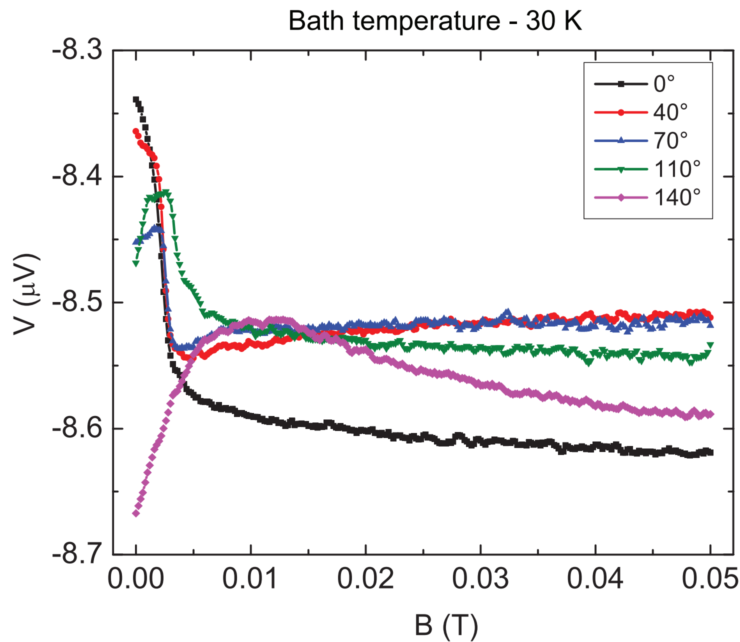

Figure 4.25: Anomalous Nernst scans for different in-plane magnetic field directions at 30 K bath temperature and 20 K temperature difference across the measured junction.

In conclusion, the anomalous Nernst effect of a (Ga,Mn)As / GaAs tunnel junction is measured. The ANE appears to be sensitive to the electron temperature and to the anisotropies of the ferromagnetic layer. A cosine function with a parameter the magnetization angle is used to describe the observed magnetic field dependence of the ANE. The

temperature dependence of the ANE is studied. Below a certain temperature difference, the relation gains a linear dependence. Above that difference it becomes nonlinear with temperature. A possible explanation is the thermal broadening of the (Ga,Mn)As Fermi function. This broadening might result in an additional contribution of other (Ga,Mn)As bands to the transport, which the cartoon model does not take into account. Further theoretical modelling of the Nernst effect of a (Ga,Mn)As / GaAs tunnel junction would be required to support that statement. That is considered as a future work. Moreover, such model might also explain the considerably smaller value of the estimated anomalous Nernst coefficient.

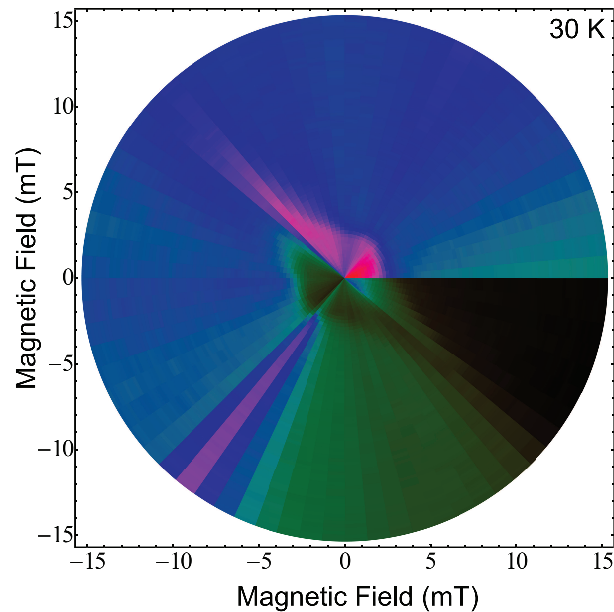

Figure 4.26: ANE Fingerprint at bath temperature of about 30 K and temperature difference of about 20 K. It is obvious that the uniaxial anisotropy dominates at higher bath temperature. A small temperature drift causes the colour change in the last quadrant with respect to the first one.

Chapter 5

Conclusion and Outlook

In this thesis the diffusion thermopower (the Seebeck effect) and the Nernst effect of a (Ga,Mn)As / GaAs tunnel junction are studied. The different interfaces between the layers in the junction benefit a reduced phonon drag contribution. A heating current technique [Gall 90, Jong 95, Mole 90] is used to create a local temperature gradient. An AC current heats the electrons in a heating channel (bottom of the junction), while the device temperature is not significantly affected. That results in a temperature difference across the studied junction and a generation of a thermal voltage. A standard lock-in technique at double the frequency of the heating current is used for measuring the voltage. Locking at $2f$ provides a selective detection for signals of thermoelectric / thermomagnetic origin. The temperature difference is monitored by means of the Weak Localization (WL) effect.

Chapter 3 describes in detail the arising thermal voltage or the Seebeck voltage across the studied junction with one top contact. The calculated thermopower of the junction has a linear dependence on temperature. Phonon drag effects, which are usually highly nonlinear with temperature, are not observed. This hints that only diffusion thermopower is measured. The electronic contribution to the Seebeck coefficient of the junction at 4.2 K is estimated to be 0.5 μV/K. The latter is about three orders of magnitude smaller than the reported to date experimental values. However, it appears to be consistent with the calculations of the introduced cartoon model.

Furthermore, the behaviour of the diffusion thermopower in an external magnetic field is studied. The thermovoltage is found to be anisotropic with the applied magnetic field. The symmetry of the signal is different than the AMR-like one reported by Pu *et al.* for bulk (Ga,Mn)As [Pu 06]. Switching events are observed in the detected thermal voltage when the magnetic field is swept from negative to positive values. They are associated with the magnetization reversal in the magnetic layer and remind of a spin-valve signal. This observation suggests that the experiments on spin-detection and spin-injection should be done with great care, since thermal effects can be also present and they might be anisotropic with the magnetic field. Furthermore, the values for the switching fields for different angles are extracted and then plotted in a polar plot. The plot is similar to

previously reported TAMR measurements [Goul 04]. It consists of an inner region with a rectangular shape. This corresponds to a biaxial anisotropy of the (Ga,Mn)As layer and it suggests that the (Ga,Mn)As remains at 4.2 K, while the electron system of the Si:GaAs channel is heated.

To complete the study on the thermopower, a simple cartoon model is introduced to estimate the Seebeck coefficient of the junction. Assuming a position of the Fermi level below the top of the valence band for the (Ga,Mn)As site, the calculated Seebeck coefficient is in good agreement with the obtained experimental value. The sensitivity to the position of the Fermi level suggests that the thermopower can be further used to map the density of states (DOS) near the metal - insulator transition.

Chapter 4 reports on the Nernst effect of a (Ga,Mn)As / GaAs tunnel junction. The experiment is performed with a new device geometry. Instead of a single top contact on the junction four voltage probes are fabricated. A transverse temperature gradient is established across the junction and an external magnetic field is swept in the device plane. As a result, a magnetothermal voltage is detected between each two opposite contacts. It consists of two components: one symmetric and another asymmetric with respect to the magnetic field. The symmetric component appears to be kind of a spurious signal due to kind of a capacitive coupling. The asymmetric part is governed by the magnetization of the ferromagnetic layer. Therefore, that component is attributed to the anomalous Nernst effect (ANE) of the junction. The ANE coefficient is found to depend linearly on the temperature difference (ΔT) for the temperature range of the thermopower measurements. Above theat range, the dependence becomes nonlinear. The anomalous Nernst coefficient is estimated to be several orders of magnitude smaller than all the ordinary and anomalous Nernst coefficients reported in the literature. This might be related to the small Seebeck coefficient of the junction, given in the previous chapter. Study of this relation between the two coefficients of the junction is considered as a part of a future work.

Switching events are observed in the Nernst signal similar to the thermopower. They can be completely described with the magnetization reversalof the ferromagnetic layer. The collected fingerprints show mainly a biaxial anisotropy of the (Ga,Mn)As. Instead of two states, which is the case for TAMR and AMR, three states are noticed for the Nernst effect geometry. In summary, the Seebeck and the Nernst effects of (Ga,Mn)As / GaAs junction have a strong dependence on the detail of the DOS of the ferromagnetic contact. Strong spin-orbit coupling, which governs the anisotropies in the (Ga,Mn)As DOS, results in anisotropic thermopower and anomalous Nernst voltage. These can be further utilized to map the DOS near the metal - insulator transition.

Appendix A

Appendix

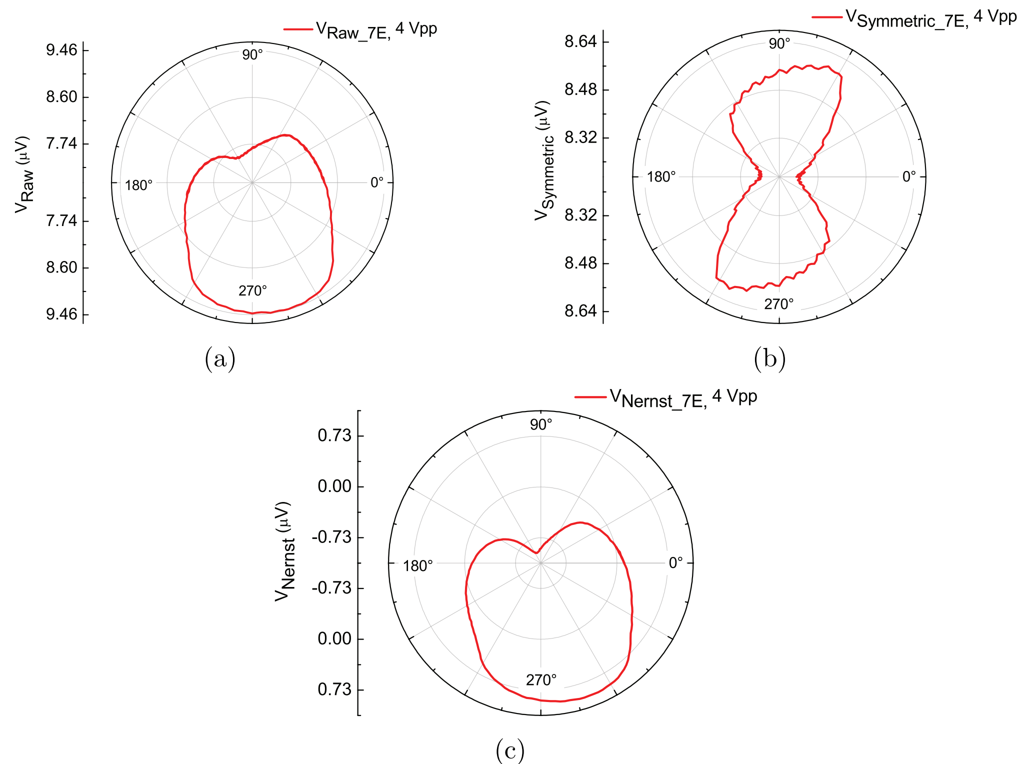

Figure A.1: Saturation φ-scans of the raw, symmetric and Nernst component of the measured signal between contacts "2" and "4". For this measurement the grounding cap is on contact "B" (See Fig. 4.10). An ac-voltage with frequency of 2 Hz and amplitude of 4 Vpp is applied on the heating channel. As it can be seen, the Nernst signal is 90° rotated with respect to the one measured on contact pair "3" - "8" (See Fig. 4.15(b)).

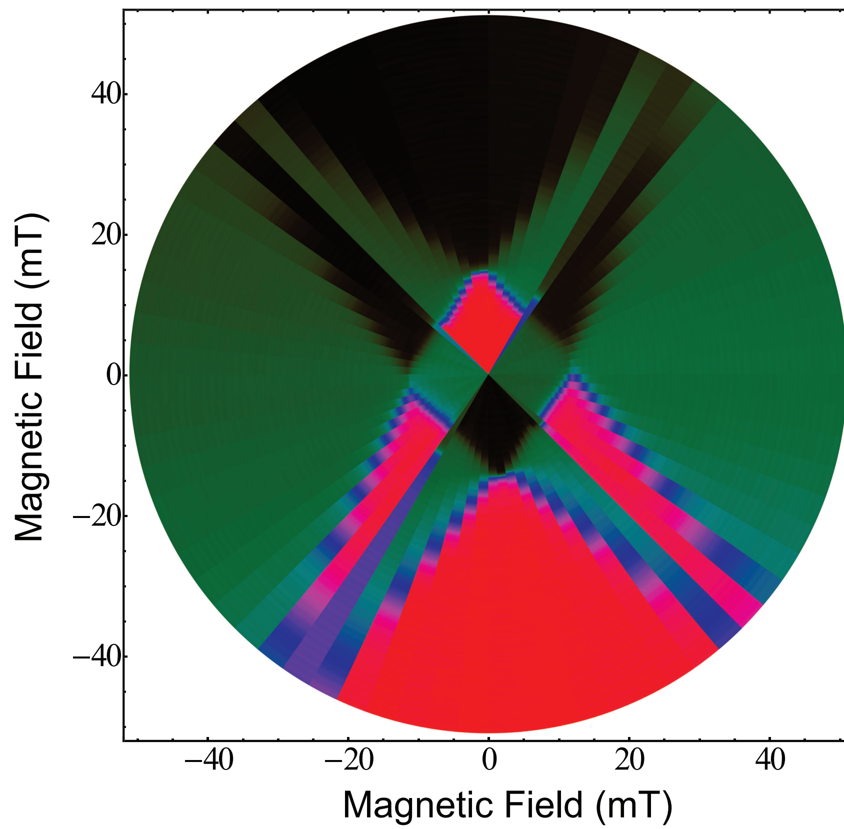

Figure A.2: Fingerprint of the Nernst signal measured on contact pair "2" - "4". The pattern is 90° rotated with respect to that of the signal from pair "3" - "8" (see Fig. 4.20). It can be noticed, that the fingerprint is kind of deformed. That is found to be due to a magnet power supply misbehaviour, which is fixed for the measurements present in the Chapter 4.

Bibliography

[AAke 02] J. J. Åkerman, R. Escudero, C. Leighton, S. Kim, D. Rabson, R. W. Dave, J. Slaughter, and I. K. Schuller. *Journal of Magnetism and Magnetic Materials*, Vol. 240, No. 13, pp. 86–91, 2002.

[Adac 10] H. Adachi, K. Uchida, E. Saitoh, J. Ohe, S. Takahashi, and S. Maekawa. *Appl. Phys. Lett.*, Vol. 97, No. 25, pp. 252506–3, 2010.

[Alts 80] B. L. Altshuler, A. G. Aronov, and P. A. Lee. *Phys. Rev. Lett.*, Vol. 44, No. 19, pp. 1288–1291, 1980.

[Amma 92] M. Amman, E. Ben-Jacob, and J. Cohn. *Physics Letters A*, Vol. 171, No. 56, pp. 389–396, 1992.

[Ando 98] T. Ando, T. Nakanishi, and R. Saito. *Journal of the Physical Society of Japan*, Vol. 67, No. 8, pp. 2857–2862, 1998.

[Ashc 76] N. Ashcroft and D. Mermin. *Solid state physics*. Thomson Learning, Toronto, 1976.

[Aume 99] J. Aumentado, V. Chandrasekhar, J. Eom, P. M. Baldo, and L. E. Rehn. *Appl. Phys. Lett.*, Vol. 75, No. 22, pp. 3554–3556, 1999.

[Awsc 07] D. D. Awschalom and M. E. Flatte. *Nat Phys*, Vol. 3, No. 3, pp. 153–159, 2007.

[Baib 88] M. N. Baibich, J. M. Broto, A. Fert, F. N. Van Dau, F. Petroff, P. Etienne, G. Creuzet, A. Friederich, and J. Chazelas. *Phys. Rev. Lett.*, Vol. 61, No. 21, pp. 2472–2475, 1988.

[Bakk 10] F. L. Bakker, A. Slachter, J. Adam, and B. J. van Wees. *Physical Review Letters*, Vol. 105, No. 13, pp. 136601–+, 2010.

[Barn 72] R. D. Barnard. *Thermoelectricity in Metals and Alloys*. 1972.

[Baue 10] G. E. Bauer, A. H. MacDonald, and S. Maekawa. *Solid State Communications*, Vol. 150, No. 11-12, pp. 459–460, 2010.

[Baue 12] G. E. W. Bauer, E. Saitoh, and B. J. van Wees. *Nat Mater*, Vol. 11, No. 5, pp. 391–399, 2012.

[Baxt 02] D. V. Baxter, D. Ruzmetov, J. Scherschligt, Y. Sasaki, X. Liu, J. K. Furdyna, and C. H. Mielke. *Physical Review B*, Vol. 65, No. 21, p. 212407, 2002.

[Berg 12] K. von Bergmann, M. Menzel, D. Serrate, Y. Yoshida, S. Schrder, P. Ferriani, A. Kubetzka, R. Wiesendanger, and S. Heinze. *Phys. Rev. B*, Vol. 86, No. 13, pp. 134422–, 2012.

[Berg 83] G. Bergmann. *Phys. Rev. B*, Vol. 28, No. 2, pp. 515–522, 1983.

[Berg 84] G. Bergmann. *Physics Reports*, Vol. 107, No. 1, pp. 1–58, 1984.

[Bina 89] G. Binasch, P. Grünberg, F. Saurenbach, and W. Zinn. *Phys. Rev. B*, Vol. 39, No. 7, pp. 4828–4830, 1989.

[Borz 04] T. Borzenko, C. Gould, G. Schmidt, and L. W. Molenkamp. *Microelectronic Engineering*, Vol. 75, No. 2, pp. 210–215, 2004.

[Bosu 11] S. Bosu, Y. Sakuraba, K. Uchida, K. Saito, T. Ota, E. Saitoh, and K. Takanashi. *Phys. Rev. B*, Vol. 83, No. 22, pp. 224401–, 2011.

[Call 48] H. B. Callen. *Phys. Rev.*, Vol. 73, No. 11, pp. 1349–1358, 1948.

[Cior 09] M. Ciorga, A. Einwanger, U. Wurstbauer, D. Schuh, W. Wegscheider, and D. Weiss. *Phys. Rev. B*, Vol. 79, No. 16, p. 165321, 2009.

[Cowb 95] R. P. Cowburn, S. J. Gray, J. Ferre, J. A. C. Bland, and J. Miltat. *Journal of Applied Physics*, Vol. 78, No. 12, pp. 7210–7219, 1995.

[Cutl 69] M. Cutler and N. F. Mott. *Phys. Rev.*, Vol. 181, No. 3, pp. 1336–1340, 1969.

[Delv 65] R. T. Delves. *Reports on Progress in Physics*, Vol. 28, No. 1, p. 249, 1965.

[Diet 00] T. Dietl, H. Ohno, F. Matsukura, J. Cibert, and D. Ferrand. *Science*, Vol. 287, No. 5455, pp. 1019–1022, 2000.

[Doer 38] W. Doering. *Ann. Physik*, Vol. 32, p. 259, 1938.

[Esak 58] L. Esaki. *Phys. Rev.*, Vol. 109, No. 2, pp. 603–604, 1958.

[Flet 99] R. Fletcher. *Semiconductor Science and Technology*, Vol. 14, No. 4, pp. R1–, 1999.

[Flip 12] J. Flipse, F. L. Bakker, A. Slachter, F. K. Dejene, and B. J. van Wees. *Nat Nano*, Vol. 7, No. 3, pp. 166–168, 2012.

[Gall 90] B. L. Gallagher, T. Galloway, P. Beton, J. P. Oxley, S. P. Beaumont, S. Thoms, and C. D. W. Wilkinson. *Phys. Rev. Lett.*, Vol. 64, No. 17, pp. 2058–2061, 1990.

[Goen 12] S. T. B. Goennenwein and G. E. W. Bauer. *Nat Nano*, Vol. 7, No. 3, pp. 145–147, 2012.

[Gold 09] H. J. Goldsmid. *Introduction to Thermoelectricity.* 2009.

[Goul 04] C. Gould, C. Rüster, T. Jungwirth, E. Girgis, G. M. Schott, R. Giraud, K. Brunner, G. Schmidt, and L. W. Molenkamp. *Physical Review Letters*, Vol. 93, No. 11, p. 117203, 2004.

[Goul 08] C. Gould, S. Mark, K. Pappert, R. G. Dengel, J. Wenisch, R. P. Campion, A. W. Rushforth, D. Chiba, Z. Li, X. Liu, W. V. Roy, H. Ohno, J. K. Furdyna, B. Gallagher, K. Brunner, G. Schmidt, and L. W. Molenkamp. *New Journal of Physics*, Vol. 10, No. 5, p. 055007, 2008.

[Hals 10] K. M. Hals, A. Brataas, and G. E. Bauer. *Solid State Communications*, Vol. 150, No. 1112, pp. 461–465, 2010.

[Hana 08] N. Hanasaki, K. Sano, Y. Onose, T. Ohtsuka, S. Iguchi, I. Kézsmárki, S. Miyasaka, S. Onoda, N. Nagaosa, and Y. Tokura. *Phys. Rev. Lett.*, Vol. 100, No. 10, pp. 106601–, 2008.

[Here 01] J. P. Heremans, C. M. Thrush, and D. T. Morelli. *Phys. Rev. Lett.*, Vol. 86, No. 10, pp. 2098–2101, 2001.

[Hout 92] H. van Houten, L. W. Molenkamp, C. W. J. Beenakker, and C. T. Foxon. *Semiconductor Science and Technology*, Vol. 7, No. 3B, pp. B215–, 1992.

[Huan 11] S. Y. Huang, W. G. Wang, S. F. Lee, J. Kwo, and C. L. Chien. *Phys. Rev. Lett.*, Vol. 107, No. 21, pp. 216604–, 2011.

[Hump 07] S. Hümpfner, K. Pappert, J. Wenisch, K. Brunner, C. Gould, G. Schmidt, L. W. Molenkamp, M. Sawicki, and T. Dietl. *Appl. Phys. Lett.*, Vol. 90, No. 10, pp. 102102–3, 2007.

[Jan 57] J. P. Jan. "Galvamomagnetic and Thermomagnetic Effects in Metals". pp. 1–96, Academic Press, 1957.

[Jawo 10] C. M. Jaworski, J. Yang, S. Mack, D. D. Awschalom, J. P. Heremans, and R. C. Myers. *Nat Mater*, Vol. 9, No. 11, pp. 898–903, 2010.

[Jawo 11] C. M. Jaworski, J. Yang, S. Mack, D. D. Awschalom, R. C. Myers, and J. P. Heremans. *Phys. Rev. Lett.*, Vol. 106, No. 18, pp. 186601–, 2011.

[John 87] M. Johnson and R. H. Silsbee. *Phys. Rev. B*, Vol. 35, No. 10, pp. 4959–4972, 1987.

[Jong 95] M. J. M. de Jong and L. W. Molenkamp. *Phys. Rev. B*, Vol. 51, No. 19, pp. 13389–13402, 1995.

[Jung 07] T. Jungwirth, J. Sinova, A. H. MacDonald, B. L. Gallagher, V. Novák, K. W. Edmonds, A. W. Rushforth, R. P. Campion, C. T. Foxon, L. Eaves, K. Olejník, J. Mašek, S. R. E. Yang, J. Wunderlich, C. Gould, L. W. Molenkamp, T. Dietl, and H. Ohno. *Phys. Rev. B*, Vol. 76, No. 12, p. 125206, 2007.

[Jung 08] M. H. Jung, S. Park, J. Eom, S. H. Chun, and K. Shin. *J. Appl. Phys.*, Vol. 104, No. 8, pp. 083908–6, 2008.

[Jung 13] T. Jungwirth, J. Wunderlich, V. Novák, K. Olejník, B. L. Gallagher, R. P. Campion, K. W. Edmonds, A. W. Rushforth, A. J. Ferguson, and P. Nemec. *ARXIV*, p. 43, 2013.

[Kasu 59] T. Kasuya. *Progress of Theoretical Physics*, Vol. 22, No. 2, pp. 227–246, 1959.

[Le B 11] J. C. Le Breton, S. Sharma, H. Saito, S. Yuasa, and R. Jansen. *Nature*, Vol. 475, No. 7354, pp. 82–85, 2011.

[Lee 04] W.-L. Lee, S. Watauchi, V. L. Miller, R. J. Cava, and N. P. Ong. *Phys. Rev. Lett.*, Vol. 93, No. 22, pp. 226601–, 2004.

[Lieb 11] N. Liebing, S. Serrano-Guisan, K. Rott, G. Reiss, J. Langer, B. Ocker, and H. W. Schumacher. 2011.

[Lou 07] X. Lou, C. Adelmann, S. A. Crooker, E. S. Garlid, J. Zhang, K. S. M. Reddy, S. D. Flexner, C. J. Palmstrom, and P. A. Crowell. *Nat Phys*, Vol. 3, No. 3, pp. 197–202, 2007.

[MacD 05] A. H. MacDonald, P. Schiffer, and N. Samarth. *Nat Mater*, Vol. 4, No. 3, pp. 195–202, 2005.

[Mark 11a] S. Mark, P. Dürrenfeld, K. Pappert, L. Ebel, K. Brunner, C. Gould, and L. W. Molenkamp. *Phys. Rev. Lett.*, Vol. 106, No. 5, pp. 057204–, 2011.

[Mark 11b] S. Mark, L. Ebel, K. Brunner, C. Gould, and L. W. Molenkamp. *Appl. Phys. Lett.*, Vol. 99, No. 20, pp. 202504–3, 2011.

[Mark 11c] S. Mark. *A Magnetic Semiconductor based Non-Volatile Memory and Logic Element*. PhD thesis, Universität Würzburg, Am Hubland, 97074 Würzburg, 2011.

[Mats 04] F. Matsukura, M. Sawicki, T. Dietl, D. Chiba, and H. Ohno. *Physica E: Low-dimensional Systems and Nanostructures*, Vol. 21, No. 24, pp. 1032–1036, 2004.

[Mats 98] F. Matsukura, H. Ohno, A. Shen, and Y. Sugawara. *Phys. Rev. B*, Vol. 57, No. 4, pp. R2037–R2040, 1998.

[McGu 75] T. McGuire and R. Potter. *Magnetics, IEEE Transactions on*, Vol. 11, No. 4, pp. 1018–1038, 1975.

[Miya 07] T. Miyasato, N. Abe, T. Fujii, A. Asamitsu, S. Onoda, Y. Onose, N. Nagaosa, and Y. Tokura. *Phys. Rev. Lett.*, Vol. 99, No. 8, pp. 086602–, 2007.

[Mole 90] L. W. Molenkamp, H. van Houten, C. W. J. Beenakker, R. Eppenga, and C. T. Foxon. *Phys. Rev. Lett.*, Vol. 65, No. 8, pp. 1052–1055, 1990.

[Moor 65] G. E. Moore. *Electronics*, 1965.

[Moor 75] G. E. Moore. *Electronics*, 1975.

[Mose 07] J. Moser, A. Matos-Abiague, D. Schuh, W. Wegscheider, J. Fabian, and D. Weiss. *Phys. Rev. Lett.*, Vol. 99, No. 5, pp. 056601–, 2007.

[Naga 10] N. Nagaosa, J. Sinova, S. Onoda, A. H. MacDonald, and N. P. Ong. *Rev. Mod. Phys.*, Vol. 82, No. 2, pp. 1539–1592, 2010.

[Nayd 11] T. Naydenova, P. Dürrenfeld, K. Tavakoli, N. Pégard, L. Ebel, K. Pappert, K. Brunner, C. Gould, and L. W. Molenkamp. *Phys. Rev. Lett.*, Vol. 107, No. 19, pp. 197201–, 2011.

[Niel 34] G. S. Nielsen. *Philosophical Magazine Series 7*, Vol. 18, No. 120, pp. 575–579, 1934.

[O Em 61] D. N. O. Emel'yanenko and R. Petrov. *Fiz. Tverdogo Tela*, Vol. 2, p. 2455, 1961.

[Ohno 96] H. Ohno, A. Shen, F. Matsukura, A. Oiwa, A. Endo, S. Katsumoto, and Y. Iye. *Applied Physics Letters*, Vol. 69, No. 3, pp. 363–365, 1996.

[Onsa 31a] L. Onsager. *Phys. Rev.*, Vol. 37, No. 4, pp. 405–426, 1931.

[Onsa 31b] L. Onsager. *Phys. Rev.*, Vol. 38, No. 12, pp. 2265–2279, 1931.

[Osin 04] V. Osinniy, K. Dybko, A. Jedrzejczak, M. Arciszewska, W. Dobrowolski, T. Story, M. V. Radchenko, V. I. Sichkovskiy, G. V. Lashkarev, S. M. Olsthoorn, and J. Sadowski. *ARXIV*, p. 21, 2004.

[Papp 07a] K. Pappert, C. Gould, M. Sawicki, J. Wenisch, K. Brunner, G. Schmidt, and L. W. Molenkamp. *New Journal of Physics*, Vol. 9, p. 354, 2007.

[Papp 07b] K. Pappert, S. Hümpfner, J. Wenisch, K. Brunner, C. Gould, G. Schmidt, and L. W. Molenkamp. *Applied Physics Letters*, Vol. 90, No. 6, p. 062109, 2007.

[Papp 07c] K. Pappert. *Anisotropies in (Ga,Mn)As - Measurement, Control and Application in Novel Devices*. PhD thesis, Universität Würzburg, Am Hubland, 97074 Würzburg, 2007.

[Park 11] B. G. Park, J. Wunderlich, X. Martí, V. Holý, Y. Kurosaki, M. Yamada, H. Yamamoto, A. Nishide, J. Hayakawa, H. Takahashi, A. B. Shick, and T. Jungwirth. *Nat Mater*, Vol. 10, No. 5, pp. 347–351, 2011.

[Pop 10] E. Pop. Vol. 3, No. 3, pp. 147–169–, 2010.

[Pu 06] Y. Pu, E. Johnston-Halperin, D. D. Awschalom, and J. Shi. *Phys. Rev. Lett.*, Vol. 97, No. 3, pp. 036601–, 2006.

[Pu 08] Y. Pu, D. Chiba, F. Matsukura, H. Ohno, and J. Shi. *Phys. Rev. Lett.*, Vol. 101, No. 11, pp. 117208–, 2008.

[Rush 06] A. W. Rushforth, A. D. Giddings, K. W. Edmonds, R. P. Campion, C. T. Foxon, and B. L. Gallagher. *Phys. Status Solidi (c)*, Vol. 3, No. 12, pp. 4078–4081, 2006.

[Rush 07] A. W. Rushforth, K. Výborný, C. S. King, K. W. Edmonds, R. P. Campion, C. T. Foxon, J. Wunderlich, A. C. Irvine, P. Vašek, V. Novák, K. Olejník, J. Sinova, T. Jungwirth, and B. L. Gallagher. *Phys. Rev. Lett.*, Vol. 99, No. 14, pp. 147207–, 2007.

[Rush 09] A. Rushforth, K. Výborný, C. King, K. Edmonds, R. Campion, C. Foxon, J. Wunderlich, A. Irvine, V. Novák, K. Olejník, A. Kovalev, J. Sinova, T. Jungwirth, and B. Gallagher. *Journal of Magnetism and Magnetic Materials*, Vol. 321, No. 8, pp. 1001–1008, 2009.

[Sait 05] H. Saito, S. Yuasa, and K. Ando. *Phys. Rev. Lett.*, Vol. 95, No. 8, pp. 086604–, 2005.

[Schm 07] M. J. Schmidt, K. Pappert, C. Gould, G. Schmidt, R. Oppermann, and L. W. Molenkamp. *Phys. Rev. B*, Vol. 76, No. 3, pp. 035204–, 2007.

[Schm 13] M. Schmid, S. Srichandan, D. Meier, T. Kuschel, J. Schmalhorst, M. Vogel, G. Reiss, C. Strunk, and C. H. Back. *Phys. Rev. Lett.*, Vol. 111, No. 18, pp. 187201–, 2013.

[Shen 97] A. Shen, H. Ohno, F. Matsukura, Y. Sugawara, N. Akiba, T. Kuroiwa, A. Oiwa, A. Endo, S. Katsumoto, and Y. Iye. *Journal of Crystal Growth*, Vol. 175176, Part 2, No. 0, pp. 1069–1074, 1997.

[Slac 10] A. Slachter, F. L. Bakker, J. P. Adam, and B. J. van Wees. *Nat Phys*, Vol. 6, No. 11, pp. 879–882, 2010.

[Slac 11] A. Slachter, F. L. Bakker, and B. J. van Wees. *Phys. Rev. B*, Vol. 84, No. 2, pp. 020412–, 2011.

[Sliw 11] C. Sliwa and T. Dietl. *Physical Review B*, Vol. 83, No. 24, p. 245210, 2011.

[Sury 99] R. Suryanarayanan, V. Gasumyants, and N. Ageev. *Phys. Rev. B*, Vol. 59, No. 14, pp. R9019–R9022, 1999.

[Sze 81] S. M. Sze. *Physics of Semiconductor Devices*. John Wiley & Sons, Inc, 1981.

[Tang 03] H. X. Tang, R. K. Kawakami, D. D. Awschalom, and M. L. Roukes. *Phys. Rev. Lett.*, Vol. 90, No. 10, pp. 107201–, 2003.

[Tang 04] H. X. Tang, S. Masmanidis, R. K. Kawakami, D. D. Awschalom, and M. L. Roukes. *Nature*, Vol. 431, No. 7004, pp. 52–56, 2004.

[Tauc 62] J. Tauc. *Photo and thermoelectric effects in semiconductors. International series of monographs on semiconductors*, Pergamon Press, 1962.

[Thom 54] W. Thomson. *Proc. Roy. Soc. Edinburgh*, pp. 237–41, 1854.

[Tser 13] Y. Tserkovnyak. *Nat Nano*, Vol. 8, No. 10, pp. 706–707, 2013.

[Uchi 08] K. Uchida, S. Takahashi, K. Harii, J. Ieda, W. Koshibae, K. Ando, S. Maekawa, and E. Saitoh. *Nature*, Vol. 455, No. 7214, pp. 778–781, 2008.

[Uchi 10a] K. Uchida, H. Adachi, T. Ota, H. Nakayama, S. Maekawa, and E. Saitoh. *Appl. Phys. Lett.*, Vol. 97, No. 17, pp. 172505–3, 2010.

[Uchi 10b] K. Uchida, J. Xiao, H. Adachi, J. Ohe, S. Takahashi, J. Ieda, T. Ota, Y. Kajiwara, H. Umezawa, H. Kawai, G. E. W. Bauer, S. Maekawa, and E. Saitoh. *Nat Mater*, Vol. 9, No. 11, pp. 894–897, 2010.

[Vasi 72] R. Vasil'eva and B. Akmuradov. *Russ. Phys. J.*, Vol. 15, p. 814, 1972.

[Vybo 09] K. Výborný, J. Kučera, J. Sinova, A. W. Rushforth, B. L. Gallagher, and T. Jungwirth. *Phys. Rev. B*, Vol. 80, p. 165204, 2009.

[Walt 11] M. Walter, J. Walowski, V. Zbarsky, M. Münzenberg, M. Schäfers, D. Ebke, G. Reiss, A. Thomas, P. Peretzki, M. Seibt, J. S. Moodera, M. Czerner, M. Bachmann, and C. Heiliger. *Nat Mater*, Vol. 10, No. 10, pp. 742–746, 2011.

[Weil 12] M. Weiler, M. Althammer, F. D. Czeschka, H. Huebl, M. S. Wagner, M. Opel, I. M. Imort, G. Reiss, A. Thomas, R. Gross, and S. T. B. Goennenwein. *Phys. Rev. Lett.*, Vol. 108, No. 10, pp. 106602–, 2012.

[Weis 13] J. Weischenberg, F. Freimuth, S. Blgel, and Y. Mokrousov. *Phys. Rev. B*, Vol. 87, No. 6, pp. 060406–, 2013.

[Weni 07] J. Wenisch, C. Gould, L. Ebel, J. Storz, K. Pappert, M. J. Schmidt, C. Kumpf, G. Schmidt, K. Brunner, and L. W. Molenkamp. *Phys. Rev. Lett.*, Vol. 99, No. 7, pp. 077201–, 2007.

[Xu 00] Z. A. Xu, N. P. Ong, Y. Wang, T. Kakeshita, and S. Uchida. *Nature*, Vol. 406, No. 6795, pp. 486–488, 2000.

[Zeh 90] M. Zeh, H. Ri, F. Kober, R. P. Huebener, A. V. Ustinov, J. Mannhart, R. Gross, and A. Gupta. *Phys. Rev. Lett.*, Vol. 64, No. 26, pp. 3195–3198, 1990.

Acknowledgements

This work would not be possible without the support and the help of many people. Some of them are not between us to read or hear the end result of this long way. However, here I would like to thank all of you for make that work possible.

- First of all I would like to thank Prof. Laurens W. Molenkamp the head of the EP3 chair and the spintronics group for providing the opportunity to work in his group and for all the discussions, guiding and support.

  Sincerely, I would like to thank:

- PD Dr. Charles Gould the leader of the spintronics group. Asking the right questions is usually more difficult than answering them. Organizing and describing correctly experimental data usually suggest an easy and reliable way of interpreting them. Scientific English is simple. Thanks Charles for the patience and keep on trying to bring that knowledge to me. It is really not easy to be mastered. Physics looks more fun and real with the plenty of examples and inspiriting discussions. Thanks for the supervision and correcting this thesis.
- Stefan Mark for introducing me and guiding me in the labs and the cleanroom work. Thanks for making the bridge technology so clear to me. Thanks also for the couch !!!!
- Christoph Brüne for learning me how to use Lock-In Amplifiers.
- Kia Tawakoli and my two master students Philipp Dürenfeld and Thomas Wagner. Guys, thanks for working with me. It was not always easy but it was really a pleasure for me. To my students I would like to express my special thanks for being so motivated and performing great transport measurements.
- Michael Rüth, Fabian Durr, Gabriel Dengel, Philip Hartmann, Christoph Pohl, Utz Bass and Bastian Büttner for helping me with experiments and giving me always useful advices. Michael, I will never forget your wedding!
- Fanny Greullet, Jennifer Constantino and Marjan Samiepour to give our office such a home-like atmosphere. I hope that you will visit me soon.
- The people from the quantum transport lab for babysitting me and my student when using their dilfridges. Thanks for the many useful tips.

- Lars Ebel for growing the (Ga,Mn)As wafers. And special thanks to Tanja Borzenko for guiding me in the cleanroon. Thanks for Volkmar Hock for the support during processing. Thanks to many other people who contributed to discussions, measurement setups etc.: Petra Wolf-Müller, Roland Ebert, and everyone else from EP3.

- I also would like to gratefully acknowledge the financial support from the European Union (SemiSpinNet).

- My friends Eva, Feli, Mandy, Marta and Paola for having so many nice moments in Würzburbg and being next to me during these years.

- Megi, Didi, Niki, Viki, Dino, Kiro, Hristo, Gogo, Galq, Zdravka, Io, Joli, Mariela. Thanks all of you for the great time and vacations!!!!

- Agi who never left me alone and homesick here in Germany. Danke dass es Dich gibt!!!

- My family for giving a meaning to everything!!! Mamo, Tati, Mariq, Babo, Inko, Stefcho, Blagodarq Wi, che ne sprqhte da me podkrepqte i da wqrwate w men! Wie ste Wsichko za men!!!!